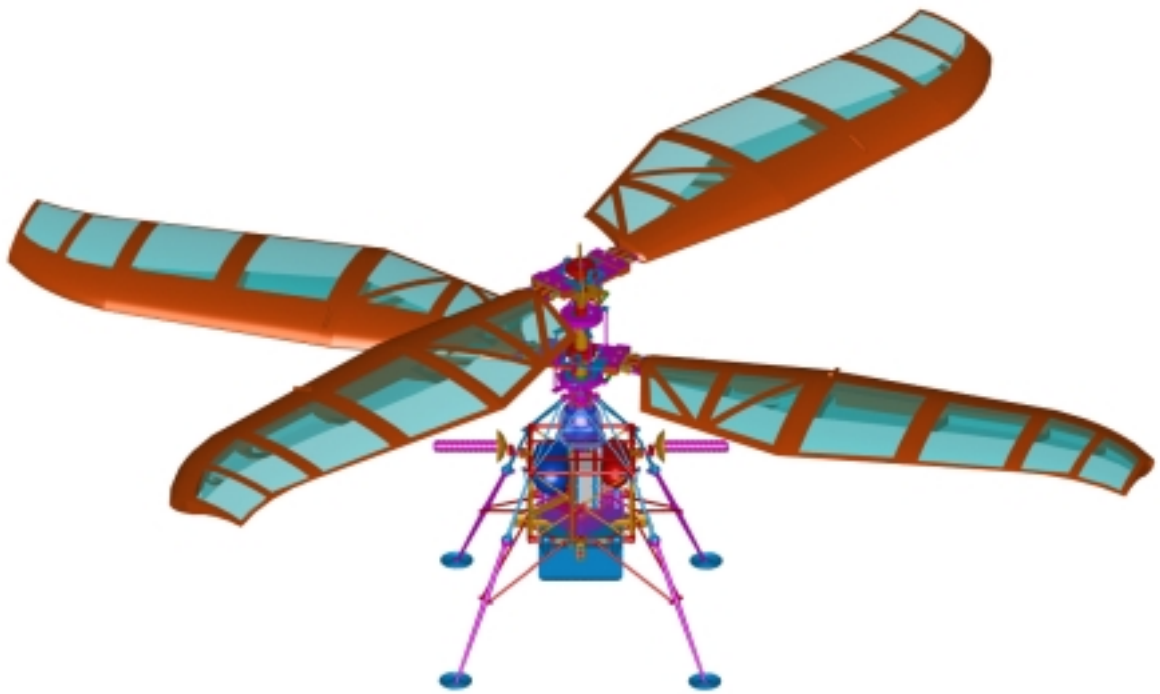


# THE MARTIAN AUTONOMOUS ROTARY-WING VEHICLE (MARV)



Alfred Gessow Rotorcraft Center  
Department of Aerospace Engineering  
University of Maryland  
College Park, Maryland 20742  
June 1, 2000

University of Maryland



Alfred Gessow Rotorcraft Center  
Department of Aerospace Engineering  
University of Maryland  
College Park, Maryland 20742

# THE MARTIAN AUTONOMOUS ROTARY-WING VEHICLE (MARV)

In response to the 2000 American Helicopter Society  
Student Design Competition - Graduate Category  
1 June 2000

---

Anubhav Datta - Team Leader

---

Dr. Inderjit Chopra - Faculty Advisor

---

Jinsong Bao

---

Olivier Gamard

---

Dan Griffiths

---

Lin Liu

---

Greg Pugliese

---

Beatrice Roget

---

Jayanarayanan Sitamaran

# ACKNOWLEDGEMENTS

The design team has been extremely fortunate to have the opportunity to work not only with the esteemed faculty of the Alfred Gessow Rotorcraft Center, but also with Prof. Marat Tishchenko from the Mil Design Bureau. His insights, suggestions, and vast knowledge of design issues helped us immensely in our efforts. We would like to thank Prof. Alfred Gessow, for his keen insight and encouragement. We also thank Dr. Nagaraj, for his guidance and lectures on helicopter design. The inputs of Dr. Leishman and Dr. Lewis, who answered many questions that arose during the design process, are also much appreciated. Dr. Greg Jackson was also very helpful with the design of the fuel cell system. Special thanks also goes to fellow graduate student Preston Martin, without whose knowledge of and expertise with airfoil design issues and methods would have made the new airfoil design almost impossible. Finally, we thank Prof. Inderjit Chopra, for his suggestions and motivation, and for giving us the opportunity to partake in this exciting design competition.

# CONTENTS

<b>Table of Contents</b>	<b>ii</b>
<b>List of Figures</b>	<b>vi</b>
<b>List of Tables</b>	<b>viii</b>
<b>Report Requirements and Compliance</b>	<b>ix</b>
<b>RFP Requirements and Compliance</b>	<b>x</b>
<b>Executive Summary</b>	<b>1</b>
<b>1 Introduction</b>	<b>7</b>
<b>2 Feasibility Study for a Rotorcraft on Mars</b>	<b>8</b>
2.1 Comparison of basic atmospheric characteristics . . . . .	8
2.2 Critical design issues . . . . .	8
2.3 Demonstration of flight capability and estimation of hover power . . . . .	9
2.4 Availability of power . . . . .	10
2.5 Communication between vehicle and lander . . . . .	10
2.6 Results of feasibility study . . . . .	11
<b>3 Mission Profile</b>	<b>11</b>
3.1 Mission objectives . . . . .	11
3.2 Preferable mission parameters . . . . .	11
3.3 Mission profile . . . . .	12
3.4 Basic mission power/energy requirements . . . . .	13
3.5 Extended mission . . . . .	13
3.6 Extended mission power/energy requirements . . . . .	15
3.7 Alternate missions . . . . .	15
<b>4 Selection of Rotor Configuration</b>	<b>16</b>
4.1 Choice of candidate configurations and selection criteria . . . . .	16
4.2 Evaluation of the configurations . . . . .	17
4.3 Down selection . . . . .	21
4.4 Coaxial and quad rotor trade off studies . . . . .	21
4.4.1 Trade study methodology . . . . .	21
4.4.2 Trade study results . . . . .	21
4.4.3 Selection of configuration . . . . .	22
4.5 Coaxial trade off studies . . . . .	22
4.5.1 Number of blades . . . . .	22
4.5.2 Control mechanism and landing gear . . . . .	23
4.6 Summary . . . . .	24

<b>5</b>	<b>Aerodynamic Design</b>	<b>24</b>
5.1	Methodology . . . . .	24
5.2	Planform design . . . . .	25
5.2.1	Momentum theory analysis . . . . .	25
5.2.2	Blade element/momentum analysis . . . . .	26
5.2.3	Development of planform . . . . .	26
5.2.4	Comparison to existing planforms . . . . .	27
5.3	Airfoil design . . . . .	29
5.3.1	Necessity of new design . . . . .	29
5.3.2	Design process . . . . .	30
5.3.3	Forward flight considerations . . . . .	31
5.3.4	Features of the AGRC 1506 airfoil . . . . .	32
5.3.5	Rotor specifications . . . . .	33
<b>6</b>	<b>Rotor Blade Structural Design</b>	<b>33</b>
6.1	Detailed design of the rotor blade . . . . .	33
6.1.1	Design methodology . . . . .	33
6.1.2	Final rotor configuration . . . . .	34
6.1.3	Weights . . . . .	36
6.2	Deployment mechanism of the rotor blade . . . . .	37
6.2.1	Deployment hinges . . . . .	37
<b>7</b>	<b>Hub Structural Design</b>	<b>39</b>
7.1	Functions of the rotor hub . . . . .	39
7.2	Selection of hub type and layout . . . . .	39
7.2.1	Critical issues for Martian helicopter . . . . .	39
7.3	Detailed design . . . . .	42
<b>8</b>	<b>Blade Dynamics and Kinematics</b>	<b>44</b>
8.1	Dynamics and stability . . . . .	44
8.2	Kinematics and clearances . . . . .	45
8.3	Vibration issues . . . . .	45
<b>9</b>	<b>Selection of Powerplant</b>	<b>47</b>
9.1	Key questions for Martian propulsion . . . . .	47
9.2	Analysis and selection of energy options . . . . .	47
9.3	Answers to the key questions . . . . .	52
<b>10</b>	<b>Power Plant Design</b>	<b>53</b>
10.1	Fuel cell description . . . . .	54
10.2	Fuel cell stack design . . . . .	54
10.3	Fuel storage . . . . .	55
10.4	System operation . . . . .	56
10.5	System issues . . . . .	58
10.5.1	Growth potential . . . . .	59
10.6	Stack technical specifications . . . . .	59

<b>11</b>	<b>Selection of Electric Motor</b>	<b>60</b>
11.1	DC motor . . . . .	60
11.2	Brushless DC motors . . . . .	60
11.3	Speed setting and control . . . . .	61
11.4	Selection of brushless DC motor . . . . .	61
<b>12</b>	<b>Transmission Design</b>	<b>61</b>
12.1	Problem formulation . . . . .	61
12.2	Trade-off study . . . . .	62
12.3	Detailed design of configuration 4 . . . . .	63
12.4	Integration of structure . . . . .	65
12.5	Lubrication of gears . . . . .	66
<b>13</b>	<b>Rotor Control System</b>	<b>66</b>
13.1	Trade-off study . . . . .	68
13.2	Control system design . . . . .	68
<b>14</b>	<b>Landing Gear Design</b>	<b>71</b>
14.1	Landing leg deployment mechanism design . . . . .	72
14.2	Landing gear sizing . . . . .	72
14.2.1	Trade study . . . . .	74
<b>15</b>	<b>Fuselage Design</b>	<b>75</b>
15.1	Internal configuration . . . . .	75
15.2	Gearbox suspension . . . . .	76
<b>16</b>	<b>Materials and Manufacturing</b>	<b>77</b>
16.1	Properties of aerospace materials at low temperatures . . . . .	77
16.2	Materials for primary structures . . . . .	78
16.3	Manufacturing . . . . .	79
<b>17</b>	<b>Avionics Selection</b>	<b>80</b>
17.1	Outboard avionics . . . . .	81
17.2	Inboard avionics . . . . .	82
17.3	Flight computer . . . . .	85
17.4	Component placement/deployment . . . . .	85
17.5	Redundancy/reliability . . . . .	86
17.6	Summary . . . . .	87
<b>18</b>	<b>Weight and Balance</b>	<b>87</b>
18.1	Weight breakdown . . . . .	87
18.2	Balance . . . . .	89
<b>19</b>	<b>Performance Analysis</b>	<b>89</b>
19.1	Drag breakdown . . . . .	90
19.2	Analysis methodology . . . . .	91
19.3	Performance results . . . . .	92

<b>20 Project Plan</b>	<b>93</b>
20.1 Critical technologies and risk assessment . . . . .	93
20.2 Critical technology areas . . . . .	94
20.2.1 Technology roadmap . . . . .	94
20.2.2 Risk reduction testing . . . . .	94
20.3 Preliminary resource estimate . . . . .	95
20.3.1 Cost of R&D . . . . .	95
20.3.2 Cost of manufacturing . . . . .	95
20.3.3 Mars mission cost . . . . .	96
20.4 Redundancy and reliability . . . . .	97
<b>21 Summary and Conclusions</b>	<b>97</b>
<b>Bibliography</b>	<b>97</b>

# LIST OF FIGURES

E.1	Cutaway drawing of MARV . . . . .	4
E.2	Four-view drawing of MARV . . . . .	5
E.3	Inboard view . . . . .	6
2.1	Required mean lift coefficient versus rotor radius . . . . .	10
3.1	Basic mission profile . . . . .	12
3.2	Extended mission profile . . . . .	14
4.1	Single rotor configurations . . . . .	19
4.2	Twin rotor configurations . . . . .	19
4.3	Quad rotor configurations . . . . .	20
4.4	Other flying/tested rotorcraft configurations . . . . .	20
4.5	A coaxial configuration . . . . .	21
4.6	Two multi-rotor configurations . . . . .	22
4.7	Performance comparison of coaxial and quad rotor designs . . . . .	23
4.8	Performance comparison of 2-bladed and 3-bladed rotors of equal solidity . . . . .	23
5.1	Disk loading vs 1 / power loading for powered-lift aircraft on Earth and Mars . . . . .	24
5.2	Rotor blade planform and propeller blades on existing aircraft . . . . .	28
5.3	Reynolds number and Mach number distribution in hover . . . . .	29
5.4	Operating envelopes of airfoil and rotor . . . . .	31
5.5	AGRC 1506 profile . . . . .	32
5.6	Lift and pitching moment coefficients in hover . . . . .	32
6.1	Design methodology . . . . .	34
6.2	Four view drawing of the rotor blade . . . . .	35
6.3	Section A-A' . . . . .	35
6.4	Section B-B' . . . . .	36
6.5	Section C-C' . . . . .	36
6.6	Blade in the folded position . . . . .	37
6.7	Mid span deployment hinge details . . . . .	38
6.8	Root deployment hinge details . . . . .	38
6.9	Configuration of MARV stowed inside lander . . . . .	40
6.10	Deployment scheme . . . . .	41
7.1	Hub design . . . . .	43
8.1	Stiffness and inertia distributions on the rotor blade . . . . .	44
8.2	Fan diagram of the rotor blades . . . . .	44
8.3	Vertical 2/rev vibration measured in Earth g-level . . . . .	46
9.1	Current battery technology . . . . .	48
10.1	Schematic of an individual fuel cell . . . . .	54
10.2	Performance of PEM fuel cells . . . . .	55
10.3	Power density of PEM fuel cells . . . . .	55
10.4	Mass of fuel cell system . . . . .	56
10.5	Energy density and power density . . . . .	56
10.6	Fuel cell system . . . . .	57
10.7	Mission power profile . . . . .	57

10.8	Current density drawn from each cell . . . . .	57
10.9	Fuel consumption rate . . . . .	58
10.10	Mass of fuel consumed during flight . . . . .	58
10.11	Cell voltage during mission . . . . .	58
10.12	Stack voltage during mission . . . . .	58
11.1	DC motor . . . . .	60
12.1	Transmission configurations 1 and 2 . . . . .	62
12.2	Transmission configurations 3 and 4 . . . . .	62
12.3	Design constraint of configuration 4 . . . . .	64
12.4	Hollow ratio effect on the diameter and cross section area of the shaft . . . . .	65
12.5	Integration of transmission . . . . .	65
12.6	Gearbox section and isometric view . . . . .	67
13.1	Control by shaft tilt and CG shift . . . . .	68
13.2	Yaw control system . . . . .	69
13.3	Hub and control system assembly . . . . .	70
14.1	Viking image of the Martian surface . . . . .	71
14.2	Fully deployed landing gear system . . . . .	72
14.3	Fully retracted landing gear system . . . . .	73
14.4	Different landing cases considered for leg sizing . . . . .	74
14.5	Design space for a four legged system . . . . .	74
15.1	Fuselage structure . . . . .	75
15.2	Gearbox suspension . . . . .	77
16.2	Interlaminar shear strength and matrix strength versus temperature . . . . .	78
16.1	Average and range of fracture toughness values for three test orientations . . . . .	78
17.1	Transducers . . . . .	81
17.2	Sony Xc-999 . . . . .	81
17.3	Mini gyro . . . . .	82
17.4	Tachometer . . . . .	82
17.5	Helical antenna . . . . .	84
17.6	Placement of avionics . . . . .	86
18.1	Preliminary estimate based on Boeing-Vertol formulae . . . . .	88
18.2	Comparison between actual weights and predictions . . . . .	88
18.3	Component CG locations on the MARV . . . . .	90
19.1	Rotor operating envelope in forward flight . . . . .	91
19.2	Power required in forward flight . . . . .	92
19.3	Power breakdown . . . . .	92
19.4	Payload vs range . . . . .	93
20.1	Preliminary resource estimate . . . . .	96

# LIST OF TABLES

2.1	Comparison of atmospheric properties . . . . .	8
3.1	Mission objectives . . . . .	11
3.2	Basic mission energy requirements . . . . .	14
3.3	Extended mission energy requirements . . . . .	15
3.4	Sample-return mission energy requirements . . . . .	16
4.1	Selection criteria . . . . .	17
4.2	Single rotor configurations (Fig. 4.1) . . . . .	17
4.3	Twin rotor configurations (Fig. 4.2) . . . . .	18
4.4	Multi-rotor configurations (Fig. 4.3) . . . . .	18
4.5	Other helicopter configurations (Fig. 4.4) . . . . .	19
5.1	50kg Earth vehicle on Mars . . . . .	28
5.2	Rotor characteristics . . . . .	33
6.1	Weights of blade components . . . . .	37
8.1	Natural frequencies of the rotor blades . . . . .	45
8.2	Lateral flapping response to gust . . . . .	45
9.1	Comparison of energy systems . . . . .	51
10.1	Stack technical specifications . . . . .	59
12.1	Sizes of first stage gear . . . . .	63
12.2	Sizes of second stage gear . . . . .	64
12.3	Sizes of internal meshing gear . . . . .	64
16.1	Typical properties for some metallic alloys . . . . .	79
16.2	Typical properties for some composites . . . . .	79
17.1	Avionics weight table . . . . .	87
18.1	Weight and CG location breakdown . . . . .	89
19.1	Drag breakdown . . . . .	90
20.1	Manufacturing cost breakdown . . . . .	96

# REPORT REQUIREMENTS AND COMPLIANCE

<b>RFP Requirement</b>	<b>Supplied in Report</b>	<b>References</b>
Three view drawing	Supplied	Pg. 5
Inboard profile drawing	Supplied	Pg. 6
Description and illustration of rotorcraft stowed in lander	Detail folding mechanism and stowed illustration	Sec. 6.2
Description and illustration of rotorcraft deployed from lander	Detail description and illustration of step by step deployment	Sec. 6.2
Weight empty and mission gross weight derivation	Detailed weight table	Sec. 18.2
Propulsion system requirements	Detail design and description	Chap. 10
Flight controls requirement	Detailed swashplate control design	Chap. 13
Payload-range curve	Supplied	Chap. 19
Drag prediction	Supplied	Chap. 19
Power required vs airspeed	Supplied	Chap. 19
Risk reduction program	Supplied	Sec. 20.2
Redundancy and reliability	Supplied	Sec. 20.4

# RFP REQUIREMENTS AND COMPLIANCE

RFP Requirement	MARV Characteristics	Reference
Vehicle mass not to exceed 50 kg	Mass of 50 kg	Sec. 2.3
Controlled flight duration of no less than 30 mins	Endurance of 39 minutes	Table 3.2
Range greater than 25 km	Range of 25.12 km with restart	Sec. 3.5
Maximum cruise altitude 100 m	Cruise altitude 100 m	Sec. 3.3
Soft landing and complete shutdown	Soft landing and shutdown	Sec. 3.3, Chap. 14
Assess effect of 20% knockdown on given density and pressure	Entire design based on 20% knockdown	Chap. 5, Chap. 19
Hovering flight for no less than 1 minute	Hover for 1 minute	Sec. 3.3
Consideration of gust between 3-7 m/s	Airfoil designed for gusts of 7m/s, rotor spacing safe for much higher values	Sec. 8.2
Autonomous deployment	Detailed deployment mechanism developed	Sec. 6.2
Avionics not more than 10% of vehicle mass	Avionics 8.1% of vehicle mass	Sec. 17.6
Entry deceleration of $100 \text{ m/s}^2$	Structure withstands reentry loads	Sec. 12.3
Telemetry requirements	Complete avionics package for in flight and post-soft-landing image telemetry, flight profile and vehicle status telemetry.	Chap. 17
Sustain continuous full sensor and data relay power for 4 hours after seperation from lander	Required power and energy supplied by backup batteries	Sec. 17.5
Second startup and take off, desired	Second startup, take off and flight of 3 minutes	Sec. 3.6

# EXECUTIVE SUMMARY

The Martian Autonomous Rotary-wing Vehicle (MARV) is an autonomous rotorcraft (autonomous except for passive telemetry and course-correction aid from lander) for Martian exploration which has been designed in response to the American Helicopter Society's Seventeenth Annual Student Design Competition. The Request For Proposals (RFP) described the motivation for such an endeavor as being a natural extension of the use of robotic vehicles for planetary exploration. An autonomous rotorcraft, while a new concept for this purpose, would have several advantages over a conventional fixed-wing or ground-based vehicle. These include the ability to hover and fly slowly, allowing detailed imaging of terrain; the capability of soft landing and associated vehicle reuse; and having a greater range and speed than a ground-based rover.

## Mission requirements and design objectives

The RFP specifies a number of required mission elements as part of the standard flight profile. Chief among these is the requirement that the rotorcraft maintain sustained controlled flight for a minimum of 30 minutes. Of secondary importance is the desire to have a range of at least 25 km. The overall strategy during the design process was to develop a vehicle that could carry the greatest possible payload within the weight limit of 50 kg specified in the RFP. The weight limit was interpreted as the maximum amount that NASA would be willing to carry (and pay for) and that the focus should thus be on carrying the highest payload possible. This resulted in a 50 kg vehicle which can carry 10.8 kg of payload over a range of 25 km.

## Selection of coaxial configuration

Initial concept development resulted in a large number of different rotorcraft configurations. It was decided, in addition to the fundamental low Reynolds number issue which argued for as large a vehicle as possible, it would be best to develop a vehicle which could carry the maximum payload for the given take off weight. Initial studies conducted based on Boeing-Vertol methodology showed that the payload fraction remains nominally constant from a total vehicle take off mass of 20 kg to 50 kg. To have a substantial payload capability suitable for future sample return type missions, over a long range, it was decided that a vehicle gross weight of 50 kg would be most suitable. Hence a 50 kg vehicle take off mass maximizes both payload and payload fraction. The amount of payload that can be carried translates directly into the scientific utility of the vehicle, and because of the cost and rarity of such planetary exploration, this is what should be maximized in this design.

A coaxial configuration was chosen. The single-rotor/tail rotor configuration requires a long fuselage in order for the tail rotor to have a sufficiently long moment arm. Also a single rotor would require a higher rotor radius compared to a multi-rotor configuration. These factors made packaging of a single rotor inside the lander and subsequent deployment extremely complex. A coaxial, in contrast could generate the required amount of thrust for the smallest rotor disk area and needed no antitorque device. At the same time, it could be designed to achieve the blade Reynolds numbers necessary for efficient airfoil operation. The fuselage dimensions are no longer than required for payload and system packaging. Packaging inside the lander is compact and convenient. The quad rotor produced blade Reynolds numbers that appeared to be low for a reasonable overall vehicle size. In addition the complexity of having to power and control four separate rotors was deemed to be more than that of a coaxial. Above all, the coaxial is a mature and proven technology in contrast to quadrotors which are in the experimental stage. Thus the coaxial configuration appeared to be the most reliable configuration for Mars. For

proof of concept demonstration it was deemed essential to pick a configuration that not only appears to have higher payload capability but also one which can be used with maximum confidence. In terms of technological maturity and knowledge base, a coaxial far outweighs a quad rotor design.

## Design features of the MARV

The MARV is an autonomous coaxial helicopter. The design is dominated by the unusual and often conflicting aerodynamic challenges of flight in the Martian atmosphere. Predicted size constraints inside the lander, as well as the stated weight limit of 50 kg, limit the physical size of the helicopter. Even with these challenges, the MARV has been carefully designed to achieve a maximum sustained flight for 30 minutes, having an associated range of 25 km. The MARV can then make a controlled landing on the Martian surface, and shortly thereafter perform another takeoff.

The rotors on the MARV seem to resemble turbine blades more than traditional helicopter main rotor blades. However, the blade planform stemmed from the unique aerodynamic concerns arising from operation in the Martian atmosphere, where the density of almost one one-hundredth that on Earth makes blade Reynolds numbers one or two orders of magnitude below those normally encountered on Earth, as well as lowering the speed of sound. Here are the highlights of the MARV design:

**Specially designed airfoil** meets the requirements of high lift at low Reynolds number and high subsonic Mach number, a combination of conditions that is rarely found on Earth.

**Airfoil camber** increases lifting capability. Low dynamic pressure ensures that the dimensional pitching moment is not high.

**Low aspect ratio blades** maximize blade Reynolds number while keeping the rotor diameter as small as possible. This produces a maximum blade Reynolds number of 78,000, and keeps the Reynolds number above 60,000 along more than half of the radius (below 50,000, it becomes extremely difficult to keep the boundary layer attached beyond the leading edge under any condition).

**Taper** is used to minimize induced power while still generating high Reynolds numbers on inboard portions of the blade.

**Parabolic tip sweep** keeps the incident Mach number at or below 0.5 along the entire blade, avoiding adverse compressibility effects, while allowing the rest of the blade to operate at conditions corresponding to an effectively higher Mach number.

**Non-linear twist** is used to produce the desired distribution of lift coefficient along the blade, avoiding sharp peaks or changes at any radial station.

**Boundary layer trips** are added on both the upper and lower surfaces to artificially transition the boundary layer to a turbulent state, energizing it and allowing it to stay attached for a much longer portion of the chord, as well as preventing the formation of a laminar separation bubble. Without such trips, at such low Reynolds numbers the laminar boundary layer separates before becoming turbulent, making re-attachment very difficult. Even if re-attachment does occur, a laminar separation bubble forms. As discussed above, trips may not work below Reynolds numbers of 50,000.

**A coaxial configuration** eliminates the need for a tail rotor and allows the rotor and fuselage to be as small as possible while still generating the required amount of thrust.

**A conventional washplate design** is a proven effective means of control for coaxial rotors, whereas other methods have questionable effectiveness in such an environment.

**An efficient electric motor** minimizes powerplant weight and allows a high payload.

The rotor blades fold in two places, allowing **compact storage in the lander** during travel to Mars, minimizing the size requirement of the spacecraft. Special care is taken such that the **folded size matches the current dimensions of the Mars polar lander**. When on the Martian surface, the blades self-deploy and snap into place, keeping their extended position.

**Retractable, lightweight composite landing legs** provide the capability for a soft landing on the Martian surface after flight, avoiding damage to the vehicle and making another takeoff possible.

**Innovative teetering hub design** facilitates blade motions for load reduction as well as proper frequency placement to reduce vibration loads; a flexbeam hub design reduces **inplane vibration**; and **aeromechanic instabilities** are eliminated without the use of lag dampers.

**Optimum rotor phasing** based on trade-offs between low 2/rev g-levels and compactness of folding.

**Detailed control system design** with yaw stability scheme tailored for a two-bladed rotor.

**Light weight transmission** including bearings and gear teeth design.

State of the art **Proton Exchange Membrane (PEM) fuel cell powerplant**. Only pure hydrogen and pure oxygen used for power generation, producing no environmentally harmful byproducts.

**Heaters provide insulation** to protect avionics and subsystems from extreme low temperatures.

**Fuselage shape** allows placement of payload in locations that provide unobstructed views of the Martian landscape in flight.

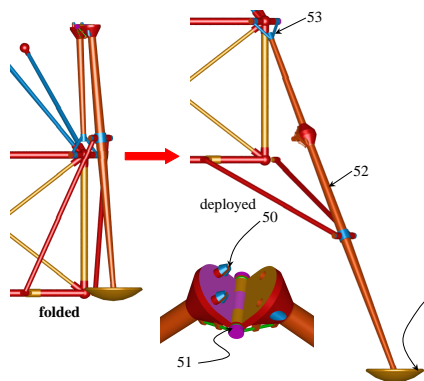
**Specially designed communication antennas** to provide line of sight communication capability.

A full suite of **advanced navigation, communication, and scientific electronic equipment** makes the vehicle autonomous apart from passive telemetry.

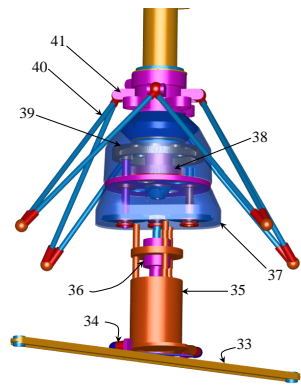
**Innovative integration of state of the art proven technology, with minimal reliance on future technology**.

## Download document

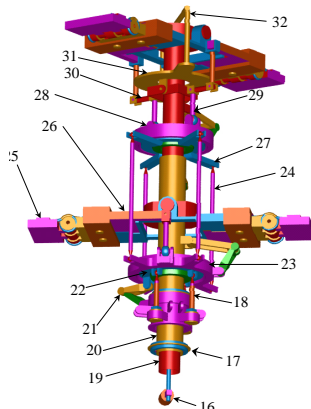
This document can be downloaded in PDF form from the following internet address:  
<http://www.ena.e.umd.edu/AGRC/Design00/MARV.html>



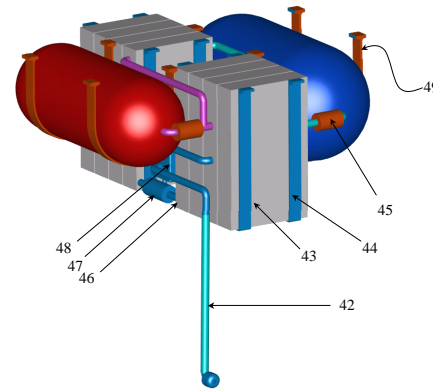
**Landing Gear Deployment Linkages**



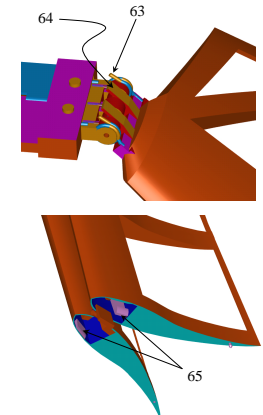
**Transmission and Suspension**



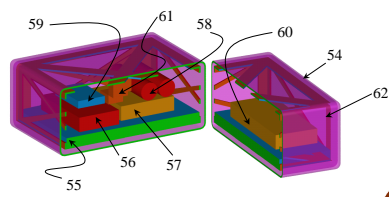
**Hub and Control System**



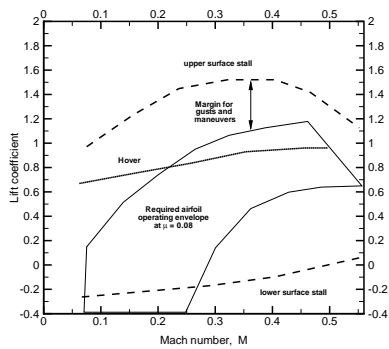
**Fuel Cell System**



**Blade Deployment Systems**



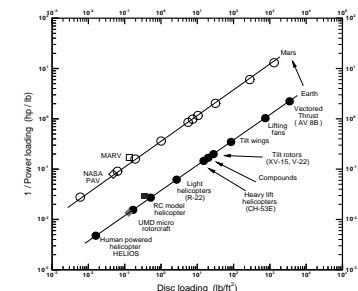
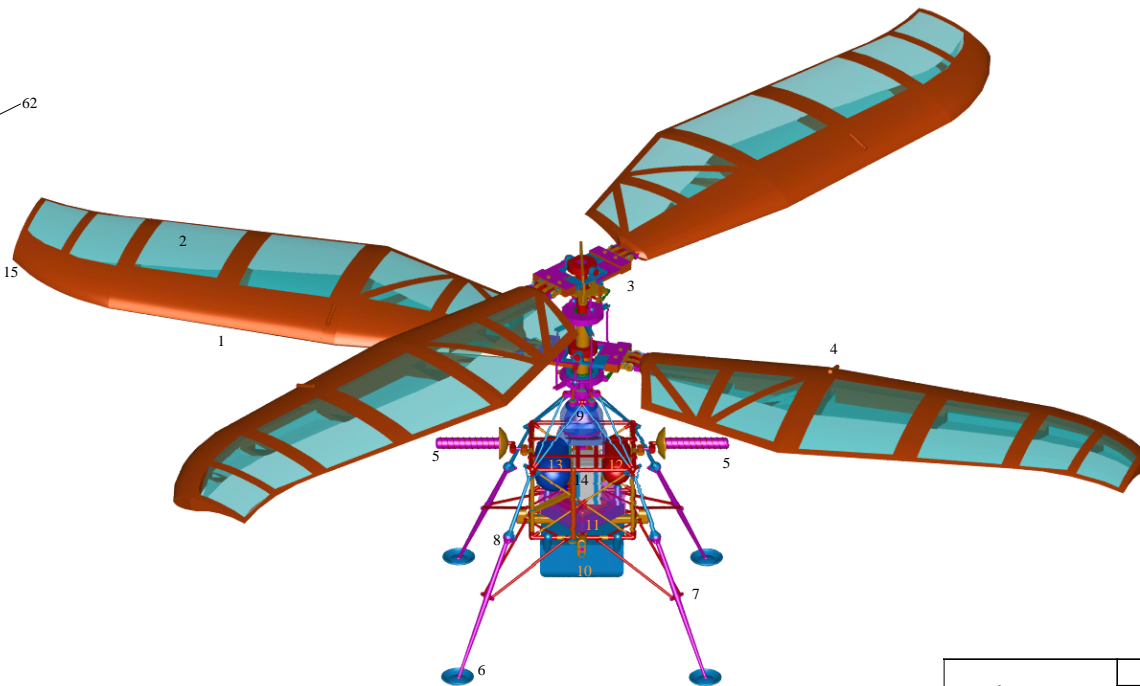
**Avionics and Navigation Package**



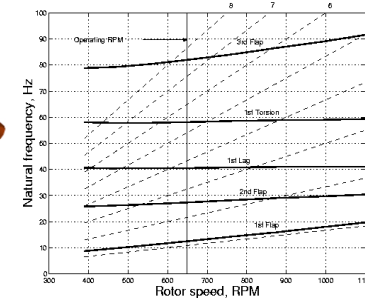
**Operating Envelope**

**MARV, cutaway drawing key**

- |  |  |                               |                                     |                                    |
|--|--|-------------------------------|-------------------------------------|------------------------------------|
| 1. Fully composite rotor blade               | 14. Fuel cell system (see detail)      | 27. Upper control swashplate  | 40. Lift transfer links to fuselage | 53. Hinged landing gear attachment |
| 2. Ultrathin Mylar skin                      | 15. Swept tip for constant Mach number | 28. Upper rotating swashplate | 41. Fuselage attachment hard point  | 54. Aerogel insulation             |
| 3. Hub and control system (see detail)       | 16. Yaw actuator                       | 29. Pitch control link        | 42. Heated water exhaust            | 55. Flight computer                |
| 4. Midspan blade deployment hinge            | 17. Outer shaft lower bearing          | 30. Yaw fork link             | 43. Fuel cell stacks                | 56. Data multiplexer               |
| 5. Directional UHF antennas and actuator     | 18. Cyclic and collective actuators    | 31. Yaw actuation disk        | 44. Stack attachment                | 57. Transceiver                    |
| 6. Landing gear foot pads                    | 19. Inner shaft                        | 32. Yaw control linkages      | 45. Fuel valve                      | 58. Backup batteries               |
| 7. Secondary support studs                   | 20. Outer shaft                        | 33. Motor torsion support     | 46. Cell unit (8 modules)           | 59. Computerized compass           |
| 8. Landing gear deployment hinge(see detail) | 21. Torque link                        | 34. Elastomeric bushing       | 47. Humidizer                       | 60. Temperature sensor             |
| 9. Gearbox (see detail)                      | 22. Non-rotating swashplate            | 35. Aveox brushless DC motor  | 48. Water reservoir                 | 61. Gyroscopes                     |
| 10. Main payload bay                         | 23. Lower rotating swashplate          | 36. Clutch                    | 49. Tank attachment                 | 62. Heated container               |
| 11. Main avionics bay                        | 24. Swashplate links                   | 37. Gearbox casing            | 50. Pawl latch                      | 63. Deployment torsion spring      |
| 12. Liquid O <sub>2</sub> tank               | 25. Blade deployment hinge             | 38. Inner shaft spur gear     | 51. Torsion spring                  | 64. Positive hinge lock            |
| 13. Liquid H <sub>2</sub> tank               | 26. Compact feathering door hinge      | 39. Outer shaft spur gear     | 52. Primary support strut           | 65. Pawl locking mechanism         |



**Design Space Envelope**



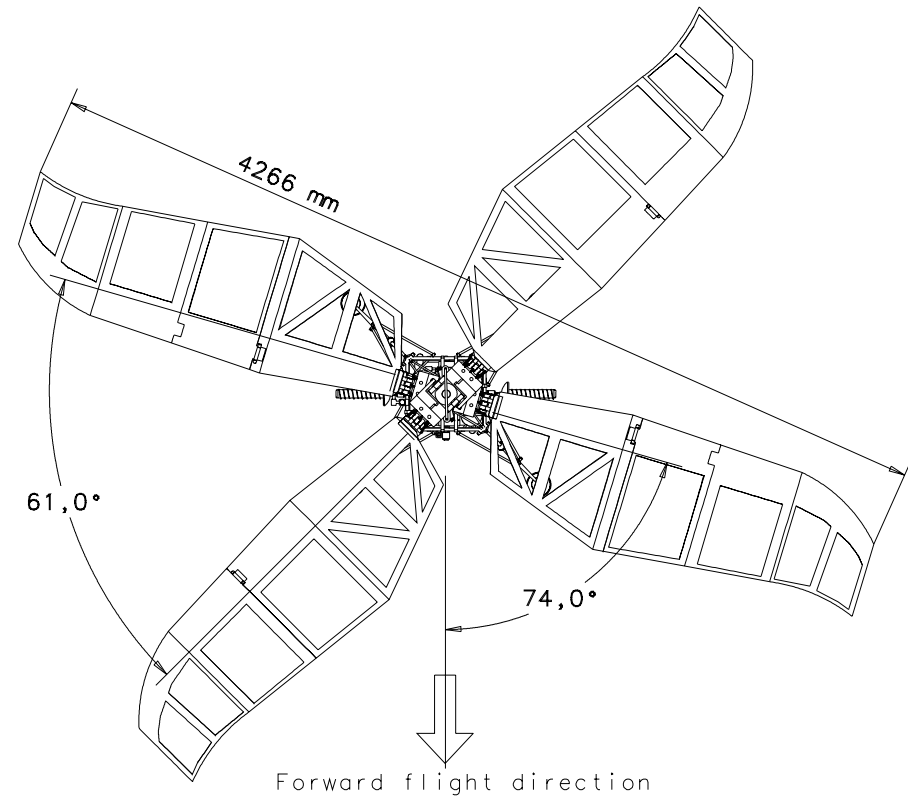
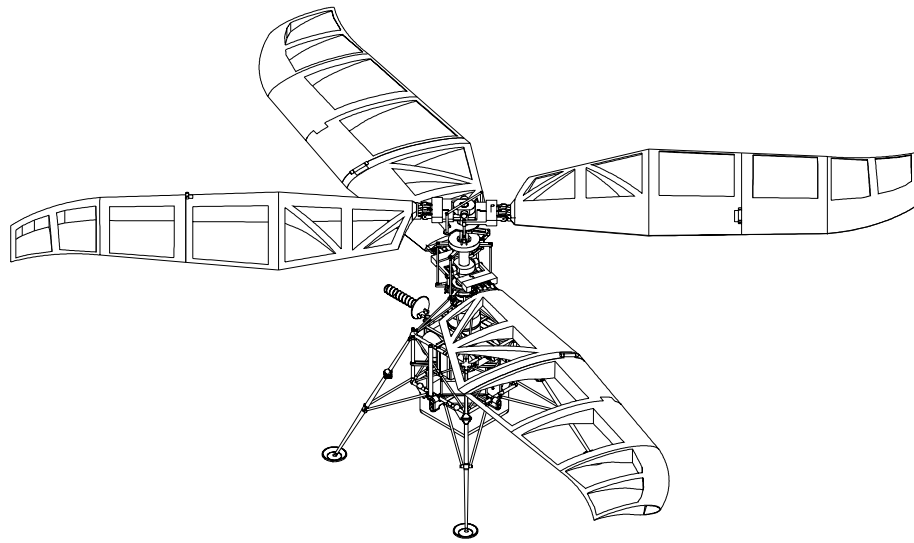
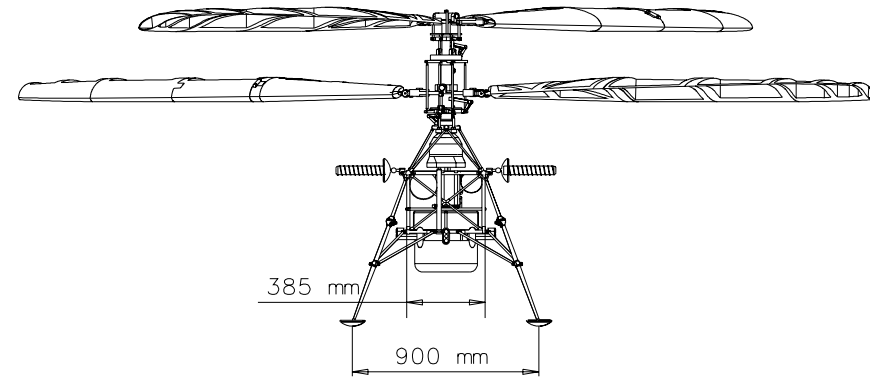
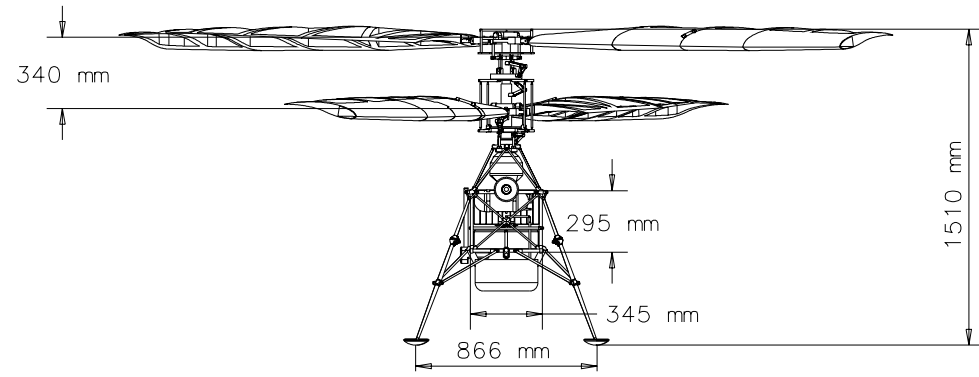
**Rotor Frequency Plot**

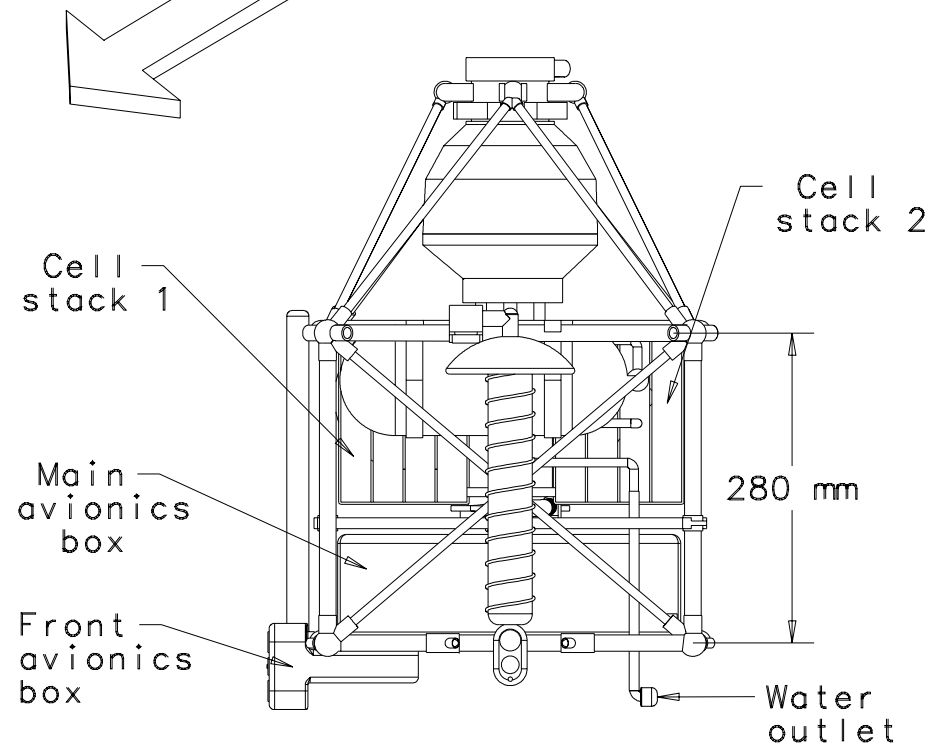
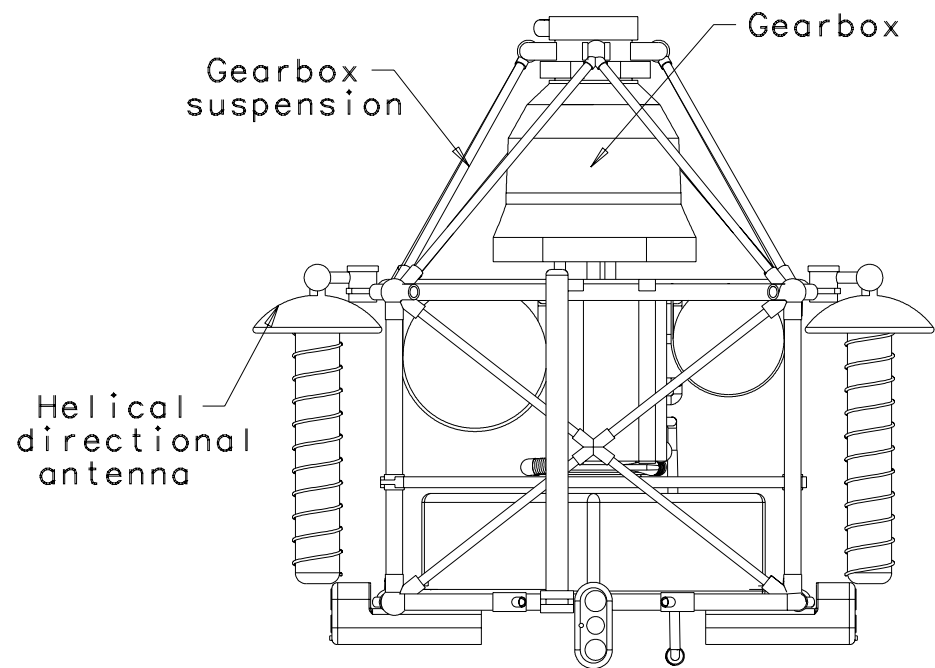
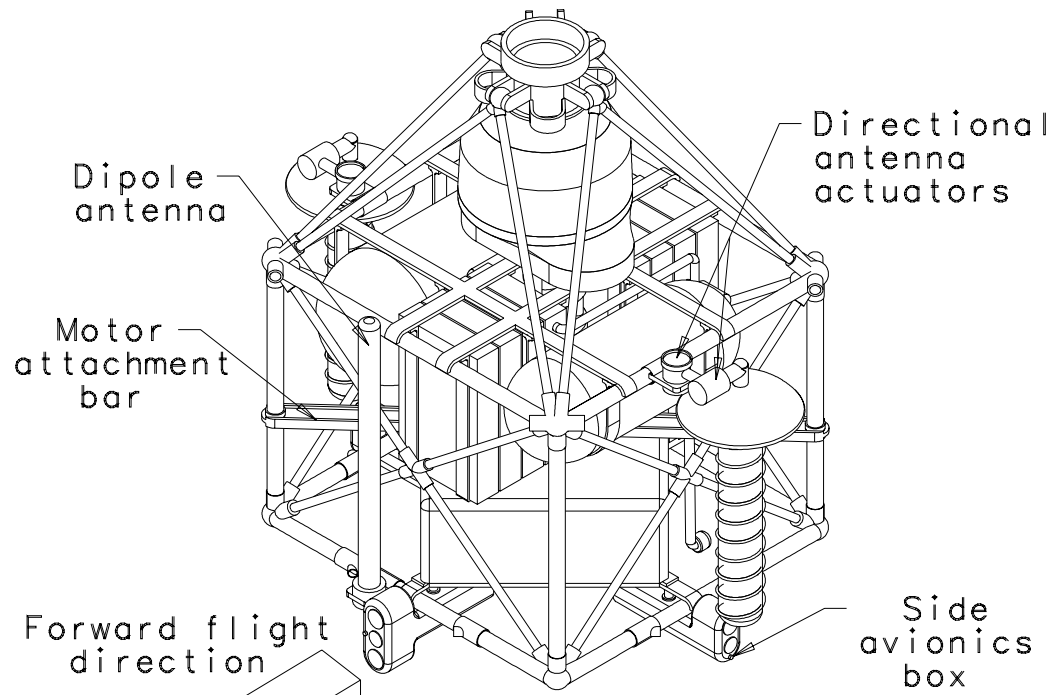
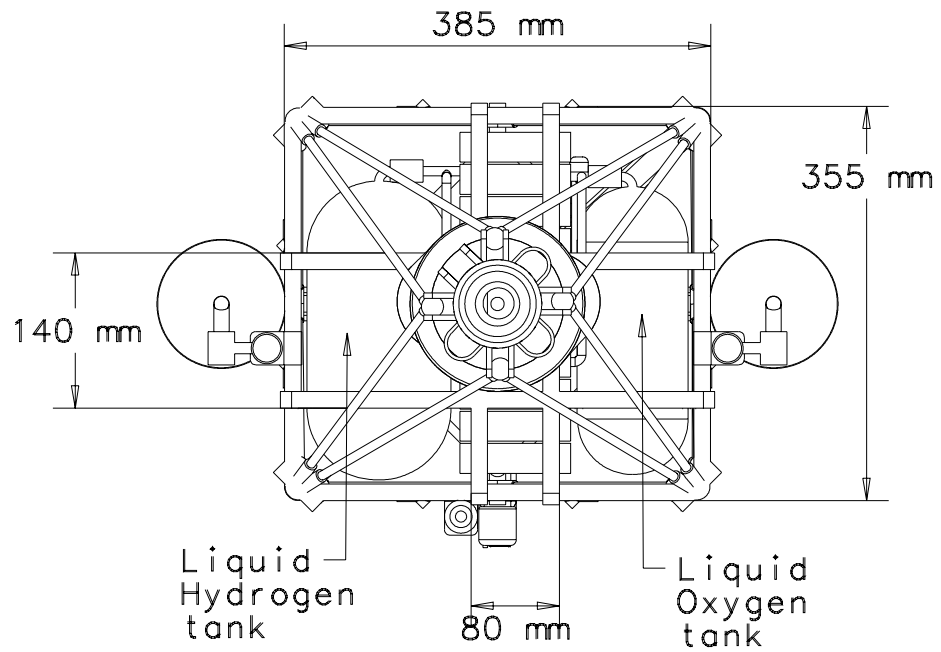
<b>Performance at mission gross take off mass</b>	Maximum cruise speed	11.5 m/s	
	Maximum vertical rate of climb	2.5 m/s	
<b>Power plant PEM Fuel cell stack</b>	Range	25 km	
	Endurance	39 minutes	
	Average power output	4.63 kW	
<b>Mass</b>	Maximum power output	6.43 kW	
	Maximum take off mass	50 kg	
<b>Major dimensions</b>	Payload	10.8 kg	
	Deployed	Rotor diameter	4266 mm
		Height from ground level	1510 mm
	Retracted	Folded rotor diameter	1520 mm
		Height from ground level	1338 mm
Inter rotor spacing	340 mm		



**THE MARTIAN AUTONOMOUS ROTARY-WING VEHICLE (MARV)**







# 1 INTRODUCTION

This proposal details the Martian Autonomous Rotary-wing Vehicle (MARV), an autonomous rotorcraft designed for Martian exploration. The MARV was designed in response to the request for proposals (RFP) from the American Helicopter Society as part of their 2000 Student Design Competition. This RFP for an autonomous rotorcraft identified a number of key requirements for the design: the vehicle must demonstrate one complete startup, takeoff, flight, and subsequent landing routine; the maximum vehicle mass be no greater than 50 kg; the vehicle must maintain controlled sustained flight for no less than 30 minutes; the range should be at least 25 km; and it must demonstrate a controlled hover for no less than one minute.

These are very challenging and unique design requirements. The average density in the Martian atmosphere is almost one one-hundredth of that on Earth at sea level. This produces flight Reynolds numbers and dynamic pressures one or two orders of magnitude lower than that seen on Earth. As a result, generating aerodynamic force becomes very difficult. This in turn requires a blade design that maximizes blade Reynolds number. Since there is not such a consideration on Earth, a different approach must be taken for blade design and this leads to planforms and airfoil profiles which are much different from the norm on Earth. In addition, the very low ambient Martian temperature makes the local speed of sound substantially lower, placing a limit on tip speed and as such on forward flight speed.

The primary goal of the design of the MARV was to develop a rotorcraft which could carry the maximum payload for the specified maximum gross weight, over a period of 30 minutes and for a range of at least 25 km. The final design satisfies all these requirements: the MARV can carry 10.8 kg of payload over a range of 25 km in 39 minutes, make a soft landing, shutdown, re-start, and take off again and fly a short distance.

## 2 FEASIBILITY STUDY FOR A ROTORCRAFT ON MARS

To design a rotorcraft for Mars one must first assess the impact of the different atmospheric conditions on the basic aspects of its flight. Next, one must identify a suitable means of propulsion. When basic flight capabilities are proved and a suitable power system identified, the feasibility of flying a rotorcraft on Mars is established. Once feasibility is established, detailed design can begin.

We begin by comparing the basic atmospheric characteristics between Earth and Mars. We identify the design issues that arise out of such differences. The unique requirement of carrying the rotorcraft to Mars poses additional, significant challenges. We demonstrate rotorcraft flight capability and estimate hover power. We prove the feasibility of designing a suitable power source with current technology. Finally we conclude that it is feasible to have rotorcraft flight on Mars.

### 2.1 Comparison of basic atmospheric characteristics

Table 2.1 compares the key atmospheric parameters on Earth and Mars. The values in the fourth column are used for design. They incorporate the RFP required 20% knockdown factor on density and pressure.

Physical parameters	Earth	Mars	Design value
gravity	$g$ (9.81 $m/s^2$ )	0.373 $g$ (3.66 $m/s^2$ )	3.66 $m/s^2$
pressure	$p$ (1.0135e5 Pa)	0.0078 $p$ (790.53 Pa)	632.42 Pa
temperature	288.16 K	210.56 K	210.56 K
density	$\rho$ (1.225 $kg/m^3$ )	0.0136 $\rho$ (0.0167 $kg/m^3$ )	0.0133 $kg/m^3$
viscosity	$\mu$ (1.789e-05 kg/ms)	0.721 $\mu$ (1.289e-05 kg/ms)	1.289e-05 kg/ms

Table 2.1: Comparison of atmospheric properties

### 2.2 Critical design issues

The Martian atmosphere generates unique design problems. Additional challenges are posed by the requirement of carrying the rotorcraft to Mars. Here we identify the critical design issues:

1) For the same vehicle mass the weight is 3 times less than it is on Earth. However, the atmospheric density is 100 times less than that on Earth. Hence assuming airfoil behavior on Mars to be comparable to that on Earth, five times more surface area is needed to generate the required amount of lift.

2) For the same speed and characteristic length the Reynolds number is 0.019 times that on Earth. The Mach number is 0.7 times that on Earth. Hence we have a low Reynolds number problem with no significant relaxation on the compressibility margin. In fact compressibility margins are more stringent for low Reynolds number flows.

3) Lock number is low due to very low density. This is important for the agility of the rotor system, for disturbance correction as well as maneuvers.

4) At low Reynolds numbers the aerodynamic capability of an airfoil is very sensitive to contour. This limits In Ground Effect hover capability in view of the dusty Martian surface.

5) Design robustness is a critical consideration for sustained controlled flight in the windy Martian environment.

6) The temperature range is 140 – 290 K. The avionics box must be heated along with any temperature sensitive components like lubricants and elastomers.

7) Mars has only 0.13% oxygen in its atmosphere. Hence, standard air breathing propulsion schemes used on Earth will not work. An innovative power plant design is essential for maximum payload capability. In view of the enormous cost of such a mission, maximizing payload capability is the most important design objective.

8) The design must be easily folded and simple to deploy. It must not call for drastic changes in current lander designs.

9) The structure must be made as light weight as possible, as this will determine payload capability.

10) In absence of satellites in orbit or repeater stations on the ground, a communications system must be designed for effective data transfer from the vehicle to the lander.

## 2.3 Demonstration of flight capability and estimation of hover power

**Problem definition** The flight capability of the vehicle is determined qualitatively by the maximum lift coefficient needed from airfoils to enable the vehicle to hover. Next, power required to hover is determined.

**Methodology** Gross vehicle weights from 0 – 50 kg were considered. The Martian environment was modeled as described in the RFP, including the knockdown factor. The following steps were performed:

1) Momentum theory calculations were performed in hover.

2) Detailed blade element calculations were performed in hover. Low Reynolds number and Mach number effects are incorporated. Flight capability is proved. Next, actual airfoil data was incorporated into the calculations. Finally, the power and torque requirements in hover are found, and are used for determination of a power source since these requirements are highest in hover.

**Results** In Step 1, a tip Mach number of  $M_{tip} = 0.5$ , solidity of 0.25, vehicle mass of 50 kg and a constant drag coefficient value of  $C_{do} = 0.038$  were assumed. Calculations were performed for different values of rotor radius. A single main rotor was assumed. The purpose of this analysis was to determine the power requirement in hover and the mean lift coefficient capability demanded of the airfoils. A relatively high  $C_{do}$  was chosen because of the low Reynolds number effect. From the left graph in Fig. 2.1, we conclude that the average value of  $C_l$  required is high but not impossible to achieve.

In Step 2, detailed blade element calculations showed the effects of blade taper and twist distribution on the aerodynamic loading at each spanwise section and on the overall rotor figure of merit. First a linear lift-curve slope and constant drag were used, taken as 5.57 and 0.038 respectively. The spanwise distribution of lift coefficients required is a practically realizable range with currently available airfoils, as shown on the right in Fig. 2.1. Thus, the feasibility of flying a rotorcraft on Mars is established. Based on these lift requirements, an airfoil was initially chosen. The experimental lift, drag and moment curves of the airfoil were then incorporated into the blade element calculations. Also, it was found that the payload fraction stayed nominally constant above a minimum gross weight, and thus it was decided to maximize the payload. This led to the initial choice of a rotor radius of 3.05 m (10 ft) and a vehicle mass of 50 kg. From this it was found that the power required to hover would be approximately 5 kW, and that the torque requirement was approximately 127 Nm.

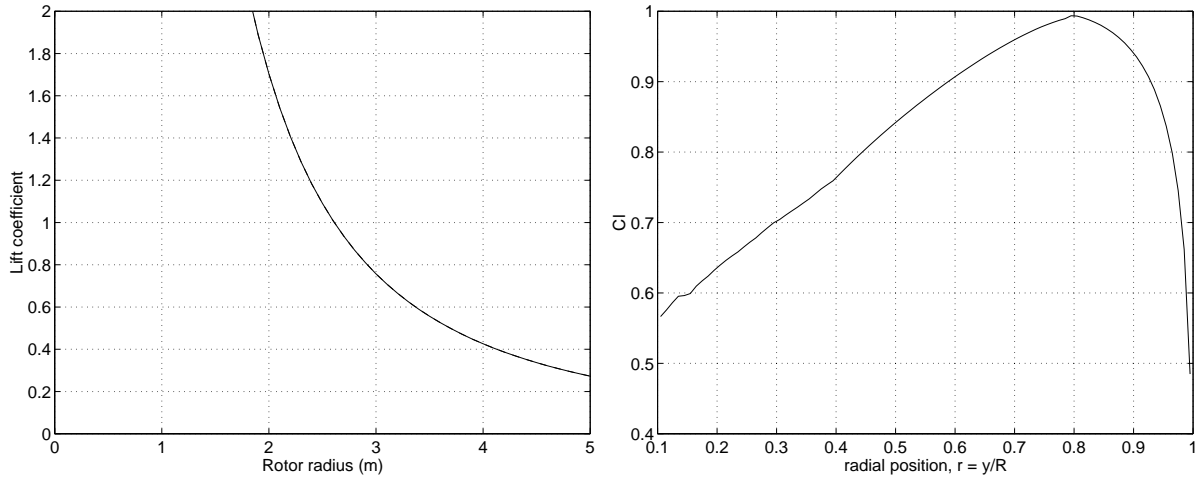


Figure 2.1: Required mean lift coefficient versus rotor radius

## 2.4 Availability of power

Once flight capability is demonstrated, the next step is to examine whether the power requirement can be met. A detailed discussion on propulsion options is given in the power plant selection chapter. Here, only the feasibility of obtaining a required power source is proved. No technological forecast has been relied upon for this purpose.

**Methodology** For a 50 kg total vehicle mass and a rotor radius of 10 ft, the minimum power required to hover was approximately 5 kW. For the feasibility study we assumed an increased value of 6 kW continuous for 30 minutes duration. This gives a total mission energy requirement of 3000 Watt-hour (Wh), where  $1 \text{ Wh} = 3.6 \text{ kJ}$ . If the mass of an energy source which can supply 3000 Wh of energy is less than the vehicle take off mass, then the feasibility of providing sufficient power is established.

**Results** A hydrazine-fueled piston type engine [1] has, in its current form of implementation, a specific fuel consumption (SFC) of 1.01 kg/MJ. The fuel requirement for such an engine for our mission would be 10.8 kg. Currently developed lithium ion rechargeable batteries for vehicle traction have specific energy value of 150 Wh/kg [2]. At this rate a battery mass of 20 kg would be required. Investigation into currently available electric motors show that it is possible to obtain brushless direct current electric motors in the 6 kW power and 127 Nm torque range within 2 to 3 kg [3]. The Pathfinder lander had Gallium Arsenide solar cells on Germanium substrate (GaA/Ge Cells). They recorded energy absorption levels on the order of 3888 kJ per day [43]. At this rate a rechargeable battery as above can be recharged in a little less than 4 days and multiple missions can be flown. We conclude from the above figures that it is feasible to supply the required power.

## 2.5 Communication between vehicle and lander

Data transfer, navigation and guidance of a helicopter on Mars are important issues. There is no GPS system on Mars, nor are there any repeater stations. Even if there were, Mars has not a significant ionosphere off of which to bounce signals. Hence direct Line-of-Sight contact between the helicopter and the lander must be maintained. The detailed design of our communication system is provided in the section on avionics. Here we simply state that an effective communication system has been designed for this application.

## 2.6 Results of feasibility study

As a result of the feasibility study we have established the following:

- 1) Rotorcraft flight on Mars is feasible with current low Reynolds number aerodynamic knowledge.
- 2) It is feasible to develop a suitable power plant to power the vehicle for 30 minutes. Such a power plant can be built by innovative utilization of current technology.
- 3) Design of the communication system over a range of 25 km needs to be addressed.

## 3 MISSION PROFILE

A mission profile that meets all of the performance requirements specified in the RFP has been formulated. The profile can be split into the basic mission, which meets all the basic RFP objectives, and the extended mission, which meets additional objectives of the RFP.

The two missions will be described in this chapter. The objectives of each mission will be given, followed by the step-by-step mission profiles. At each of the mission legs, it will be shown how each objective is met. The total energy required for the basic and extended missions is then calculated from the mission profile. Finally, our mission flexibility will be discussed, and our alternate mission capabilities will be described.

### 3.1 Mission objectives

The Mars mission objectives given in the RFP are summarized in Table 3.1.

Requirement	Reference
Autonomous deployment	RFP 1.2.8
25 km range	RFP 1.2.2
30 min controlled flight	RFP 1.2.2
1 min hover	RFP 1.2.10
100 m max altitude	RFP 1.2.3
Restart capability (3 min)	1.2.4 (preferable)

Table 3.1: Mission objectives

### 3.2 Preferable mission parameters

The following objectives have been deemed preferable by the design team:

- 1) A restart and repositioning of the helicopter after it has completed the basic mission. This has been listed as preferable in the RFP.
- 2) To minimize the power requirement, the helicopter will spend most of its time in cruise.
- 3) Perform climb and descent at maximum forward flight speed, minimizing power required.
- 4) Power from the lander is used to start up the rotor, as well as during pre-flight system checks. This is listed as acceptable in the RFP (section 1.2.9).
- 5) A climb to 100 m will be included, since this will prove the MARV's climb capabilities.
- 6) To prove independence of it, the hover will be performed out-of-ground-effect (OGE).

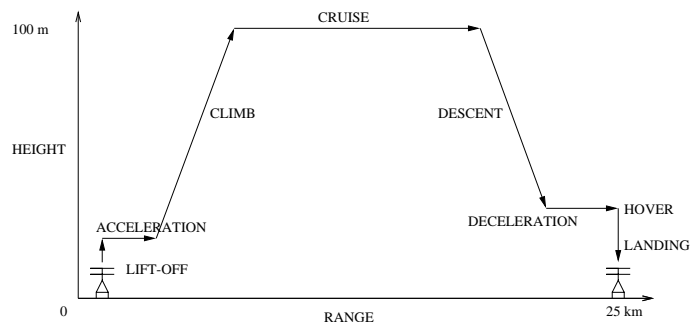


Figure 3.1: Basic mission profile

### 3.3 Mission profile

The basic mission profile is shown in Fig. 3.1. The steps are as follows:

A specific deployment scheme has been designed, which frees the helicopter from the lander, and fully deploys its pre-folded blades. This **initial deployment** procedure is detailed clearly in the blade deployment chapter.

Once fully deployed on the lander, the helicopter can begin its **pre-flight autonomous system checks**. This will consist of the following processes:

- All sensors should begin monitoring the local atmosphere and the internal conditions of the helicopter.
- The heating system should be tested and determined to be fully operational.
- The fuel cells and motors will be run, with power and rotor RPM monitored by the onboard sensors.
- Each directional antenna will be traversed its full 180 degrees, and transmissions from the omnidirectional antennas will be tested.
- The orientation of the helicopter (vertical axis must be vertical) will be checked.
- The blades will be checked to ensure they are fully deployed and locked in position.
- The landing gear will be checked to ensure it is fully extended.

Once a full system check is performed, the lander should transmit data to Earth, informing mission control that it has landed and deployed successfully. Mission control on Earth can then give the go-ahead to begin the mission. Using power from the lander (battery, solar cells, etc.), the rotor blades will be spun up to the full RPM. A low blade pitch will be maintained until the rotor is fully up to speed.

Following the spinup of the rotors and the system checkout, MARV will be ready to **take off**. The power from the lander will be disconnected, and power will now be provided by the helicopter's internal power source. An initial vertical lift-off will be performed to clear obstructions, such as antennas on the lander. The mission profile specifies a 5 m height for this vertical climb. This will be high enough to clear above the lander antenna mast, which will then extend to its full 3 m height (see the avionics chapter). Thirty seconds are allowed for this procedure, allowing diagnostic programs in the flight computer to perform final pre-flight checks. If any errors are encountered during lift-off, it will be possible for the helicopter to land back down in or near the lander without difficulty.

**Acceleration** will be performed following the initial takeoff of the helicopter. Acceleration in this fashion is performed by pilots on Earth as well, mainly for safety reasons (autorotation), and also for the purpose of reducing the power required for flight. Sixty seconds will be allotted for the acceleration to our maximum forward speed of 11.5 m/s ( $\mu = 0.08$ ). During this time the helicopter will travel approximately 345 m.

After full acceleration to maximum speed, a **climb** to altitude will be performed. The climb will be to a height of 100 m, to prove the climb capabilities of the helicopter. This will take approximately 37 seconds, this

being determined by assuming that 10 percent more power will be added for climb. This results in a maximum climb velocity  $V_c = \Delta P/W = 2.5142$  m/s. During this time the MARV will travel approximately 437 m. We have limited the climb rate to one-third of the highest possible value (as shown in the performance chapter) to ensure that the airfoils do not stall.

**Cruise** will then be performed at the 100 m altitude, both to ensure line-of-sight communication with the lander and to maximize the MARV's ability to take aerial photographs, and possibly recognize landmarks or other items of interest. This cruise portion will last approximately 34 minutes, and cover a distance of at least 23.459 km. The other components of the mission provide the remaining 1.541 km. This distance meets the 25 km range objective, as well as the 30 minutes sustained controlled-flight objective. This can be seen in Table 3.2 below.

Near the end of the flight, the helicopter will approach to a landing as would be done on Earth. **Descent** will be performed at speed, to minimize power. It will last roughly 36 seconds, and proceed to a height of 10 m above the ground. This time was determined assuming the descent rate would be the same as the climb rate. During this time the helicopter will travel approximately 414 m.

The **deceleration** portion of the flight will be the reverse of the acceleration portion. The helicopter will slow from maximum speed to a hover. Sixty seconds will again be allowed for this procedure. After a full deceleration, the helicopter will be in a hover in the target area. During this time the helicopter will travel approximately 345 m.

Following the full deceleration, the MARV will **hover** for 60 seconds, as required by the RFP. The hover portion of the flight was designed to be at the end of the flight, because it is expected that the landing site is an area to be studied. It will be performed at a height of 10 m, for the dual purpose of providing a good aerial view for photography and to prove that the MARV has hovering ability OGE.

The helicopter will then descend to a soft **landing**. It will do so slowly and carefully, so that it lands properly on its landing legs. Thirty seconds will be allowed for the 10 m descent.

After a soft landing, the MARV will cut **shutdown** and power to its rotors. Avionics will continue to be supplied with power, to enable post-flight checks and telemetry transmission back to the lander.

### 3.4 Basic mission power/energy requirements

The total mission energy requirements have been determined stage by stage, as shown in Table 3.2. Each stage requires a different amount of power and is of a different duration. The energy required for each stage is subsequently calculated by  $E = P * \Delta t$ . This calculated total energy will later provide us with the necessary power supply size and type.

### 3.5 Extended mission

This section will detail the planned extended mission, which fulfills objectives beyond the basic requirements of the RFP. As detailed above, after the completion of the basic mission, the flight computer will shut down the helicopter. After a period of time, the helicopter will restart and perform a second flight.

This mission is a 3 minute flight, of approximately 200 m. It will demonstrate a restart capability, which greatly increases the mission flexibility, by allowing scientists to send the helicopter to a second landing site of interest. The extended mission profile can be seen in Fig. 3.2.

The extended mission begins with a **restart** of the rotor, using the power provided by the helicopter fuel cells. Low pitch will be maintained until the rotor is up to speed. It is also suggested that the same pre-flight

No.	Description	Duration	$\mu$	Distance	Avg. Power	Energy Req.
1	Rotor spinup	-	0	0	-	0
2	Takeoff to 5 m	30 sec.	0	0	5.369 kW	47.73 Wh
3	Acceleration	60 sec.	0-0.08	345 m	4.74 kW	79 Wh
4	Climb to 100 m	38 sec.	0.08	437 m	4.6 kW	53.41 Wh
5	Cruise	2040 sec.	0.08	23459 m	4.6 kW	2607 Wh
6	Descent to 10 m	36 sec.	0.08	414 m	4.6 kW	41.4 Wh
7	Deceleration	60 sec.	0.08-0	345 m	4.74 kW	79 Wh
8	Hover	60 sec.	0	0	4.88 kW	81.33 Wh
9	Landing	30 sec.	0	0	4.392 kW	36.6 Wh
TOTAL		39.23 min.	-	25 km	-	3025.47 Wh

Table 3.2: Basic mission energy requirements

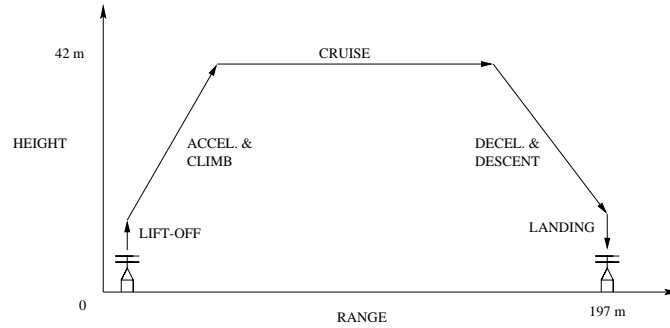


Figure 3.2: Extended mission profile

system checks be performed before the ‘restart’ flight as were performed before the ‘basic’ flight. These checks have been detailed above.

A short vertical **takeoff** will then begin. This will allow the helicopter to clear above any obstacles which may hinder its acceleration to forward flight. Fifteen seconds will be allowed for this climb, which will take the helicopter up to a height of approximately 5 m.

**Acceleration and climb** to a higher altitude will occur concurrently in the extended mission. A total of 15 seconds will be allowed for the acceleration and climb. It is notable that this does not accelerate the helicopter to its maximum forward flight speed. This is because a full acceleration time, as set forth in the basic mission, requires too much time. Since the entire extended mission is designed for a short 3 minutes, a full period of acceleration as in the basic mission was not planned here. The same climb rate as in the basic mission will be assumed here. This results in a final altitude of approximate 42 m. This height has been accepted by the design team as high enough for any probable scientific studies.

By the end of the acceleration/climb mission leg, the helicopter will be at a slow **cruise** speed of  $\mu = 0.01$ . Such a slow forward speed does not introduce any significant power reduction. However, due to the short duration of the cruise period, this is no significant waste of energy. A 120-second cruise flight will then be performed, which will cover a distance of roughly 175 m. The direction and nature of this cruise flight will be at the discretion of mission control. A new target may be set which is a short distance away, or a circle route could be performed over the basic mission target area.

After the cruise portion of the flight is complete, the helicopter will then **decelerate and descend** for a

landing. This deceleration/descent will be performed concurrently, similar to the acceleration/climb mission leg. After descent to hover, the helicopter will land softly on the ground.

### 3.6 Extended mission power/energy requirements

Table 3.3 details the specifications of the extended mission. The extended mission energy requirements have been determined stage by stage, as was performed with the basic mission. The energy required for each stage is subsequently calculated by  $E = P * \Delta t$ . This calculated total energy will later provide us with the necessary power supply size and type.

No.	Description	Duration	$\mu$	Distance	Avg. Power	Energy Req.
1	Takeoff to 5 m	15 sec.	0	0	5.369 kW	22.37 Wh
2	Acceleration / climb	15 sec.	0-0.01	11 m	4.88 kW	20.33 Wh
3	Cruise	120 sec.	0.01	175 m	4.88 kW	162.67 Wh
4	Descent / Deceleration to 5 m	15 sec.	0.01-0	11 m	4.392 kW	18.3 Wh
5	Landing	15 sec.	0	0	4.392 kW	18.3 Wh
TOTAL		3 min.	-	197 m	-	241.97 Wh

Table 3.3: Extended mission energy requirements

Our helicopter is designed to fly both the basic and the extended missions. Based on our calculations, the total energy required to perform both missions is 3267.44 Wh.

It is understood that certain assumptions of duration, speed, and course have been made in the design of this mission profile. Deviation from this mission profile due to gusts or poor control response will result in a longer flight duration, and thus a greater energy requirement. For this reason we have added an 10% of the mission energy, providing a total of 3594.84 Wh of energy in the fuel cells.

### 3.7 Alternate missions

The above basic mission profile was designed with the primary aim of fulfilling all RFP mission objectives, with less emphasis on providing a flexible, applicable mission capability. It is most likely that mission scientists will want the ability to customize the mission with various turning, landing, climb/descent, and hover stages.

**Sample-Return Mission:** The ‘sample-return’ mission is one in which the helicopter flies out a distance, collects a soil sample, and returns to the lander. In our analysis, we determined the maximum distance our helicopter could travel in a sample return mission. We have assumed the same amount of total energy available as was provided for the basic plus extended missions. We have also assumed that the only objective of this mission is maximum range. Thus we do not include a hover stage. As was done in the basic and extended missions, a 10 percent ‘buffer’ was accounted for in the energy requirement. The results of this analysis are shown in Table 3.4. As we see, our maximum range for a sample-return mission is 13.341 km.

**Long-Range Reconnaissance:** In this section, an alternate, longer range mission is examined. It is assumed that in this case MARV’s sole purpose is to conduct long-range reconnaissance photography and atmospheric analysis. The available scientific payload is therefore replaced by more energy capacity. The results of this can

be seen in the payload/range curve, Fig. 19.4 (see performance chapter). We can see from the curve that the maximum total range of the helicopter is approximately 120 km.

No.	Description	Duration	$\mu$	Distance	Avg. Power	Energy Req.
1	Lift-off to 5 m	30 sec.	0	0	5.369 kW	47.73 Wh
2	Acceleration	60 sec.	0-0.08	345 m	4.74 kW	79 Wh
3	Climb to 100 m	38 sec.	0.08	437 m	4.6 kW	53.41 Wh
4	Cruise	1009 sec.	0.08	11.8 km	4.6 kW	1290 Wh
5	Descent to 10 m	36 sec.	0.08	414 m	4.6 kW	41.4 Wh
6	Deceleration	60 sec.	0.08-0	345 m	4.74 kW	79 Wh
7	Landing	30 sec.	0	0	4.392 kW	36.6 Wh
SAMPLE TOTAL		21.05 min.	-	13.341 km	-	1627.14 Wh
RETURN TOTAL		21.05 min.	-	-13.341 km	-	1627.14 Wh
MISSION TOTAL		42.1 min.	-	0	-	3254.28 Wh

Table 3.4: Sample-return mission energy requirements

## 4 SELECTION OF ROTOR CONFIGURATION

In this chapter we describe the steps leading to the selection of a coaxial 2-blades per rotor configuration. The selection of configuration is based on a systematic down selection strategy. A comparative study of the performance of different configurations to mission specific design criteria was made and the two rotor configurations respectively representing conventional main rotor/tail rotor and quad rotor were selected in the first round for further evaluation. An energy based performance analysis for a prescribed mission plan is conducted to further down select the final configuration.

### 4.1 Choice of candidate configurations and selection criteria

The design of a rotorcraft to fly on Mars imposes unconventional constraints on the configuration due to the low density of the Martian atmosphere and the intricacies of the mission plan. Brainstorming sessions generated a number of candidate configurations and also the criteria for evaluating their suitability. Table 4.1 shows the selection criteria and their respective weightage.

The volume inside the lander module housing the rotorcraft for a mission to Mars is restricted. Hence the foldability of the rotorcraft is a primary design criteria. As the aircraft is to be of autonomous nature its reliability also is an important consideration. Aerodynamic cleanliness, hover efficiency and cruise efficiency are included to determine the aircraft that is optimum for all the different flight regimes of the mission profile. As this would be the first rotorcraft to fly on Mars a technologically mature rotorcraft configuration would be a welcome option compared to an experimental configuration. A payload of scientific instruments has to be carried for a successful mission. Some configurations have greater restrictions on the sizes and shapes of the payload over others. Hence this criterion is also taken into consideration for final selection. The autonomous nature of the rotorcraft necessitates the inclusion of controllability and maneuverability also to the selection criteria. Simplicity of the overall structure and control system also have to be considered for final selection.

Selection Criteria	Weight
Compactness of folding	10
Reliability	10
Controllability	8
Aerodynamic cleanliness	6
Maturity of technology	10
Hover efficiency	8
Aerodynamic interaction	3
Vibration	8
Cruise efficiency	7
Maneuverability	3
Ease of payload packaging	9
Simplicity of structure	10
Simplicity of control system	8

Table 4.1: Selection criteria

Schematics of 15 different candidate rotorcraft configurations are given in Figs. 4.1 to 4.4. They are classified as single rotor, twin rotor, quad rotor and hybrid configurations. Additional configurations tailored to the mission plan are shown in Figs. 4.6 and 4.5. Different aspects of the final design and deployment mechanism were adapted from these schematic designs. Tables 4.2 to 4.5 show comparative rankings of different configurations based on the selection criteria and their weight shown in Table 4.1.

Weight	Selection Criteria	Conventional (T/R)	Ducted w/ 2 propellers	Ducted w/ slipstream vanes	Tip-jet rotors
10	Compactness of folding	1	2	2	1
10	Reliability	9	5	3	5
8	Controllability	5	3	1	1
6	Aerodynamic cleanliness	8	2	2	3
8	Maturity of technology	10	2	5	2
8	Hover efficiency	10	7	3	8
3	Aerodynamic interaction	7	10	10	9
8	Vibration	1	2	6	3
7	Cruise efficiency	7	4	1	4
3	Maneuverability	5	1	1	3
9	Ease of payload packaging	10	5	1	10
10	Simplicity of structure	8	2	5	10
8	Simplicity of control system	6	2	2	6
	Total	659	336	297	492

Table 4.2: Single rotor configurations (Fig. 4.1)

## 4.2 Evaluation of the configurations

**Single rotor configurations:** The single rotor configurations studied are conventional main rotor/tail rotor configurations, ducted rotors with vanes in the slipstream for providing anti-torque [5], ducted main rotor with

Weights	Selection Criteria	Side by side	Tandem	Coaxial	Ducted coaxial
10	Compactness of folding	2	2	10	2
10	Reliability	8	8	8	10
8	Controllability	5	5	7	5
6	Aerodynamic cleanliness	6	6	8	2
8	Maturity of technology	9	10	10	8
8	Hover efficiency	10	10	8	8
3	Aerodynamic interaction	10	10	7	7
8	Vibration	2	2	1	2
7	Cruise efficiency	6	6	8	6
3	Maneuverability	4	4	3	3
9	Ease of payload packaging	10	10	10	8
10	Simplicity of structure	8	8	10	8
8	Simplicity of control system	6	6	6	6
	Total	646	654	760	588

Table 4.3: Twin rotor configurations (Fig. 4.2)

Weights	Selection Criteria	Quad-rotor (shrouded)	Quad-rotor (free)	Six rotors
10	Compactness of folding	8	8	1
10	Reliability	9	9	1
8	Controllability	8	10	8
6	Aerodynamic cleanliness	1	2	1
8	Maturity of technology	2	5	1
8	Hover efficiency	8	8	7
3	Aerodynamic interaction	7	7	3
8	Vibration	2	2	2
7	Cruise efficiency	5	5	4
3	Maneuverability	9	9	10
9	Ease of payload packaging	8	8	7
10	Simplicity of structure	5	7	3
8	Simplicity of control system	10	10	4
	Total	621	687	362

Table 4.4: Multi-rotor configurations (Fig. 4.3)

propellers for anti-torque and forward speed [6] and tip-jet driven rotors [7]. The first three of these configurations have been successfully tested for Earth-based UAVs [8, 5, 9, 10].

From Table 4.2 it is clear that the conventional main rotor/tail rotor configuration is the best choice among the four configurations. Though compactness in folding is adversely affected by the large size of the rotor required, the maturity of technology and aerodynamic efficiency favor the conventional configuration. Tip-jets, though attractive due to their simplicity of structure and ease of payload packaging due to the absence of powerplant inside the fuselage, have the drawbacks of lower controllability and lack of compactness in folding. The lower controllability of tipjets may be attributed to the lower Lock number of the blade due to the high blade inertia resulting from blade mounted nacelles.

Weight	Selection criteria	rotor wing	tilt rotor	tilt wing	joined wing
10	Compactness of folding	1	2	2	1
10	Reliability	1	3	3	1
8	Controllability	1	5	5	3
6	Aerodynamic cleanliness	6	2	4	10
8	Maturity of technology	2	7	6	1
8	Hover efficiency	1	3	5	2
3	Aerodynamic interaction	7	3	3	1
8	Vibration	8	6	6	10
7	Cruise efficiency	8	10	10	4
3	Maneuverability	1	4	4	10
9	Ease of payload packaging	10	10	10	8
10	Simplicity of structure	1	1	1	3
8	Simplicity of control system	1	1	1	3
	Total	332	421	441	344

Table 4.5: Other helicopter configurations (Fig. 4.4)

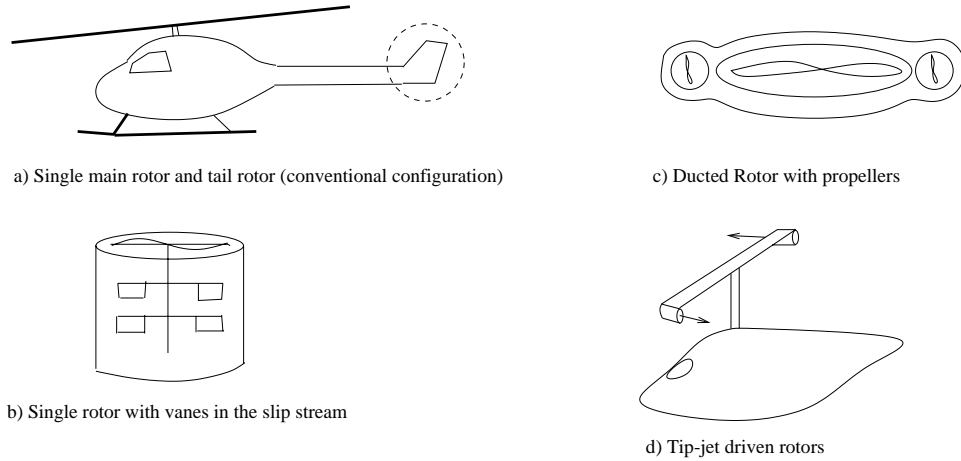


Figure 4.1: Single rotor configurations

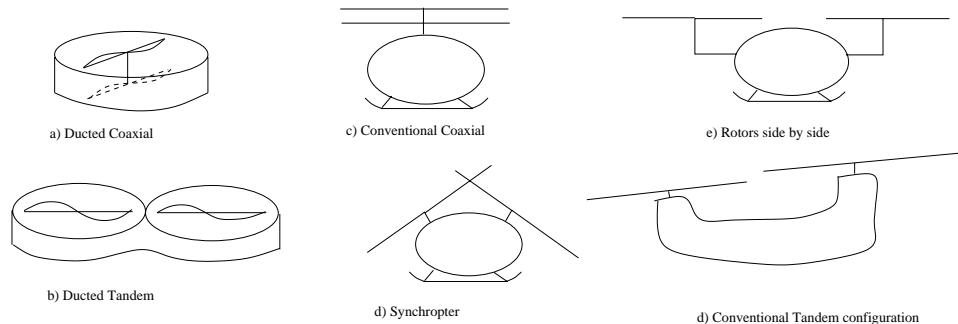


Figure 4.2: Twin rotor configurations

**Twin rotor configurations:** Four twin rotor configurations were analyzed: side-by-side rotors, tandems (eg. Boeing Chinook), coaxials (Kamov, Sikorsky ABC) and ducted coaxial configurations (Sikorsky Cypher). Tandem helicopters have not been used for UAV or radio control helicopter designs. Coaxial configurations are

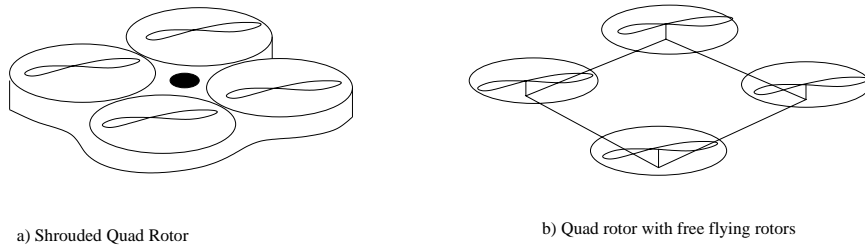


Figure 4.3: Quad rotor configurations

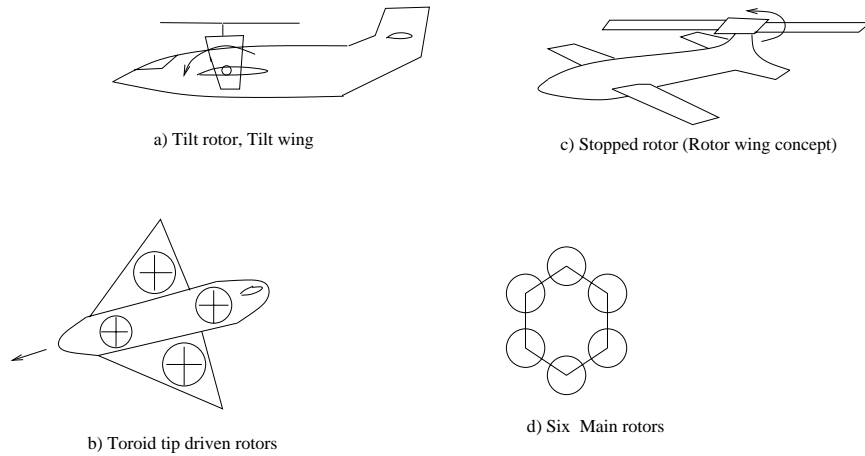


Figure 4.4: Other flying/tested rotorcraft configurations

the most widely used configurations for UAV design [11]. Sikorsky's Cypher and Cypher II [12], which have ducted coaxial configurations, are some of the most successful UAV designs.

The coaxial design is favoured by most of the key design criteria and has received the highest number of points in the points table (Table 4.3). Side-by-side and tandem configurations also received comparable ratings. The difficulty of folding and the complexity of the structure are among the key drawbacks of these configurations. Ducted coaxial configurations, though well suited for earth based UAVs, have significant compactness problems for a Mars based mission. The low density flow field necessitates large rotor diameters to produce the required amount of lift. Such big rotor diameters and shrouds cannot be folded efficiently to package it inside the Mars lander.

**Quad rotor and other rotor configurations:** Recently there has been an interest in the rotorcraft industry in designing rotorcraft with four or more lifting rotors. Such configurations could be controlled by varying the RPM of different rotors to change the direction of the thrust vector. Also gyros could be used to establish stability in forward flight. Some of the tested configurations are the Mesicopter [13], Gyronsaucer [14] and Roswell Flyer [15]. The latter two are RC helicopters and are reported to have very good controllability. The former (Mesicopter), a meso-scale flying machine which is no larger than a penny, is still in the development stage. Also, a six rotor version of the Mesicopter is proposed to improve its controllability. The comparative table above indicates that a quad rotor design with free flying rotors has good potential to meet the design criteria. Free flying rotors are generally better than their shrouded counterparts in their simplicity of structure and aerodynamic cleanliness.

**Hybrid helicopter configurations:** The candidates in the compound helicopter category are a rotor wing or stopped rotor [16], tilt-rotor (XV-15), tilt-wing and joined wing, toroid rotor configurations [17]. All these designs suffer from foldability problems because of the large size of their wings. They are well suited for payload packaging and also very effective in high speed forward flight conditions. However, as the mission plan does not require high speed forward flight, these designs may not be suitable options as configurations for MARV.

### 4.3 Down selection

Comparative tables show that the quad rotor and coaxial designs are the best candidates for the present design problem. The coaxial design has the advantages of compactness and ease of deployment while the quad rotor is superior from a controllability view point. Both designs are complex mechanically. Maturity of technology favors the coaxial design while innovation favors the quad rotor. Further downselection of the most suitable design between the quad rotor and coaxial configurations is desired. A trade study based on aerodynamic performance was conducted between these two configurations to determine the downselection to a single configuration for further detailed design.

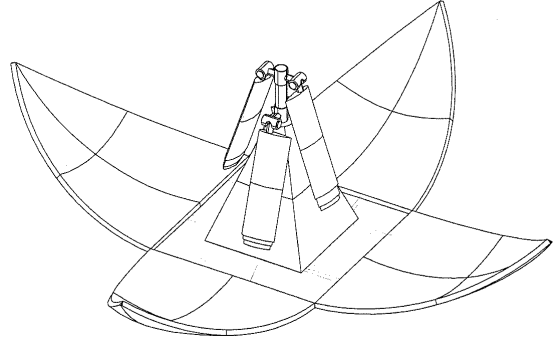


Figure 4.5: A coaxial configuration

## 4.4 Coaxial and quad rotor trade off studies

### 4.4.1 Trade study methodology

The configuration which results in the highest payload must be chosen as the final configuration. Energy consumed by a given configuration to complete a mission determines the amount of the power source (battery in our case) required to complete the mission. The weight of the battery and other configuration specific infrastructure required determines the amount of payload. The energy required for the vehicle of a specific configuration to complete a prescribed mission profile is estimated. A blade element/momentum model is used for performance estimation. Blades of rectangular planform and linear twist are assumed to simplify the computations. The lift characteristics of the airfoil based on experimental and CFD data was included using a suitable regression model. As the weight of the rotorcraft is not specified, the analysis is conducted for take off weights ranging from 1-50 kg and the weight which provides the highest weight of payload is chosen as the design weight. Further analysis on choosing the gross weight will be detailed in the weights section of this report.

### 4.4.2 Trade study results

The comparison of the energy required to complete the specified mission for the quad rotor and coaxial designs is shown in Fig. 4.7. The energy required dictates the weight of batteries required and hence affects the weight of payload which can be carried. It can be seen that the quad rotor consumes more energy than the coaxial for the same mission profile. The higher energy required may be attributed to two reasons. Primarily the lower Reynolds number causes an increase in the profile power consumed by the rotor. For generally constant overall vehicle sizes, the rotors of the quad rotor have much lower Reynolds numbers owing to lower chord values. Airfoil characteristics at lower Reynolds numbers show higher drag coefficients, lower maximum lift coefficients, and

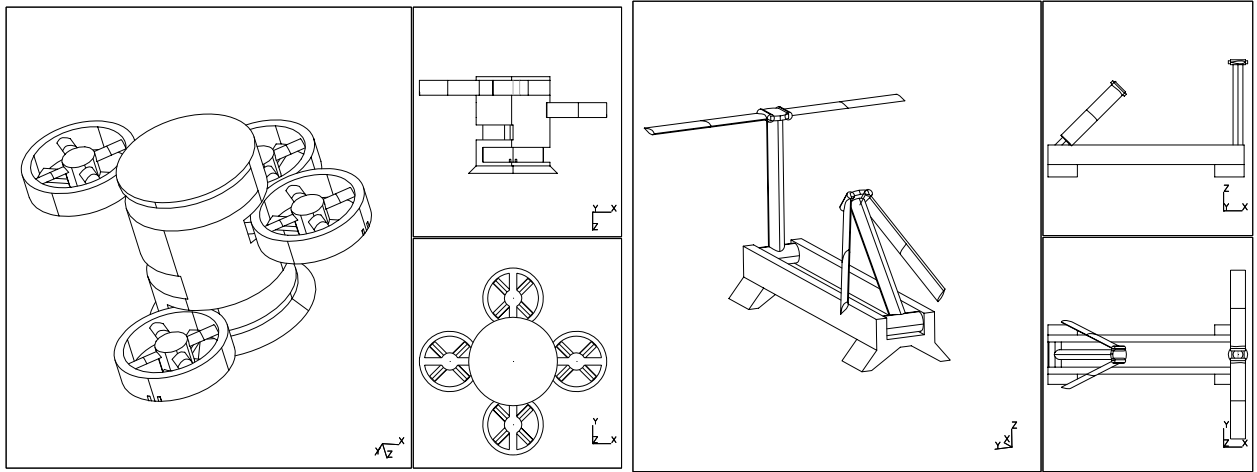


Figure 4.6: Two multi-rotor configurations

thus much lower lift-to-drag ratios. Additionally, later airfoil design work showed that in general, below Reynolds numbers of 50,000, it became extremely difficult to keep the boundary layer attached to the airfoil surface for more than a small distance along the chord, as turbulent separation would occur almost immediately after the trip transitioned the boundary layer to turbulent flow. Thus at the Reynolds numbers expected on a quad rotor vehicle, the airfoils may always be stalled. Another cause of the higher energy requirement for the quad rotor is due to the higher parasitic drag of the quad rotor in forward flight because of its higher effective flat plate area. As energy and weight are very important parameters, it can be seen that the coaxial rotor is a better choice to fulfill the mission objectives. Even more important than this however, is the maturity of the technology of coaxial designs. Quad rotor development is still in its infancy and cannot be expected to be relied upon for such an exotic mission. For these reasons, the coaxial design was chosen over the quad rotor configuration.

#### 4.4.3 Selection of configuration

A trade study of different coaxial rotor configurations need to be conducted now to arrive at a final specific configuration. The main parameters of interest are the number of blades on each rotor and the control mechanism and the landing gear configurations. These have to be studied carefully before selecting the final specific configuration.

### 4.5 Coaxial trade off studies

#### 4.5.1 Number of blades

Most conventional coaxial configurations (Kamov and Sikorsky ABC) have three bladed rotors. The increase in number of blades alleviates the blade loading and hence the vibrations on the fuselage. Also it is generally found that the performance of rotors with higher number of blades is better than those with lesser number. Since our design goal is unconventional, a parametric study on the number of blades is conducted. The energy required for the mission profile specified earlier is used as the criteria for evaluating the performance. Equivalent solidity two-bladed and three-bladed rotors are used for comparison. From Fig. 4.8 it is evident that the three-bladed rotor needs 7% more energy than its two-bladed counterpart to complete the prescribed mission for all the take off weights studied. This is again attributed to lower airfoil performance as a result of the lower Reynolds number.

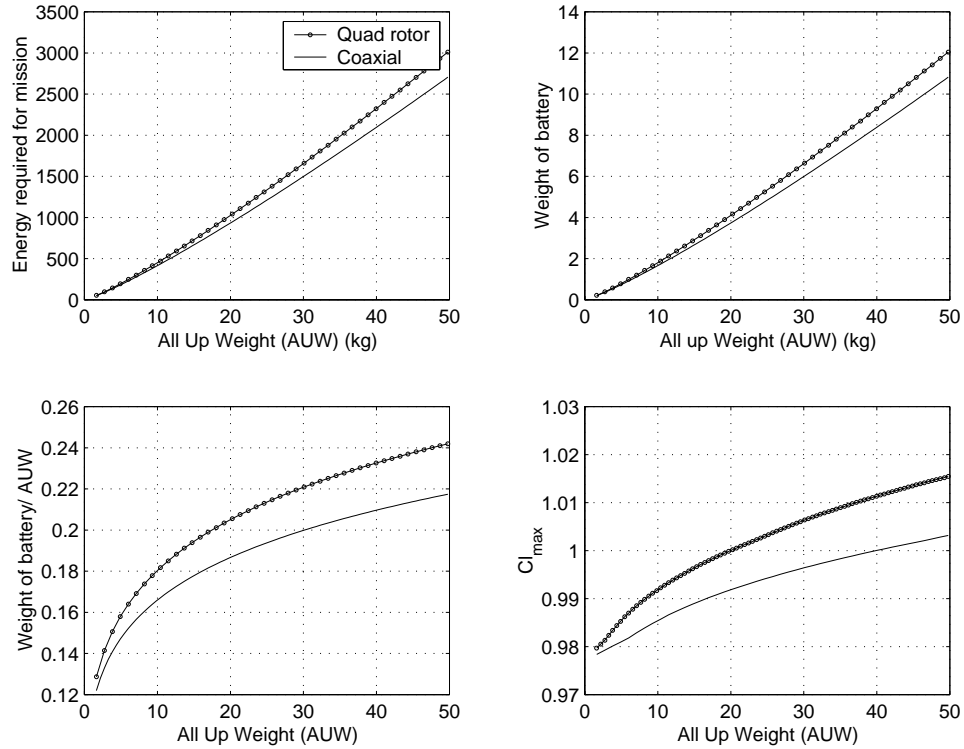


Figure 4.7: Performance comparison of coaxial and quad rotor designs

As the solidities of the two rotors are the same, the three-bladed rotor results in a smaller chord and hence lower Reynolds number that causes an increase in the drag coefficient and decrease in the lift to drag ratio. Also lower Reynolds numbers introduce a lower stall margin which might become prohibitive in climb and forward flight conditions. Based on these results, it was decided to use two blades per rotor for the final configuration.

#### 4.5.2 Control mechanism and landing gear

The candidates for the control mechanisms were conventional the swashplate mechanism, servo-flaps and an all-movable tip. We were expecting to use smart structures technology to implement servo-flaps and all movable tips. These had to be analyzed carefully in the light of the present design goal. Also the types and number of landing legs to be used and their deployment mechanisms were studied in detail. Since the trade off study between these different configurations is inseparable from the process of detailed design, the final down selection of each particular mechanism for these systems will be explained in their respective detailed design sections.

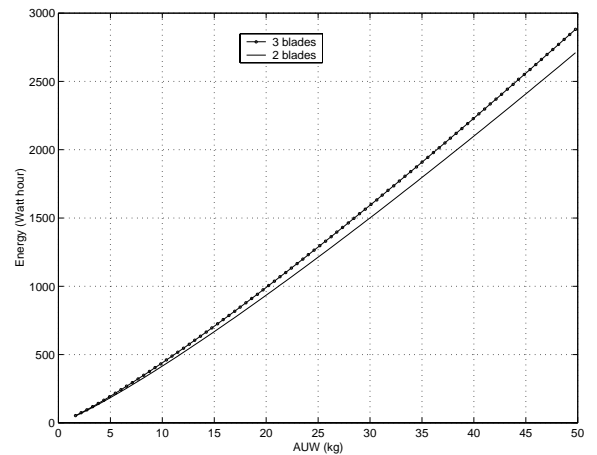


Figure 4.8: Performance comparison of 2-bladed and 3-bladed rotors of equal solidity

## 4.6 Summary

A coaxial 2-blades per rotor helicopter was chosen as the best configuration for the specified flight mission. This selection was based on a trade off study conducted by analyzing different rotorcraft configurations in the light of the present design constraints. The quad rotor and coaxial configurations showed promise in fulfilling many criteria of selection. A further downselection was made using a performance comparison for a specific mission profile which fulfills the requirements of the RFP. A parametric study of the number of blades was also conducted to choose the design which would give the best performance. This leads to the selection of the two-bladed rotor for the final configuration.

# 5 AERODYNAMIC DESIGN

## 5.1 Methodology

Since maximum power is needed in hover, it was decided to minimize the power required to hover while still maintaining good forward flight performance. Weight and packaging considerations onboard the Mars spacecraft dictate that size and thus rotor diameter be as small as possible. Producing the required lift with a minimum rotor disk area necessitates a high tip speed, which in the Martian atmosphere becomes a relatively high tip Mach number condition. To keep the power required low, solidity must be minimized and thus the blade loading must be high. Added to these considerations is the unusual requirement of sizing the rotor so that blade Reynolds number can be maximized, as the Martian atmosphere's low density makes the flight Reynolds number range one or two orders of magnitude below that encountered for helicopters on Earth. These unusual and often conflicting requirements show that the rotor planform and airfoil designs are very challenging tasks.

These requirements necessitated a rigorous and unconventional approach to the aerodynamic design. The rotor planform evolved into a configuration which produces favorable Reynolds number distributions over the entire vehicle operating envelope, while avoiding the adverse effects of compressibility. Many design innovations were used to specially tailor the rotor airfoil to operate at the extremely difficult combinations of Reynolds number, Mach number, and lift coefficient that are required during the mission. This was a critical step in the overall design process because no known existing airfoils are able to fulfill the above requirements.

Fig. 5.1 shows general trends for disk loading and power loading for existing aircraft, including the hypothetical NASA Planetary Aerial Vehicle (PAV) as detailed in [18]. The lower line shows vehicles on Earth, while the upper line shows trends for these vehicles shifted to Martian conditions. This change comes from the different values of density and gravity on Mars, and combines to decrease the disk loadings and

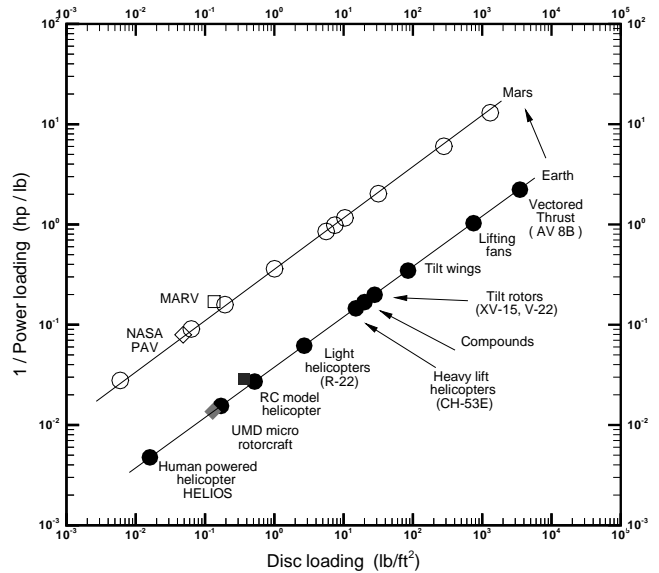


Figure 5.1: Disk loading vs 1 / power loading for powered-lift aircraft on Earth and Mars

increase the power loadings. Any viable new powered-lift aircraft would be expected to follow these trend lines, and it can be seen that the MARV follows this. Thus even though the disk loading and power loading are much different from conventional values on Earth, it can be seen that this combination of these two parameters follows established trends.

## 5.2 Planform design

The rotor design process began with an estimate of the maximum performance that could be expected of airfoils in such a low Reynolds number environment. Very little is known about airfoil behavior below Reynolds numbers of 100,000, and even less about behavior at such Reynolds numbers and high subsonic Mach numbers [19]. It was recognized that while relying on the airfoil sections to work to their extremes, the combination of these two difficult conditions would require conservative initial estimates. Based on the extensive University of Illinois at Urbana-Champaign Low Speed Airfoil Test (UIUC LSAT) data, and performing standard compressibility corrections, it was decided not to exceed a hover tip Mach number of 0.5. This was thought to be the limiting case not because of the absolute value of the Mach number, but because of its close proximity to the estimated critical Mach number at high lift conditions. Rotor blades on Earth operate at higher tip Mach numbers, since these airfoil sections generally have greater margins between the critical Mach number and drag divergence Mach numbers. However, the weak boundary layer at low Reynolds numbers makes it important to avoid shocks and sonic flow altogether, since it is likely that the associated adverse pressure gradients would completely separate the boundary layer and stall the airfoil. Associated with this choice of limit on hover tip Mach number, it was decided that the maximum blade loading in hover should be 0.2.

### 5.2.1 Momentum theory analysis

Having set these two parameters, the next step was to apply a momentum theory analysis to compare the performance of different rotor configurations based only on tip Mach number and a chosen solidity ratio. The actual blade planform was left unspecified, as this momentum theory-based analysis by definition was only concerned with overall dimensions.

For a given solidity and tip Mach number, plots were made of disk loading versus blade loading, power loading and figure of merit. From these plots, the value for maximum blade loading set the maximum disk loading. For a given solidity ratio and tip Mach number, a minimum radius of the rotor was determined. This process was continued for a large range of inputs, and for three rotor configurations representing respectively, a conventional single rotor design, a coaxial design, and a quad-rotor design. Based on this analysis, as detailed in the tradeoffs section the coaxial design was chosen, as it allowed a minimum vehicle size, did not require a tail rotor, and gave a favorable Reynolds number distribution.

At this point, initial rotor configuration and planform selections were made so that a combined blade element/momentum theory analysis could be used to calculate the performance of the helicopter. In order to keep the Reynolds number as high as possible with a fixed tip speed and rotor radius, the chord needed to be as large as possible. Thus two blades per rotor were chosen. This would result in blades of unconventionally low aspect ratio, but it was decided that the Reynolds number concern outweighed the performance degradation resulting from the adverse three-dimensional flow effects due to a low aspect ratio blade. A quick comparison of this planform to a more conventional rotor blade with aspect ratio of 15, for the same radius and blade loading, showed that a coaxial rotor would require 7 blades per rotor, and the tip Reynolds number would be barely 25,000. Clearly, this blade loading could not be maintained at such a low Reynolds number, and most likely the

profile drag of 7 blades would outweigh the reduction in tip losses resulting from a higher aspect ratio.

### 5.2.2 Blade element/momentum analysis

The blade element analysis used an input chord distribution, linear twist rate, and airfoil data, along with a Prandtl tip loss factor, to calculate the collective pitch required to produce the amount of thrust needed. A table lookup scheme was used with a representative low Reynolds number airfoil from the UIUC LSAT database to obtain lift and drag values for each angle of attack. Prandtl-Glauert compressibility corrections were then applied to the lift values, with the drag values being found as those corresponding to the respective compressibility-corrected lift values in the table. The resulting inflow, power, angle-of-attack, lift coefficient, and Reynolds number distributions were then determined. In addition, the total power and figure of merit were calculated.

The aerodynamic modeling of the coaxial rotor followed that suggested by Coleman's survey of coaxial research [20]. This showed that the concept of an equivalent-solidity single rotor is widely used and is also an experimentally-validated method. Various schemes have historically been used, ranging from a simple case of two isolated rotors related by an interference factor, to a 'dual-rotor theory' used by Sikorsky to study the ABC rotor, to sophisticated wake modeling methods for detailed analysis. However, working with the available resources, and citing the conclusions of Coleman, it was decided that an equivalent-solidity single rotor analysis would be appropriate for this design. This concept, in conjunction with the blade element/momentum theory analysis, was validated against actual Kamov coaxial flight test data [21], and results showed in general good agreement. Use of the equivalent solidity single rotor model leads to coefficients of total vehicle quantities referenced to the area of a single rotor. However, where appropriate, values are referenced to each rotor individually, for example for the calculation of disk loading where it is assumed that each rotor carries half of the total vehicle weight.

It was decided that reasonable assumptions about the airfoil behavior would be made in the blade element analysis and then the airfoil would be tailored to take advantage of the planform, but that the actual design of the airfoil would evolve at the same time as the planform and would not be completely known ahead of time. The design of the airfoil would essentially be such that it would meet the lift coefficient / Mach number / Reynolds number combinations along the span of the blade, with the appropriate margins for forward flight. Therefore, using basic airfoil characteristics deduced from preliminary studies, the design process was conducted such that it would produce a blade planform which would have a favorable lift coefficient distribution. Then, when the airfoil design was finalized, any small changes from the assumed airfoil behavior could be compensated for by changing the twist of the blade to produce the desired distribution of lift coefficient.

### 5.2.3 Development of planform

After the selection of the rotor configuration and number of blades, the next step was to develop the planform. A root cutout of 10% radius was chosen as this seemed appropriate based on existing designs. Since the Reynolds number at inboard stations would be very low regardless of the planform, and the tip section might be suffering from tip loss effects, it was decided to try to carry the most lift, and thus generate the highest Reynolds number and lift coefficient, at about 80% radius.

At first, an untapered, untwisted blade with the required radius and chord was analyzed, and based on this, the planform was evolved. Blade element theory shows that normal blade taper is beneficial in reducing induced power, and this, combined with the need to maximize Reynolds numbers at inboard stations, led to the maximum blade chord being at 40 percent radius. From the root cutout to the 40% radius station, the blade was split into three sections with different inverse taper ratios, resulting in an approximately elliptical planform shape in this

region, without creating curved sections that are undesirable from structural and manufacturing standpoints. Inverse taper was used in this region as it was beneficial for blade folding. However, it was still necessary to maintain as large a chord as possible in this region to keep the required lift coefficients below the stall limit. Near the root attachment point, a rapid reduction in chord avoids the need for a drag brace to the trailing edge, which would make blade folding much more difficult. This produces a locally high required lift coefficient that can stall the flow in this section of the blade. However, the stalled region is so small, and the dynamic pressure is so low, that it has a negligible effect on the overall performance of the rotor. Various taper ratios over the central 40-80% radius section were tried until a ratio of 1.2 was settled upon. This gave a Reynolds number of almost 80,000 at 80% radius, while maintaining at least 60,000 along almost 50% of the blade. This was thought to be an adequate operating range for airfoils.

By assuming that compressibility effects are dependent upon the Mach number normal to the airfoil section, and not to that of the blade axis, the use of tip sweep could improve the performance of the blade. Having set the tip Mach number, sweep was incorporated at the tip so that the true tip speed of the rotor could be increased while keeping the incident Mach number at 0.5 in the swept region. This would allow the inboard sections to operate at higher Reynolds numbers than that possible if the true tip Mach number was 0.5. To accomplish this, a parabolic tip sweep was used in the outer 20% of the blade to keep the incident Mach number constant at 0.5 in this region. This resulted in the sweep at the extreme tip being almost 37 degrees.

Taper in the tip region was used for several reasons. First, tapering the tip lowered the thrust-weighted solidity ratio, which lowered the effective chord, resulting in an increase in the effective aspect ratio. Second, the induced power dropped slightly, since tip taper produces a blade which more closely approaches the ideal case of hyperbolic taper. Lastly, since the highest lift coefficient takes place at 80% radius, other sections of the blade which have lower lift coefficients can also have lower Reynolds numbers, and this allows the chord to be decreased in these regions. Therefore in the tip region, where the lift coefficient rapidly drops off, the Reynolds number can be lowered by decreasing the chord.

This tapered, untwisted planform helped minimize induced power, but resulted in a triangular lift coefficient distribution, causing a sharp peak and then a rapid drop off near the tip. Sharp changes in lift necessarily result in shed vorticity, which can produce strong trailing vortices. Even though blade-vortex interactions were not expected to be a major concern for this vehicle, it was thought that any sharp changes in lift coefficient along the blade, and the accompanying shedding of vorticity into the wake, should be avoided. For this reason, linear twist was added until the lift distribution was more even, and this gave the added benefit of reducing the maximum lift coefficient required on the blade, as well as lowering profile power.

A rotor radius of 7 ft was eventually chosen as this was shown to be the minimum possible while still maintaining a reasonable blade loading and aspect ratio, which based on effective chord is slightly greater than 4. For a coaxial configuration, this resulted in a disk loading of 0.135 lb/ft<sup>2</sup> (1.75 kg/m<sup>2</sup>) per rotor, which is almost two orders of magnitude less than a comparable value on Earth. However, assuming the density and thus dynamic pressure on Mars to be almost one one-hundredth of that on Earth at sea level, it appears appropriate that the amount of weight that could be lifted per unit area of rotor disk would be about one one-hundredth of that on Earth.

#### 5.2.4 Comparison to existing planforms

The resulting blade planform has an unconventional appearance, as shown in Fig. 5.2. It seems to resemble a fan blade or a propeller more than a rotor blade. However, the radically different operating environment of this helicopter dictated a very different blade design. For comparison, a simple configuration for a coaxial helicopter

on Earth that could also lift 50kg was analyzed. Starting with an assumed blade loading of 0.1, it was found that for a coaxial, 2-rectangular-blades-per-rotor design, and using a common tip speed and thrust coefficient on Earth, a rotor diameter of 1.06 m and chord of 4.16 cm were required. This made the tip Reynolds number about 600,000, the disk loading 5.8 lb/ft<sup>2</sup> (28 kg/m<sup>2</sup>) per rotor, and the aspect ratio almost 13. These are all realistic numbers on Earth, although the Reynolds number is lower than that encountered on full-scale helicopters but still close to that on model-scale rotors.

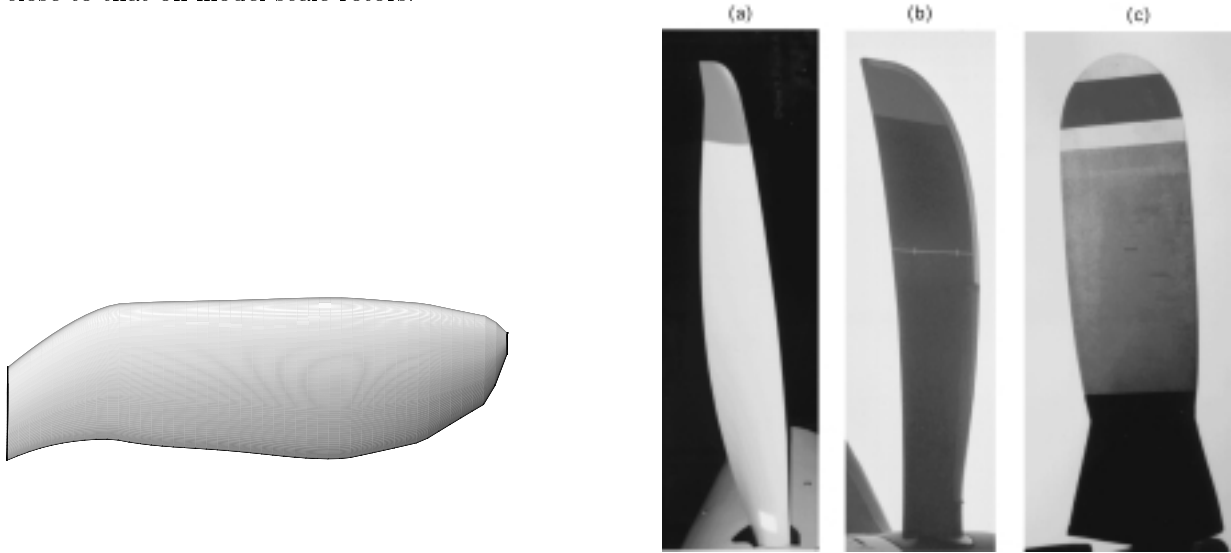


Figure 5.2: Rotor blade planform and propeller blades on existing aircraft

Parameter	On Earth	On Mars
Radius	0.530 m	0.530 m
Chord	4.16 cm	4.16 cm
Aspect ratio	12.7	12.7
Tip speed	213 m/s	213 m/s
Blade loading	0.1	3.4
Thrust coefficient	0.01	0.34
Tip Mach number	0.71	0.93
Tip Reynolds number	607,000	11,000
Mean lift coefficient	0.6	20.4

Table 5.1: 50kg Earth vehicle on Mars

This same design, if used in the Martian atmosphere, will cause many problems, as shown in Table 5.1. The tip Reynolds number now falls to just 11,000 - obviously far below the minimum needed to generate any kind of lifting force while still maintaining practical lift-to-drag ratios. The tip Mach number, based on the lower Martian speed of sound, now becomes 0.93. This is much higher than the operating Mach number of any normal helicopter airfoil, especially one which must be optimized for low Reynolds numbers. The thrust coefficient also increases dramatically to 0.34, almost two orders of magnitude above normal values used on Earth. With the same solidity, the blade loading now becomes 3.4, which indicates a physically unrealizable average lift coefficient of more than 20. These results show why a configuration that easily fulfills the design criteria on Earth becomes infeasible on Mars.

Having seen these conflicting requirements, justifications for this rotor design can be comprehended. The

aspect ratio is very low because rotor diameter needed to be minimized while still attaining as high a blade Reynolds number as possible; the chord is very large inboard in order to improve the Reynolds number in that region; and the tip is swept to keep the incident Mach number less than or equal to 0.5 along the entire blade. Working one section of the blade very hard while minimizing the contribution of the rest of the blade is a risky approach at such low Reynolds numbers, because if the flow is sufficiently disturbed in that region, all the lifting capability of the blade is lost. While recognizing that the low inboard Reynolds numbers limit the corresponding maximum attainable lift coefficients, spreading the distribution of lift coefficient out along a larger portion of the blade ensured that no one section is pushed to its limit. The Reynolds number and Mach number distributions along the blade in hover are shown in Fig. 5.3.

Another justification for the planform design can be seen to the right in Fig. 5.2, which shows 3 types of propeller planforms used on existing aircraft. Comparing the rotor blades of the MARV to propeller blades would seem to be valid, since both have low aspect ratios and high thrust coefficients. The blade on the left is from a Pathfinder UAV (a), the middle is from a Lockheed C-130J (b), and the blade on the right is from a Lockheed P-3 Orion (c). It can be seen that blades with high thrust coefficients generally have lower aspect ratios than normal helicopter blades. Also, the Pathfinder blade operates in a relatively low Reynolds number regime, probably an order of magnitude above that of the MARV. From this blade, it can be seen that the chord has been increased substantially in the midspan region, and that it has an overall taper that is higher than that of other propeller blades. Also, sweep is used in the tip region to delay compressibility effects.

In these respects, it is similar to the blades used on the MARV.

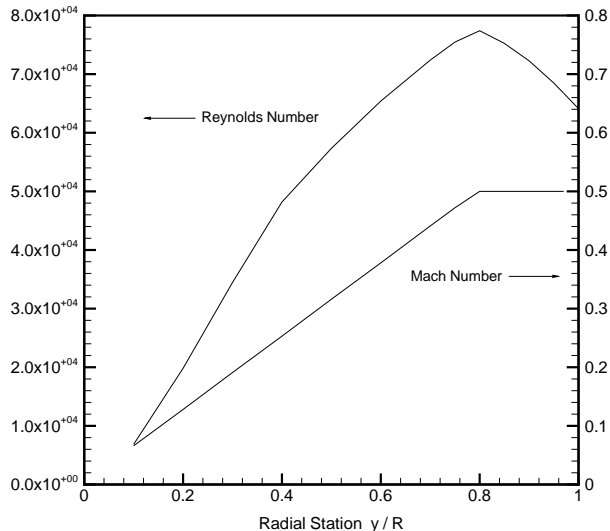


Figure 5.3: Reynolds number and Mach number distribution in hover

## 5.3 Airfoil design

### 5.3.1 Necessity of new design

Concurrent with the design of the rotor planform was the development of an airfoil which could meet the unconventional requirements of high lift at low Reynolds number and high Mach number. The UIUC test data showed that airfoils could indeed be designed to operate at high lift and low Reynolds number. However, all of these tests had been performed at very low Mach numbers, and so the data had to be analyzed for compressibility effects. By choosing a candidate airfoil from the UIUC database, and using the airfoil coordinates and lift data, an inviscid, incompressible panel code was used to estimate the pressure distribution around the airfoil at a higher Mach number.

This analysis showed that all the high-lift, low Reynolds number airfoils had critical Mach numbers at high lift conditions that were too low for this application. Unlike conventional helicopters on Earth, the critical Mach number first appeared in the high-lift retreating blade region in forward flight, as opposed to the low-lift advancing blade region. This is because rotor airfoils are generally not designed for high lift on Earth. Utilizing

a high-lift design leads to the flow on the retreating side accelerating to sonic conditions before the advancing side reaches sonic flow as a result of forward speed. For the Martian mission, a high critical Mach number is important not only to delay compressibility problems, but also because it would determine how fast the vehicle could fly in forward flight. Since the power required drops in forward flight as advance ratio increases, flying fast will minimize the total energy required for the mission.

Conflicting with the need to fly at a high advance ratio is the fact that the strong adverse pressure gradients associated with penetration into sonic flow would most likely separate the boundary layer completely. This would stall the airfoil and also act as an effective drag divergence Mach number, since the drag would radically increase. Thus the margin between the critical Mach number and the 'effective' drag divergence Mach number may be very small. Taking these considerations into account, it was decided that a conservative approach to avoid compressibility problems was to keep the freestream Mach number below the critical Mach number at all times.

At this time, the use of more comprehensive airfoil analysis programs was begun, which could more accurately model viscosity and compressibility effects. From these it was seen that even if an existing low Reynolds number airfoil with a high critical Mach number could be found, the sharp pressure peak behind the leading edge would separate the flow to the point where very little useful lift could actually be generated. Another complication with using existing low Reynolds number airfoils is that these are point designs, which cannot operate over the wide range of lift coefficients and Mach numbers which a rotor airfoil encounters around the azimuth in forward flight.

From these findings, it was determined that no existing airfoil could fulfill all the requirements of the present rotor design. The closest example of an airfoil which might meet the requirements is the Apex 16 as used in NASA high-altitude flight experiments [22]. However, even though the Apex 16 has been designed for high Mach numbers and low Reynolds numbers, the latter are still 2-10 times higher than that encountered by the MARV. Also, the Apex 16 cannot operate over the wide range of lift coefficients needed in the present design. Thus it was decided that the only alternative was to design an airfoil specifically for this application.

### 5.3.2 Design process

Many traditional low Reynolds number airfoils are designed so that the peak suction pressure on the top of the airfoil is relatively low and flat, so that there can be a gradual pressure recovery along the chord. This helps the boundary layer navigate the flow, as it is not subjected to strong adverse pressure gradients. In order to keep the pressure peak to a minimum and still produce high lift, significant camber is used and the airfoil is designed to produce lift over most of the chord. Normally, camber is undesirable for rotor blades due to their inherent torsional flexibility. However, in this application, not only would the dimensional pitching moments be very small because of the low dynamic pressure, but the low aspect ratio of the blade would increase the torsional rigidity.

A complication of combining low Reynolds number with high Mach number is that as Mach number or angle-of-attack increases, the pressure peak at the front of the airfoil increases, and this can lead to sonic flow and flow separation due to the strong adverse pressure gradients and weak boundary layer.

With these design issues and criteria in mind, a highly iterative process was used to design an airfoil using the Xfoil commercial airfoil design program. This code has been validated for low Reynolds number flows as detailed in [23]. The first step in designing the airfoil was based on the desired range of lift coefficient, Reynolds number and Mach number that would be encountered along the length of the blade in hover.

As detailed above, a benefit of operation in the Martian atmosphere is that the use of airfoil camber is not

ruled out as it usually is on Earth. Taking advantage of this, while still trying to keep the airfoil pitching moment as small as possible, camber was used to achieve the high lift coefficients needed. This also allowed the lift distribution to be spread over a larger area of the airfoil, so that the front of the airfoil would not be carrying the vast majority of the lift. This is an extremely important aspect of the airfoil design. Since it was desired to avoid sonic flow altogether in order to prevent the boundary layer from having to attempt to pass through strong adverse pressure gradients, it was critical to keep the suction peak low enough over all operating conditions so that it would not create sonic flow on the airfoil. Distribution of lift over the airfoil, thus minimizing the peak suction pressure behind the leading edge, helped avoid sonic flow at high angles of attack and / or high Mach numbers.

At the Reynolds numbers of interest, the boundary layer separates before it has transitioned to turbulent flow; this makes re-attachment of the boundary layer much less probable, and almost negates the lifting capability of the airfoil [24]. For this reason, boundary layer trips were used on both the upper and lower surfaces, at 40% and 20% chord respectively, to artificially transition the boundary layer to turbulent flow. This prevented the formation of a laminar separation bubble and energized the boundary layer so that it could stay attached along a much longer portion of the chord. In most cases, the analysis showed that the boundary layer stayed attached almost right up to the trailing edge. It was also found that designing the planform to keep the Reynolds number above 50,000 along more than half of the radius was a good strategy. Below 50,000, it became extremely difficult to keep the boundary layer attached to the airfoil surface for more than a small distance along the chord, as turbulent separation would occur almost immediately after the trip transitioned the boundary layer to turbulent flow.

Various methods of lift augmentation were studied, such as trailing-edge flaps, slots, slats, and servo-flaps. However, all were ruled out because of their performance at such low Reynolds numbers, and the possible adverse effects they could have on the overall flow characteristics, was uncertain. The fragile nature of the boundary layer and the difficulty of keeping the flow attached argued against the use of any devices which could disrupt the flow.

### 5.3.3 Forward flight considerations

Using the predictions of inflow based on the blade element analysis, as well as good initial guesses for control settings and flap angles, and having settled on a forward flight advance ratio (described in the performance chapter), it was possible to next determine the variation in lift coefficient needed around the rotor azimuth in forward flight. Comparing the computed operating envelope of the airfoil with the operating envelope of the rotor would then ensure that enough margin remained for gusts and maneuvers. This margin was calculated to correspond to a change in lift coefficient of approximately 0.2, based on an assumed possible gust of 5 m/s.

This analysis then required the airfoil to be slightly modified to ensure that it could operate over the required range of lift coefficient, Reynolds num-

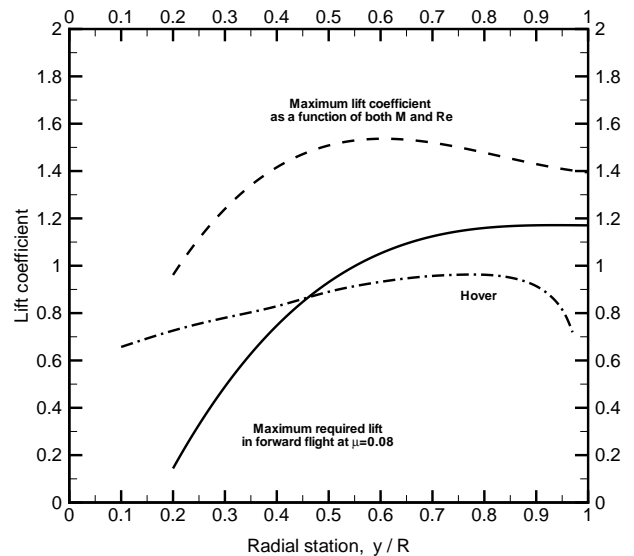


Figure 5.4: Operating envelopes of airfoil and rotor

ber and Mach number. The results of this analysis are shown in Fig. 5.4 and detailed in the performance section, where it is seen that the maximum lift coefficients needed at any point during the mission are well below the airfoil maximum lift coefficients at each combination of Reynolds number and Mach number. However, it must be emphasized that all of the airfoil data is from an airfoil design program and has not been validated experimentally. The airfoil would have to be extensively tested to ensure the accuracy of the calculated data, and some re-design and/or movement of the boundary layer trips may be necessary.

### 5.3.4 Features of the AGRC 1506 airfoil

The newly designed airfoil profile, named the AGRC 1506, is shown in Fig. 5.5. This airfoil has a maximum thickness of 15% chord, and a maximum camber of 6% chord. The boundary layer trips, shown at 40% chord on the upper surface and 20% chord on the lower surface, are also visible. The lift and pitching moment coefficient distributions along the blade in hover are shown in Fig. 5.6, where it can be seen that the maximum lift coefficient is approximately 0.97 and the pitching moment coefficient stays relatively constant at about -0.16. Inboard of the 16% radius station, the blade operates in a stalled condition because the chord decreases quickly and the required lift coefficient increases beyond the stall limit. This rapid reduction in chord avoids the need for a drag brace, which would make blade folding more difficult. However, as mentioned above, the contribution of this section to the overall performance of the rotor is negligible.



Figure 5.5: AGRC 1506 profile

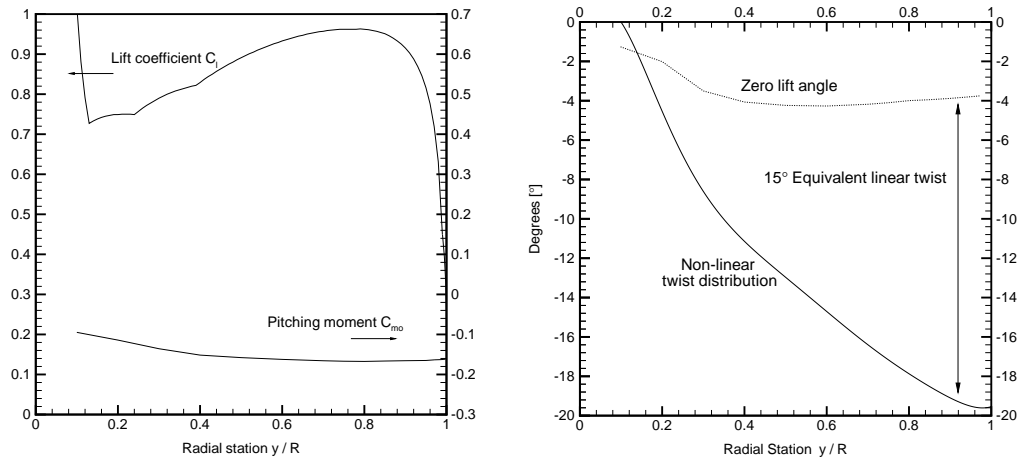


Figure 5.6: Lift and pitching moment coefficients in hover

The final step in the rotor blade design process involved modifying the previously linear twist distribution to a non-linear distribution that would produce the desired lift coefficient distribution. The calculated airfoil data

showed that the zero-lift angles and lift curve slopes varied along the span of the blade, and were different from what had been assumed. This resulted from the unconventional combinations of Reynolds number and Mach number along the length of the blade. This was a planned change, however, and therefore did not require radical changes in the twist distribution. This modified twist distribution is shown to the right in Fig. 5.6.

### 5.3.5 Rotor specifications

The dimensions and parameters of the rotors are shown in Table 5.2.

Number of blades	2 per rotor
Radius	2.13 m (7 ft)
Maximum chord	0.670 m (2.2 ft)
Tip chord	0.366 m (1.2 ft)
Tip speed	143.75 m/s (471.6 ft/s)
Tip Mach number	0.625 (effectively 0.5)
Thrust-weighted solidity (each rotor)	0.1585
Effective chord	0.530 m (1.74 ft)
Thrust coefficient (each rotor)	0.0232
Disk loading (each rotor)	1.75 kg/m <sup>2</sup> (0.135 lb/ft <sup>2</sup> )
Power loading	10.2 kg/kW (6.29 lb/hp)
Blade loading	0.1464
Mean lift coefficient	0.85
Maximum blade Reynolds number	78,000
Tip Reynolds number	64,800
Hover power required	4880 W (6.54 hp)
Forward flight power required ( $\mu=0.08$ )	4620 W (6.19 hp)

Table 5.2: Rotor characteristics

## 6 ROTOR BLADE STRUCTURAL DESIGN

### 6.1 Detailed design of the rotor blade

The rotor blade was designed for the lowest weight possible. Conventional designs usually use multi-layered skin, a single spar structure and a honeycomb core. As the aspect ratio of the planform giving optimum aerodynamic performance is small compared to conventional helicopter blades, a different strategy is adopted to design the rotor blades.

#### 6.1.1 Design methodology

As the lift produced by a single blade is only of the order of 50 N, the stress on the blade skin due to lifting forces is quite low compared to normal helicopter rotor blades. Hence it was decided that Mylar, which is a light plastic material, be used as the major component of the skin structure of the aircraft. Mylar skin was reported to be successful for human powered aircraft designs [25, 26] and is also used presently for an experimental

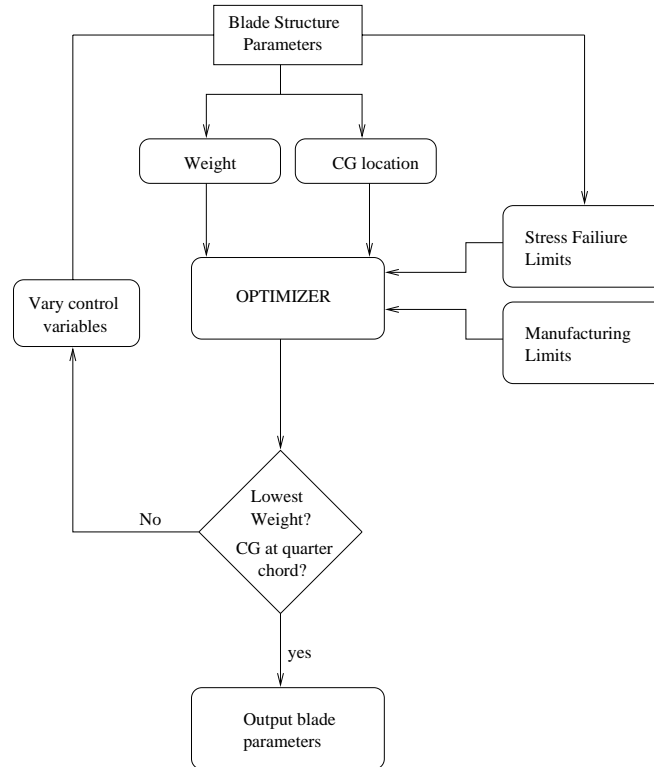


Figure 6.1: Design methodology

human powered helicopter design [27]. Graphite epoxy composite was chosen as the material for the structure supporting the skin, due to its high strength-to-weight ratio. A single hollow spar with rib structures to support the Mylar skin is used as the baseline design. The size and thickness attributes of the spar, rib and trailing edge structure were found using a constrained optimization. The weight of the rotor blade was used as the objective function for optimization. The control variables were the thickness of the spar, thickness of the I-beam type rib structure, and the thickness and extent of the trailing edge structure. To prevent aeroelastic instabilities the center of gravity of the rotor blade was constrained to be coincident to the quarter chord axis location. Limits of manufacturing and stress failure were used on the control variables to produce a realistic design. The design methodology is summarized in the schematic in Fig. 6.1.

### 6.1.2 Final rotor configuration

Fig. 6.2 shows the final rotor configuration. Sections A-A', B-B' and C-C' are shown in Figs. 6.3, 6.4 and 6.5, respectively.

A tubular spar structure made of carbon epoxy having thickness of 0.2 mm is used. The spar structure is supported by a 1.26 mm leading edge piece which also helps in bringing the CG location to the quarter chord. The rear support for the spar is in the form of an I-beam with 0.4 mm thickness, and is located at the quarter chord position. At the rib locations the spar thickness is increased to 0.5 mm, and the leading edge support has a thickness of 2.28 mm. The thickness of the rear I-beam support is also increased to 1 mm. This thickness extends 20 mm in the spanwise direction and provides spanwise torsional and bending moment support for the rotor blade. There are 7 such locations on the blade including the root and the tip. Section B-B' (Fig. 6.4) and Section C-C' (Fig. 6.5) signify the salient features of the spar structure.

The ribs help to preserve the shape of the airfoil and also are used as the supports for the Mylar skin. Mylar

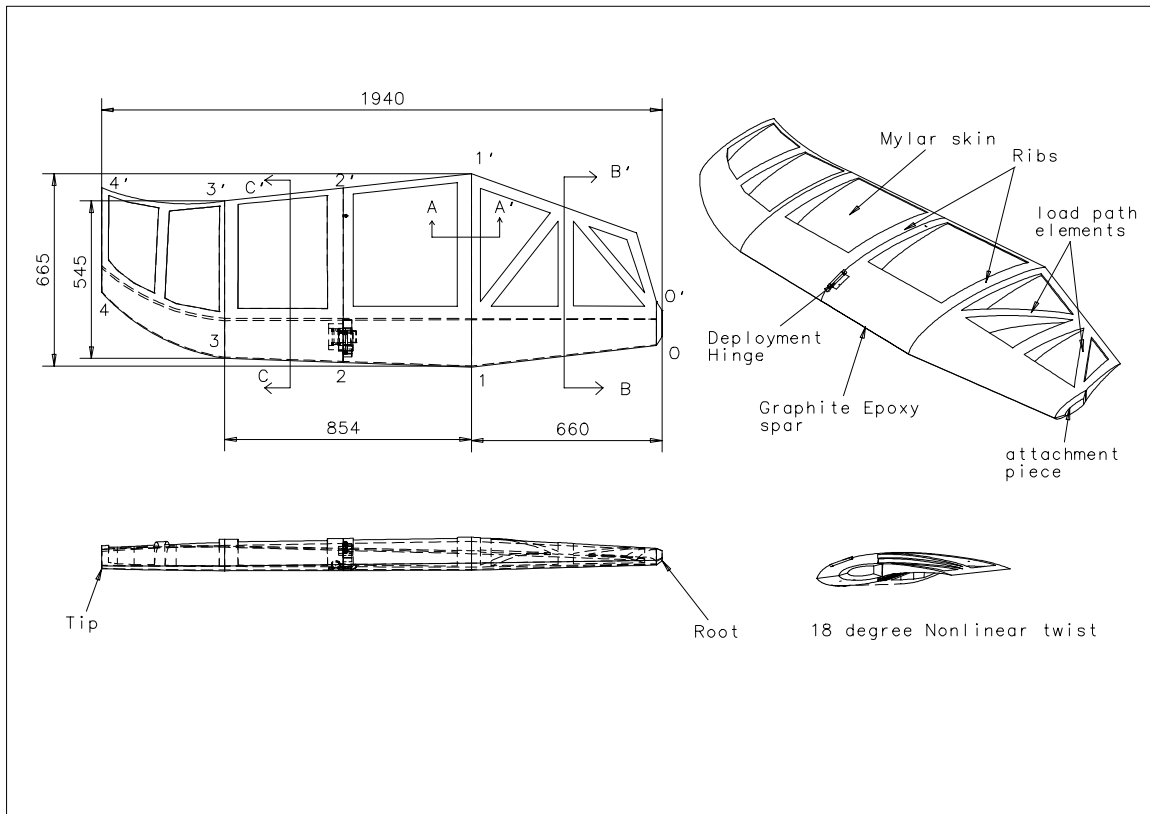


Figure 6.2: Four view drawing of the rotor blade

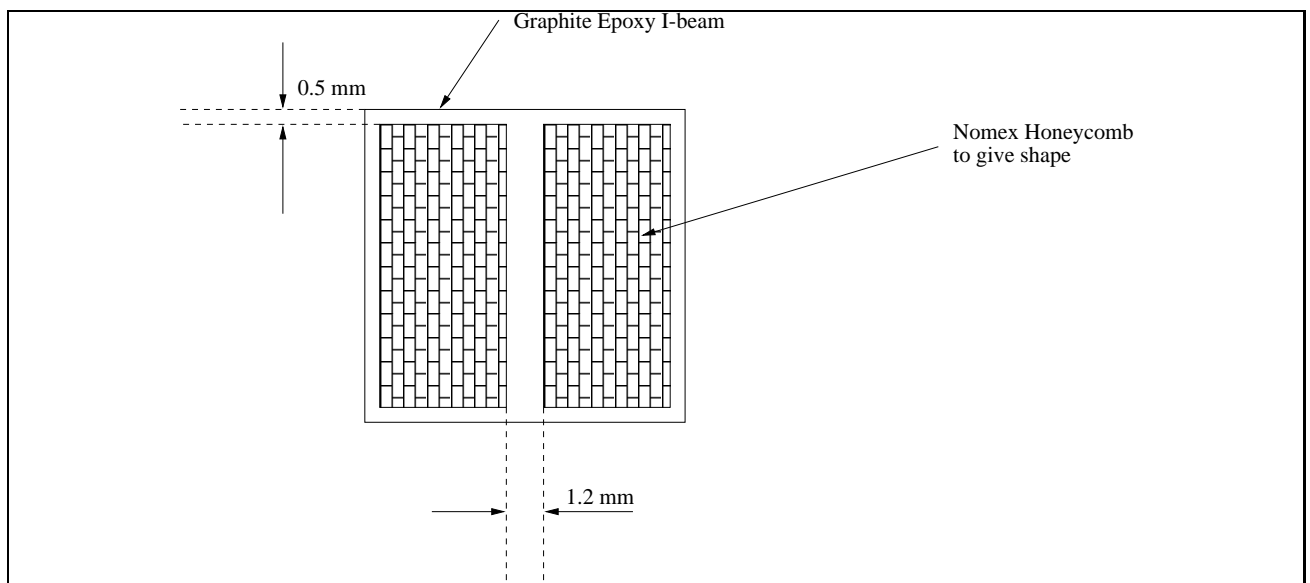


Figure 6.3: Section A-A'

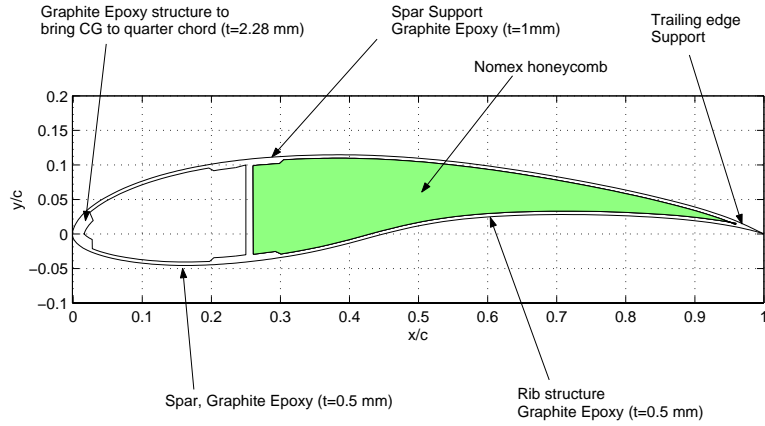


Figure 6.4: Section B-B'

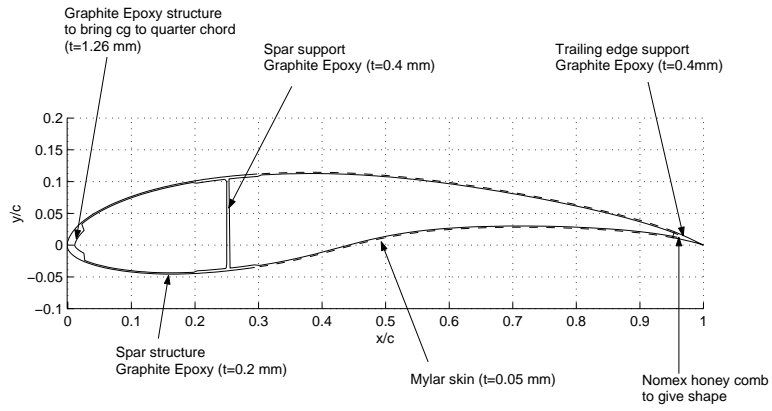


Figure 6.5: Section C-C'

is stressed in the spanwise direction and glued on to the ribs. Section A-A' (Fig. 6.3) shows the typical section of a rib. The bending loads from the lifting forces are supported by the I-beam structure, while the Nomex honeycomb core and side plates help to preserve the shape and support chordwise torsion arising from bending. Since the ribs are considered to be ineffective in supporting the centrifugal force and torsion, these loads are supported by the spar structure alone. There are transverse structures in the inboard section of the rotor blade to transfer the centrifugal loads due to the ribs and trailing edge structures to the blade root. These have the same cross-sectional structure as the ribs.

The extent of the trailing edge structure varies from 96% of chord to 90% of chord along the span of the blade. The structure is made of 0.4 mm graphite epoxy with a Nomex honeycomb core to provide shape. The trailing edge structure is supported at the ribs where they have solid graphite epoxy cross section.

There is a solid blade retention piece at the blade root. The blade is attached to the root deployment hinge which is in turn attached to the hub. The blade is split into inboard and outboard parts to facilitate folding. The hinge and locking mechanism at the mid span and root sections will be described in detail in the deployment section.

### 6.1.3 Weights

The weight of a single blade with its associated deployment mechanisms at root and hinge was analytically estimated. Table 6.1 shows these results.

Structure	Material	Weight
blade structure	graphite epoxy	0.9681 kg
skin	Mylar	0.0255 kg
honeycomb	Nomex type	0.0842 kg
deployment hinge (mid span)	Al-Li alloy	0.0557 kg
deployment hinge (root)	Al-Li alloy	0.3047 kg
torsion springs	stainless steel	0.06157 kg
Total		1.4997 kg

Table 6.1: Weights of blade components

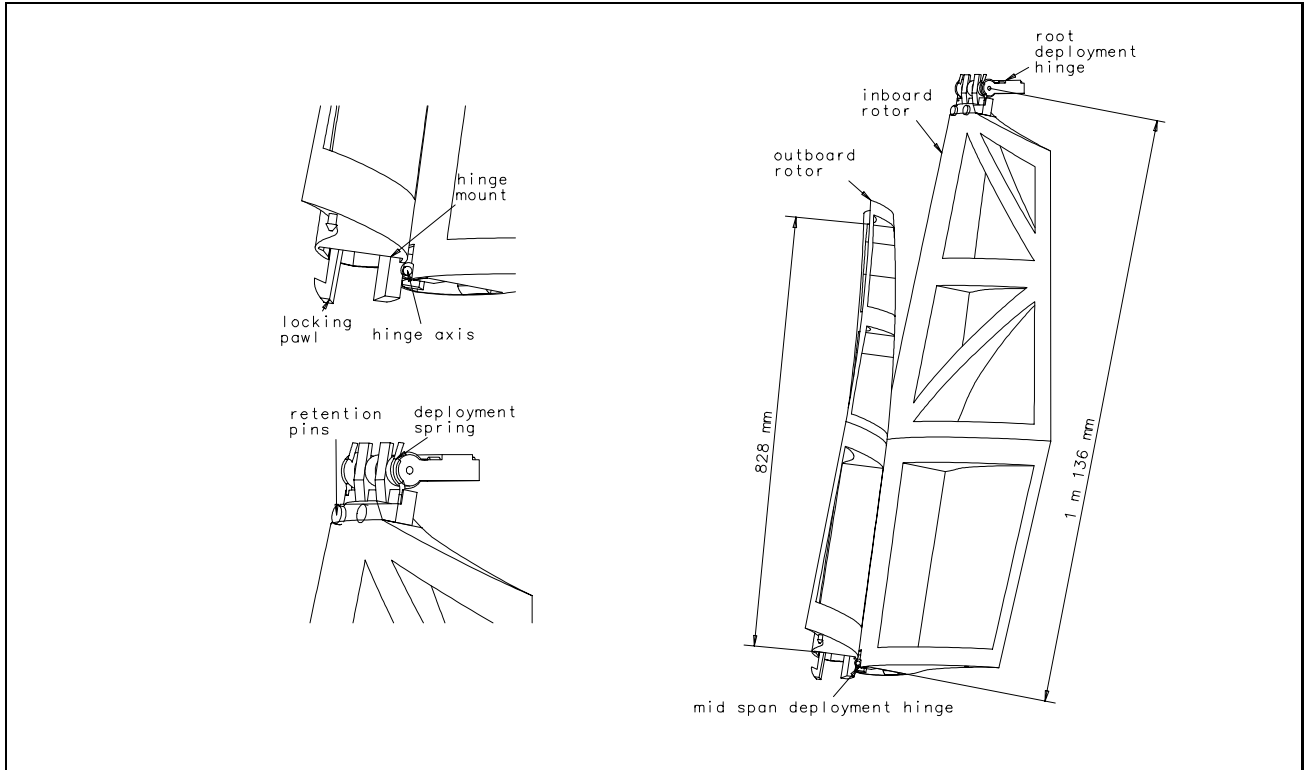


Figure 6.6: Blade in the folded position

## 6.2 Deployment mechanism of the rotor blade

Each rotor blade is folded twice to make the vehicle as compact as possible. A spring loaded self deploying hinge is used at the root of the blade, while the hinge at the mid span location is deployed and locked using the motion of the lander doors. The lander configuration of the Mars Pathfinder used four petal-like door designs which opened radially outward. We recommend the same lander design for this mission. The entire deployment scheme is shown in Fig. 6.9.

### 6.2.1 Deployment hinges

The location of the deployment hinges for the top rotor blade is shown in Fig. 6.6. The details of the root and mid span deployment hinges are shown in Figs. 6.7 and 6.8. The root deployment hinge has positive locking in the lifting load direction. It has projections in the outboard hinge piece which prevent the hinge from turning past the 180-degree position in the counter-clockwise direction as seen in the figure. A locking lever that is actuated

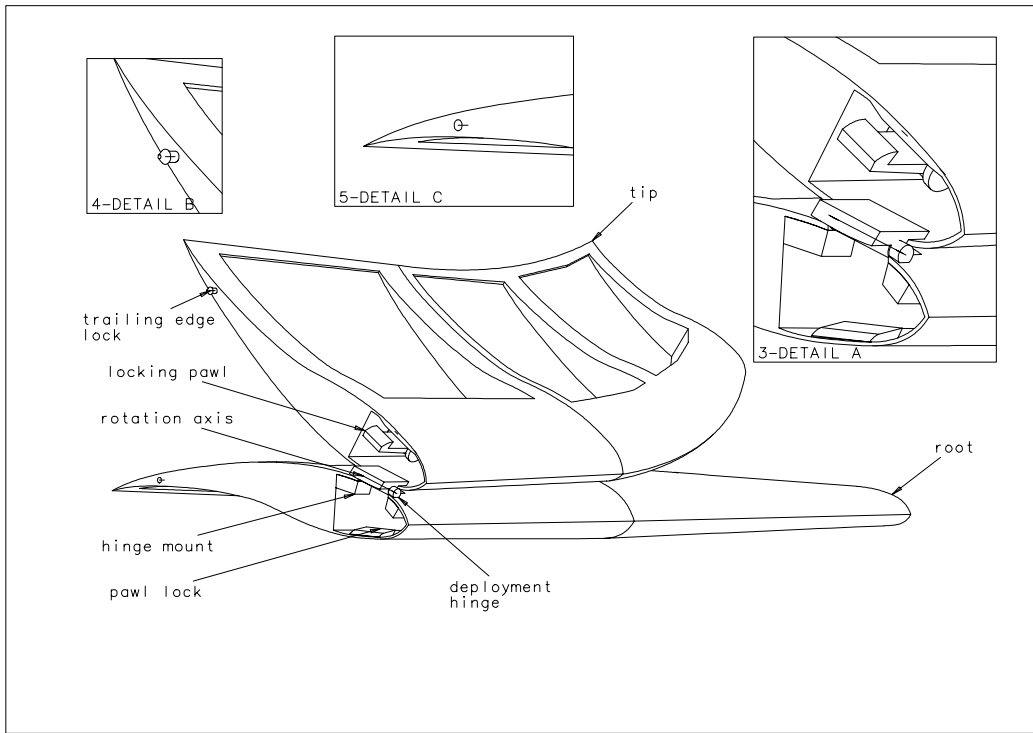


Figure 6.7: Mid span deployment hinge details

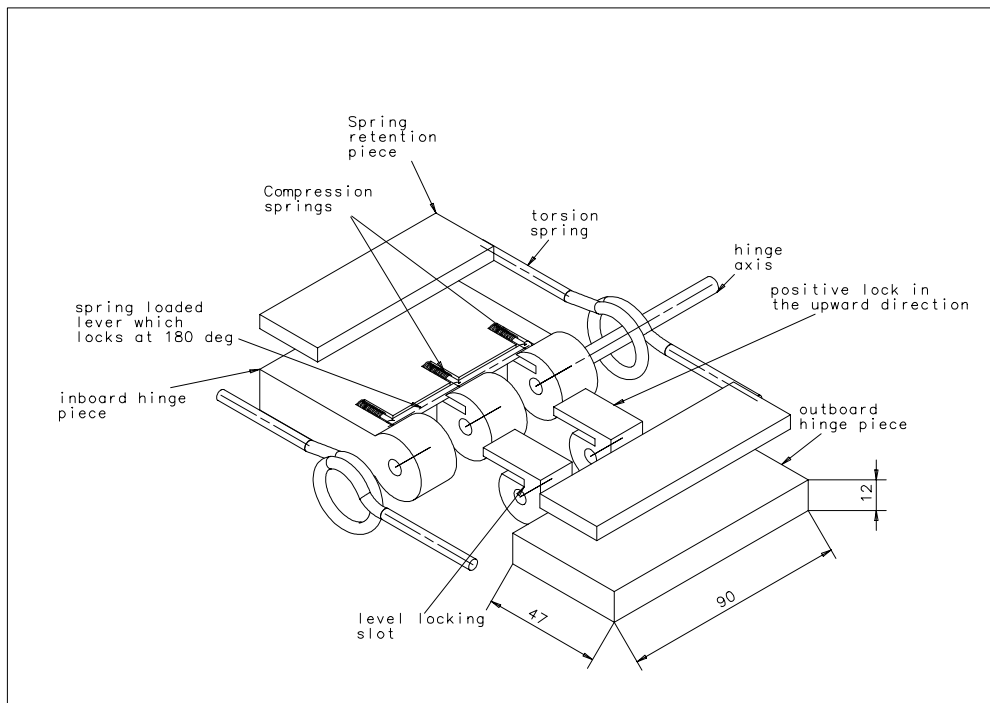


Figure 6.8: Root deployment hinge details

by compression springs is provided in the inboard hinge. This inboard hinge rolls around the outboard hinge rollers during rotation, and pushes into the lever locking slot, locking the clockwise movement at the 180-degree position. As the blades do not have to be folded back, the hinge is permanently locked by these mechanisms once the blades are deployed. Torsion springs provide the necessary torque to rotate the blade to the locking position. The mid span deployment hinge is not self-actuating and is locked into position by a cord connecting the lander door to the tip of the blade.

**Recommendations for actuation mechanisms:** The actuation mechanisms used for releasing the cords at the appropriate times can be electromagnetically actuated clips. The cords themselves can be composed of electrical wires and can provide the connections to the actuators.

## 7 HUB STRUCTURAL DESIGN

The rotor blades of the MARV have been designed to suit the special environment of Mars. Since the Reynolds number is low, the chord is large. The rotor radius is small for sizing considerations inside the lander. As a result, the aspect ratio of the rotor blade is lower than that of a conventional helicopter on Earth. This leads to stiffer blades resulting in high vibratory hub loads. High vibration is detrimental to the health of onboard electronics, imaging instruments and scientific payload. The blade frequencies need to be suitably optimized by a careful hub design. Hence, selection of the type of hub and its detailed design is critical to the overall performance of the avionics, cameras and scientific payload.

### 7.1 Functions of the rotor hub

The rotor hub has the following functions: (i) blade retention and introduction of pitch changes; (ii) determination of the quickness of the rotor response to control inputs. Hence, it influences the maneuverability and agility of a helicopter; (iii) determination of the way in which rotor forces in the rotating frame are transmitted to the fixed frame; and (iv) the rotor transmits the blade forces to the fuselage through the hub. In the tracked condition it transmits only  $pN/\text{rev}$  harmonics to the body, where  $p$  is an integer and  $N$  is the number of blades.

### 7.2 Selection of hub type and layout

#### 7.2.1 Critical issues for Martian helicopter

In selecting a hub type, the following considerations are critical:

- Low vibratory loads on the fuselage. This is required for proper functioning of cameras, onboard electronic instruments, scientific instruments and avionics.
- Mechanical simplicity results from a lower parts count.
- Low weight.
- Reduction or elimination of lubrication.
- Elimination of aeromechanical instabilities.
- Elimination of dampers to save weight and complexity.
- Adequate control power.

Folded rotor diameter: 1520 mm  
 Maximum height from ground: 1338 mm

Reference entry body diameter: 2400 mm  
 Reference entry body maximum height: 2230 mm

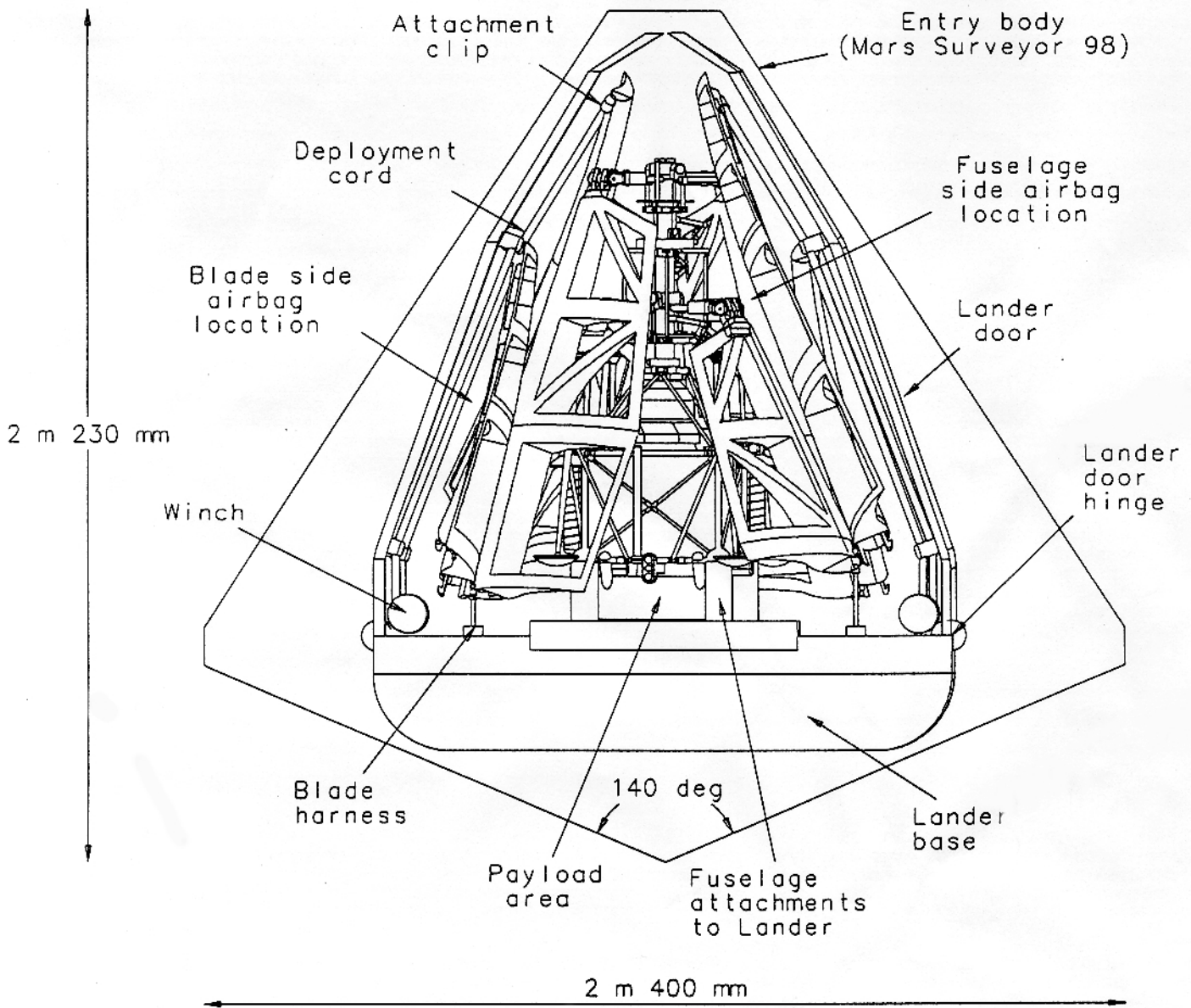


**Figure 6.9: Configuration of MARV stowed inside the lander**

The landing legs are retracted along the fuselage and maintained in position by retention links. The rotors are folded two times: once at the root, once at an appropriate span location for an optimal retraction ratio. The lander consists of a base containing payload, power supply and a communication system, and four hinged petals of dissimilar size. The two wider petals help in deploying the blades. They are equipped with winch operated cords with actuated attachment clips to the blade advancing tip. The deployment sequence from the lander is shown in detail in figure 6.10. The blades are protected by airbags on both fuselage and lander sides. The major dimensions of Mars surveyor 98 are shown for reference.

There are certain advantages for our specific application which have been exploited to fulfill the above considerations. They are:

- Aerodynamic loading is low because of the low density.
- High fatigue life of the blades is not an important requirement.
- Reduction of operating costs and maintenance are not crucial issues.
- High maneuverability and agility are not required.

The selection of the hub is influenced by the number of blades, mechanism of control and vibration level. We have two blades per rotor, and therefore we use a conventional control mechanism. The choice of the number of blades and mechanism of control is justified in the trade study section.

If the blades are not allowed to flap, lag or elastically twist then the entire periodic aerodynamic loading will be transmitted to the helicopter through the hub. Three hub designs representing teetering, articulated and hingeless rotors were examined.

- Hingeless rotors have a low parts count and are simple. Our blades are relatively stiff. Hence, elastic motions depend on a flexible hub design. The lowest flap frequency for our rotor is 1.15/rev with a flexible hub without incorporating a mechanical hinge. At this flap frequency vibratory hub moments are high.
- Articulated rotors need two flap hinges at the root. They add to the mechanical complexity of the system. Also, lag hinges are required to reduce chordwise bending moments. As a result these rotors are normally soft inplane, leading to ground resonance problems. Lag dampers are required.
- In the case of a teetering hub, the rotor flaps about a teetering hinge. Hence the problem of transmitting vibratory flapping moments at the hub is eliminated, but the responsiveness is reduced. However, agility is not a key requirement. Two blades are rigidly connected so that only one flap hinge at the hub is needed. It is mechanically simple with a low parts count. It is generally stiff inplane, and therefore ground and air resonance problems are eliminated [28]. Lag dampers are not required. A relatively flexible pylon can be incorporated in case of high chordwise bending moments during maneuvers.

A 2-bladed teetering hub is simple, reliable, light weight and free from instabilities. It is mechanically simple with less parts count. It is stiff inplane, and hence free from aeromechanical instabilities. High inplane stiffness is acceptable in view of the low aerodynamic loading and less stringent fatigue requirement. Flap vibratory moments are low because it teeters freely. This gives less agility but such a trade off is acceptable. Hence a teetering hub is the best choice.

### 7.3 Detailed design

Each rotor of the coaxial system has a teetering hub. Fig. 7.3 shows the details of the hub. The control linkages have not been shown. There are no mechanical flap or lead-lag hinges for each blade. The hinge of the top rotor passes through the shaft. The hinge of the bottom rotor cannot pass through since there are two counter-rotating shafts at that station. This hinge is fixed only to the outer shaft.

A simple door hinge is used in each hub to accommodate both collective and cyclic pitch changes. It reduces drag in forward flight because of the thin cross section. The blades are fixed to the hub with two bolts. The hub extends to 6% of the rotor radius. The blade folding mechanism is between 6% and 10% of the rotor radius.

The pitch axis passes through the center line of the hub and the 25% chord line of the blade. The latter is also designed to be the elastic axis of the blade. This decouples bending motion from torsion so that the entire actuation energy goes into pitch change.

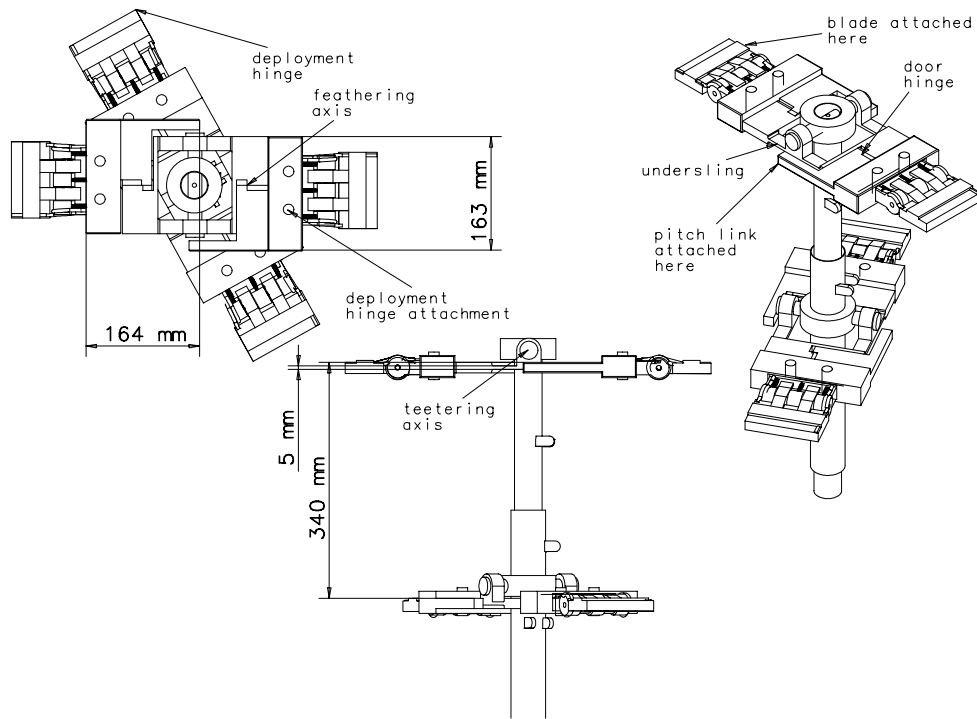


Figure 7.3: Hub design

An undersling is provided to reduce Coriolis forces induced at the hub due to the teetering motion. The undersling is designed so that the center of gravity of the rotor in flight passes through the teeter hinge. The blade coning angle during forward flight at advance ratio  $\mu = 0.08$  is  $0.39^\circ$ . The blade coning angle during hover is  $0.41^\circ$ . The coning angle is small because of the low Lock number, 0.354. The undersling is designed corresponding to a coning angle of  $0.40^\circ$ . The calculated undersling distance is 8mm.

The hub dimensions are designed with adequate margin of safety for the loadings in steady level trimmed flight at  $\mu = 0.08$ . The aerodynamic loading is very low, and the centrifugal loading is low because of the lightweight blade structure.

The inner part of the hub is made of unidirectional E-glass epoxy. This part acts as a flexible pylon to reduce  $2/\text{rev}$  loadings in the lag direction. It is carved out in the center to adjust the stiffness and hence the blade frequencies. The fiber direction is along the blade span. The outer part, to which the pitch changes are provided, is made of Boron Epoxy. This provides high torsional stiffness for effective pitch control. The hub dimensions are designed to (i) leave adequate margins over steady state loadings and (ii) control the elastic lag and torsion frequencies to reduce vibratory loading. There is no kinematic pitch flap or pitch lag coupling in the rotor system.

# 8 BLADE DYNAMICS AND KINEMATICS

## 8.1 Dynamics and stability

The study of blade dynamics is critical to the design of a rotor system. Coupled blade frequencies should be carefully placed so that they are not close to any rotor harmonics. This helps to keep vibration levels low.

The dynamic analysis of the rotor blades is performed using the University of Maryland Advanced Rotorcraft Code (UMARC). A teetering rotor displays articulated rotor characteristics for odd harmonics of flapping motion and hingeless rotor characteristics for even harmonics of flapping motion [28]. The lag and torsion motions follow the characteristics of a hingeless rotor. The non-dimensional stiffness and

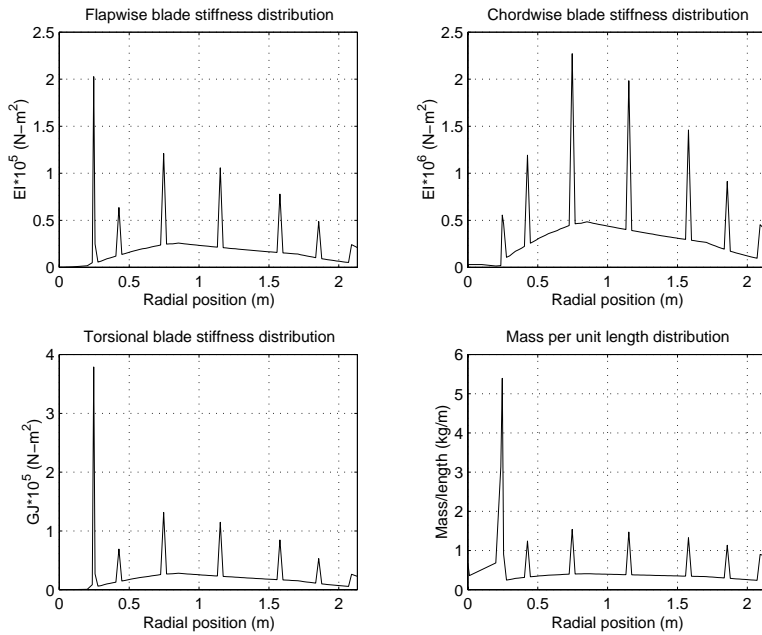


Figure 8.1: Stiffness and inertia distributions on the rotor blade

The non-dimensional stiffness and inertia distributions of the rotor blades are shown in Fig. 8.1. These were fixed after several design iterations to obtain the desired blade frequencies with necessary strength.

The rotor 'fan' plot is shown in Fig. 8.2. The natural frequencies of the blade are given in Table 8.1. The frequencies are placed carefully so that they are not near any forcing harmonic. The teeter flap frequency is 1.00/rev. The first elastic flap frequency is 1.15/rev. The inplane lag freq is high, 3.6/rev. The inplane lag frequency is a key parameter for aeromechanical instabilities like ground and air resonance. Since the rotor is stiff inplane there is no possibility of ground or air resonance. Such a lag frequency can generate high inplane vibratory loads. However, the aerodynamic loading on Mars is very low, due to the low Lock number. Also, the forward flight speed is low. The steady aerodynamic drag force at the hub in forward flight is calculated to be 9.6N. This lag frequency is acceptable for unmanned missions so long as the avionics and imaging instruments are properly isolated from vibratory loads. In the fuselage design chapter we discuss this issue and describe our vibration isolation scheme.

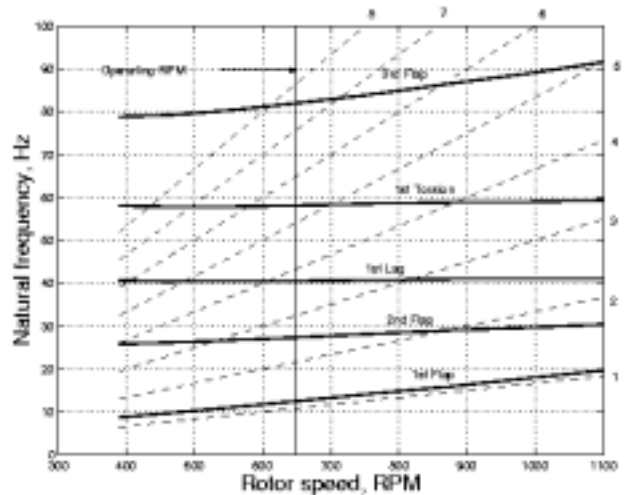


Figure 8.2: Fan diagram of the rotor blades

Natural frequency(/rev)	Cruise
1st Flap frequency	1.15
1st Lag frequency	3.6 (stiff-in-plane)
1st Torsion frequency	5.3
2nd Flap frequency	2.5
3rd Flap frequency	7.5

Table 8.1: Natural frequencies of the rotor blades

It has been verified that there is no flap-lag instability. This is because of the low Lock number (0.354) and high drag ( $C_{do} = 0.028$ ). Pitch-flap instability is eliminated by carefully making the structural design such that the center of gravity of each section is coincident with the quarter-chord line.

## 8.2 Kinematics and clearances

For a coaxial rotor system, kinematics and inter-rotor clearances are important issues, especially on Mars, where gust speeds can range from  $2 - 7m/s$ .

During rotation, the blades pass over each other at  $\psi = 90^\circ$  and  $180^\circ$ . The clearance between the two blades is determined by lateral flapping angle  $\beta_{1C}$ , in the rotating frame. For MARV, (i) the center of gravity offset of the fuselage along the longitudinal direction is zero and (ii) the forward flight speed is low. As a result the lateral flapping angle is small. Table 8.2 gives the variation of the lateral flapping angle due to gust using quasi-steady assumptions.

Gust speed (ft/s)	$\beta_{1C}$ (degree)
5	0.54
10	0.61
20	0.72
50	1.02
100	1.50

Table 8.2: Lateral flapping response to gust

Our inter-rotor clearance is set at  $0.08 D$ , where  $D$  is the rotor diameter. This gives a maximum allowable lateral flapping angle of  $4.6^\circ$ , which is much higher than the maximum lateral angle as calculate above. As a comparison Kamov coaxial systems use a clearance of  $0.095 D$ .

## 8.3 Vibration issues

### Vibration g-level

The g level for vertical vibratory hub shear is calculated for MARV. To determine g level the maximum vibratory hub shear force is divided by the vehicle mass. Then, this value is divided by the acceleration due to gravity on Earth,  $g$ . For a two bladed rotor the predominant hub forcing is at  $2/\text{rev}$ .

For a coaxial system the resultant g level transmitted to the hub depends on the inter-rotor phasing. We define inter-rotor phasing as the angle between the two rotors when one of them is aligned along  $\psi = 90^\circ$  and

$\psi = 270^\circ$ . This phasing is decided by a trade off between vibration reduction and the crucial blade folding consideration. Fig. 8.3 shows the variation of vertical vibration level with rotor phasing. The g-level for MARV is already very low. Hence the rotor phasing is done to make blade folding as compact as possible. The phasing angle is chosen as  $29^\circ$ . This gives a g-level of 0.0129. For a phasing angle of  $90^\circ$  g-level is zero. This is because no wake modeling was done, a simple linear inflow model was used. Hence no 4/rev level is captured.

### Vibration reduction

Due to the sensitive nature of the electronic instruments and imaging cameras that are carried with the helicopter, vibration levels must be kept low. The following passive design features are used to reduce vibration:

- The gear box is shielded from the fuselage through an innovative vibration isolator design. This is described in the fuselage design section. This absorbs vibration both in the flap and lag directions.
- Choice of the rotor system. The teetering rotor flaps freely at a frequency of 1/rev, reducing vibratory hub moments in the flapping direction.
- Vibratory hub moments in the lag direction are reduced by using a flexible pylon made of Kevlar 49.
- An undersling is designed to reduce Coriolis forces induced in the lag direction by the teetering motion. This reduces Coriolis components of the hub loads.
- The fuselage center of gravity is placed below the hub by suitably arranging the placement of the fuel cell subsystems, gears and the pitch actuators.
- Retreating blade stall leads to large torsional impulsive loads. However, at the chosen advance ratio of 0.08, this region is small enough to have a negligible contribution to these loads.
- The advancing blade tip Mach number is limited to 0.56. This minimizes unsteady loads resulting from compressibility effects.

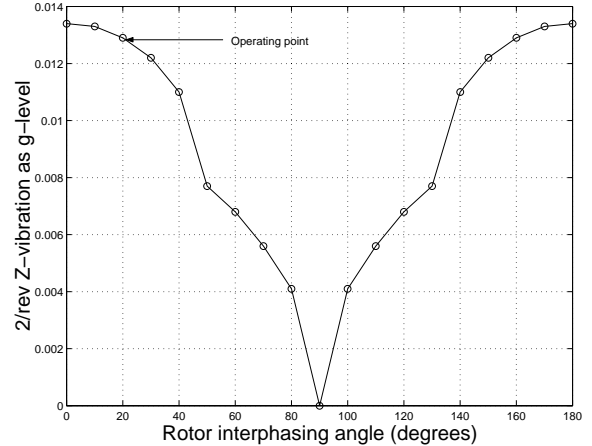


Figure 8.3: Vertical 2/rev vibration measured in Earth g-level

We recommend passive vibration reduction schemes as far as possible, for a low speed Martian helicopter. This is because state of the art active blade control features incorporate individual blade control schemes like active twist, plain flap, servo-flap or moving tips. In a low Reynolds number environment, the flow around an airfoil is very sensitive to any kind of disturbances. Also, the boundary layer is thick. A simple flap may not have any effect on the flow. A servo-flap or moving tip might destroy the flow on the airfoil surface.

# 9 SELECTION OF POWERPLANT

The availability of a suitable powerplant is an important factor which decides the mission, payload and configuration. No systematic study is available in the published literature examining the various propulsion systems for Martian applications.

We have analyzed and compared 10 different energy options. Weight estimates are calculated for each energy option and associated propulsion scheme, wherever possible and meaningful. As a result of this systematic study we have established that, with current technology, a fuel cell based propulsion system will be the most suitable form of propulsion for a Martian helicopter.

## 9.1 Key questions for Martian propulsion

In view of the increasing lift-off costs for space and planetary missions, key questions arise regarding the propulsion scheme of a helicopter operating on Mars. They are as follows:

- 1) Do we need to carry the entire energy reserve to Mars or can we generate the energy fully or partly on Mars?
- 2) Will in-situ generation of mission energy, if possible, reduce the weight that needs to be transported from Earth?
- 3) Will renewable energy sources provide benefits in terms of multiple mission capability?
- 4) Is it possible to have an in-situ propellant production system that will supply propellants autonomously?
- 5) Can energy be produced when the helicopter is flying, without having to carry the entire mission energy stored on board?
- 6) Can clean, environment friendly energy resources be utilized?

These questions are answered at the end of the section.

## 9.2 Analysis and selection of energy options

Energy sources can be classified as primary and secondary sources. Primary sources of energy use direct combustible fuel. Conventional combustion on Mars is not feasible due to lack of sufficient oxygen in the atmosphere and the low atmospheric density. Secondary energy sources will be in the form of electrical power.

To analyze each power source and to finally select the most feasible option, the following methodology is used. The Mars mission requires an energy of 3000 Wh and a hover power of 6 kW. With a rotor of 10 ft radius, the torque requirement is 127 Nm. These values are obtained from preliminary momentum theory analysis. The system weight of each propulsion scheme is determined to fulfill the energy and power requirements of such a mission. Calculations are performed for currently achieved technology levels as well as taking note of their growth potentials.

We analyze the following 10 energy options.

- Hydrazine fueled piston type engine (HP)
- Hydrazine powered tip jet propulsion (HTJ)
- $CO_2$ -breathing propulsion engine (CB)
- Liquid oxygen-liquid hydrogen powered tip jets (LHLO)
- Electrical rockets as tip jets (ER)
- Electrical power derived from batteries (B)

- Electric power from solar cells (SC)
- Electrical power from wind energy (W)
- Nuclear power (N)
- Fuel cells (F)

The energy options and associated propulsion schemes are analyzed based in the following considerations: (1) Use of a currently feasible technology; (2) minimum propulsion system weight for a given mission; (3) simplicity of operation; (4) utilization of in-situ energy resources to reduce take off weight from Earth; (5) utilization of renewable energy sources to facilitate multiple mission capability; (6) future growth potential of technology; and (7) utilization of clean, environment friendly energy sources.

**Hydrazine fueled piston type engine:** The highest value of Specific Fuel Consumption (SFC) that can be obtained with the current state of implementation of this engine is 0.99 kg/MJ. The engine weight is 13 kg [1]. We would need 10.7 kg of fuel. Added to this would be an engine weight of around 10 kg. A reduced engine weight is considered due to lesser power requirement. This gives a total propulsion system weight of at least 20.7 kg. The entire propulsion system and fuel needs to be carried to Mars and once the fuel is exhausted no further mission can be performed. The highest value of SFC that can be theoretically obtained from hydrazine is 0.67 kg/MJ [1]. This will bring down the fuel weight by 32% to 7.24 kg and lead to a system weight of 17.24 kg.

**Hydrazine powered tip jet propulsion:** To estimate the sizes, a specific impulse of 300s is taken as a reference [1]. The rate of change of momentum of the jet at the tip of all the blades combined is 42.3 N. Total mass flow rate is 0.0144 kg/s. This requires 26.5 kg of fuel for a 30 minute flight. Added to this is the weight of jet engines at the blade tips. This can be assumed to be 10 kg. System weight is at least 36.5 kg. The specific impulse assumed is achievable only with a very high adiabatic combustion temperature (3410 K) and combustion chamber pressure (1000 psi, 6.89 MPa) [31]. Engines with such values will be heavy. Chemical energy is inextricably linked to mass. There is a hard upper limit to the specific impulse. If oxidizers like  $N_2O_4$  are used with hydrazine, specific impulse of 500s may be achieved [1]. This would give a fuel mass of 16.5 kg.

**Concept of  $CO_2$ -breathing propulsion engine:** Recently, the feasibility of a  $CO_2$ -breathing engine using metal fuels has been assessed in Japan [32]. It was experimentally confirmed that aluminium and magnesium could burn in the presence of  $CO_2$ . With the results of their work they concluded that it is possible to develop a metal fueled  $CO_2$ -breathing turbojet engine. This may be an attractive scheme for planetary propulsion in the future but currently it is in its infancy. Much more work needs to be done to establish the possibility and reliability of such a scheme.

**Liquid oxygen-liquid hydrogen powered tip jets:** The Apollo J-2 rockets and currently the space shuttle main engines have specific impulses of 426s and 428s respectively [31]. Based on these values, 18.3 kg of propellant would be required to carry out this mission. In each case a total engine weight of 10 kg may be assumed at the very least. However, the weights of tanks and engines would be very high.

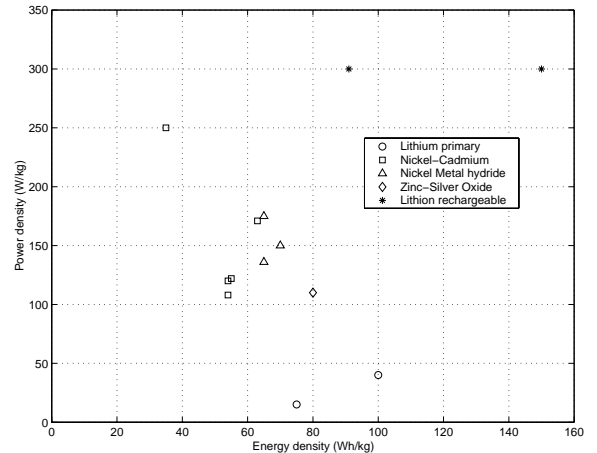


Figure 9.1: Current battery technology

**Electrical rockets as tip jets:** The attractiveness of electrical propulsion is that there is no hard upper limit on the specific impulse. However, the propellant itself is not the source of energy. Electrical energy must be supplied to the propellant from another source. Also, the rate of conversion of this electrical energy to propellant kinetic energy is limited by the mass of the conversion equipment necessary. This is very high. An electrical rocket will be essentially power limited [31].

**Electrical power derived from batteries:** The rated energy density (Wh/kg) and the rated power density (W/kg) are two critical factors in assessing batteries for our application. Rated energy density indicates the total energy a cell can deliver and depends on the rate of discharge of the cell. As the rate of discharge increases from the rated value, the energy density falls. The rate of discharge depends on the power drawn from the cell. Thus both energy density and power density of the constituent cells are important when choosing a particular battery system. The type of batteries that are needed for powering a Martian helicopter fall in the category of vehicle traction batteries, that is, those with high energy density and high power density. Fig. 9.1 summarizes the state of the art in batteries with respect to energy density and power density values [33] [2].

**Lithium primary cells** are the state of the art in non-rechargeable batteries. The Pathfinder Rover used lithium thionyl chloride primary cells to handle peak loads and as backup. A lithium thionyl chloride cells are characterized by energy densities of up to 250 Wh/kg. The energy density can be further enhanced to over 500 Wh/kg (1000 Wh/kg) by the use of halogen additives [33]. Soluble cathode systems like lithium-sulfur dioxide cells are characterized by energy densities of up to 300 Wh/kg [33]. They have favourable low temperature characteristics. However, power density is extremely limited mainly because of the relatively poor conductivity of the electrolytes. They are suitable only for low power microelectronic applications. They cannot be used for applications of or similar to vehicle traction.

High performance 6V **nickel-cadmium rechargeable cell** modules are being developed to provide power sources for electric cars. One such example is SAFT in France, who are developing power sources for the Peugeot and Renault electric cars [33]. Energy density is around 63 Wh/kg and power density 171 W/kg [33].

The highest practically obtained energy density value that has been quoted for **metal hydride-nickel oxide secondary cells** is 67 Wh/kg, by Ovonic Battery Co. [33]. Metal hydride-nickel oxide cells promise to deliver energy densities of around 80 Wh/kg in the near future [33].

The practically realized values of energy density of **zinc-silver oxide aqueous secondary cells** are in the range 40-110 Wh/kg [33]. This is assuming the most favourable discharge characteristics.

The most promising of the batteries considered for purposes of electric vehicle traction are **lithium ion rechargeable cells** using an immobilized or polymer based electrolyte. A lithium ion battery currently made available by SAFT of France has an energy density of 150 Wh/kg and power density of 300 W/kg [2]. At an energy density of 150 Wh/kg and power density of 300 W/kg, the battery mass is 20 kg. The area power density value is 250 Wh/dm<sup>3</sup>. For our application it will take 12 dm<sup>3</sup> of space. Hence, The forecast values for lithium ion vehicle traction batteries for the year 2006 are energy densities near 200-220 Wh/kg and volumetric energy densities of around 400 Wh/kg [33]. With an energy density value of 220 Wh/kg, 13.6 kg of battery would be required.

**Electric power from solar cells:** There are two figures of merit that are used to measure the performance of a space solar array, as well as the entire power system: power per unit mass in W/kg and power per unit area in W/m<sup>2</sup>. These are referred to as specific power and area power density.

Current state of the art Si cells on rigid panels used in space have values of 30-40 W/kg and 90-110 W/m<sup>2</sup>. Advanced flexible lightweight solar arrays can take these values up to 130 W/kg and 90-110 W/m<sup>2</sup> [34]. Even if

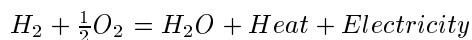
these values were applicable to Mars, 46 kg of solar cells and 55  $m^2$  of solar cell area would be required to generate the total power requirement during flight. The above figures are based on solar intensity in space. Solar intensity on Mars is very low, 590  $W/m^2$  [35]. Atmospheric dust, dust hazes, ground fogs, carbon dioxide and water ice clouds obscure this intensity further [36]. Atmospheric dust reduces transmission of light, harmful to PV arrays. They decrease surface radiation of heat, harmful to heat rejector radiators [36]. Low temperatures between  $0^\circ C$  and  $-100^\circ C$  affect material properties and solar cell performance [36]. The dry, low pressure atmosphere of Mars is also conducive to electrostatic charging [36]. On the other hand, using the available sunlight on Mars removes the need to carry fuel to increase the active life of storage batteries, which can be recharged by the solar cell array. The Mars Pathfinder rover had values of 5 W/kg and 45  $W/m^2$  with GaAs/Ge cells. These are very low for cells which are to be used to harness solar energy in flight [37]. Reference [36] gives the user end power per unit mass value at 7 W/kg even for a hypothetical extensive power generation system for supporting human Mars missions. (This value is obtained by dividing the user end load by the total electric power system mass). However, the Pathfinder lander cells were designed to generate energy at the rate of 3888 kJ/day which is 1080 Wh/day [43]. At this rate the mission energy of 3000 Wh can be collected in a little over 3 days.

For missions on Mars, Silicon (Si), Gallium Arsenide/Germanium (GaAs/Ge) and thin film cell arrays are promising. GaAs/Ge cells are most cost effective where radiation damage is significant. They were used by the Pathfinder Rover. GaAs/Ge cells have the optimum band gap for high efficiency. Indium Phosphide (InP) solar cells also have band gaps near the optimum value for high efficiency. InP cells degrade much slower than GaAs or Si cells when exposed to high radiation [34].

**Electrical power from wind energy:** Wind energy has been envisioned as being capable of providing power at the rate of up to 55 W/kg [43]. However, the technology which envisions this also requires a helium filled balloon of 80 m diameter flying at an altitude of 8 km with a tether cable tying it to the Martian surface. The balloon also has 13m diameter propeller blades running under it [38].

**Nuclear power:** Viking 1 and 2 had radioisotope thermal generator (RTG) units containing plutonium 238. Each generator had a mass of 13.6 kg and provided continuous power at 30 W. Such power to weight ratios are unsuitable for our application. Apart from this, electrical power generation envisioned on Mars from nuclear fuel is in terms of massive installations for future manned Mars missions. These, accounting for only the masses of reactor, shield and power conversion equipment are capable of 77-79 W/kg [39].

**Fuel Cells:** Fuel cells are electrochemical devices that convert the chemical energy of a reaction directly into electrical energy. Fuel cells have the capability of producing electrical energy for as long as they are continuously supplied with reactants. In simple terms, a fuel cell produces electricity, water and heat from a fuel and an oxidant, with two oppositely charged electrodes. The basic chemical equation that applies to this reaction is:



Fuel cell systems can have energy density values higher than 300 Wh/kg [40]. With a value of 300 Wh/kg, only 10 kg of fuel cell system will be required. According to AeroEnvironment Inc., fuel cell systems would readily store 400 Wh/kg, and they are targeting a value of 600 Wh/kg for powering the long endurance aircraft "Helios". This will half the system mass to 5 kg.

Fuel cells may be classified by the type of electrolyte they use. A brief description of various types is given along with their important aspects of operation in the context of Martian applications.

**Polymer Electrolyte Fuel Cell or Proton Exchange Membrane Fuel Cell (PEM):** The electrolyte is a hydrated ion exchange membrane that is an excellent proton conductor. Operating temperatures are around

80°C and below 120°C. Test results show that this cell can operate at very high power densities compared to the other cells [41].

**Alkaline Fuel Cell (AFC):** The electrolyte is concentrated (85% by weight) potassium hydroxide (KOH) or less concentrated KOH (35-50% wt). The operating temperature for concentrated KOH is around 250°C, while that for the less concentrated KOH is lower. It is risky for Mars applications. The Martian atmosphere is rich in CO<sub>2</sub> and even a small leak in the cells would make it react with KOH and convert to potassium carbonate K<sub>2</sub>CO<sub>3</sub>, thus altering the electrolyte and bringing the entire system to a halt. Containment of the aqueous KOH electrolyte is more difficult than for a polymeric membrane [42].

**Phosphoric Acid Fuel Cell (PAFC):** Concentrated to 100%, phosphoric acid is used for electrolyte in this fuel cell. This kind of cell operates at temperatures of 150°C to 220°C.

**Molten Carbonate Fuel Cell (MCFC):** The electrolyte in this fuel cell is usually a combination of alkali carbonates or of sodium and potassium, and is retained in a ceramic matrix of lithium aluminium oxide. This is a high temperature cell operating at 600° – 700°C and would not be preferred for use in Mars.

**Solid Oxide Fuel Cell (SOFC):** The electrolyte in this fuel cell is a solid, nonporous metal oxide, usually yttrium oxide stabilized zirconium oxide. This is also a high temperature cell operating at 650° – 1000°C.

Of these different kinds, PEM would be most preferred for a Martian application. It operates at low temperature.

The energy options, along with their weights are listed in Table 9.1. The current technology as well as future forecasts are presented. Clearly fuel cells have the minimum system weight.

Final selection of the propulsion scheme is performed by a systematic point assignment technique. Rechargeable batteries along with solar cells on the lander are now treated as a single alternative renewable energy option rather than solar cells alone. This option is denoted as “Battery and Solar Cells (BSC)”. Table 9.1 shows the final comparison of the propulsion schemes. Each consideration is assigned a weighting factor based on its importance. The goal is to maximize payload capability with innovative utilization of a currently mature, proven and reliable technology on Earth. Thus 1, 2 and 3 have weight 10. It is highly desirable that in-situ or renewable energy sources are used to minimize mission cost and maximize mission capability. However these are secondary to proof-of-concept demonstration of a rotorcraft flight on Mars. Considerations 4, 5, and 6 have weight 5. Feature 8 is important and cannot be completely neglected. However, its effect has been kept minimal so that an attractive scheme is not penalized only because of this criteria. Each scheme is assigned points on a 0-10 scale. The points reflect how well they fulfill the considerations.

Considerations	Weighing factor	Propulsion Schemes								
		HP	HTJ	CB	LHLO	B	BSC	W	N	F
Current technology	10	10	6	1	5	10	10	0	0	10
Low system weight	10	6	4	2	5	6	6	0	0	10
Simplicity	10	0	0	0	0	9	6	0	3	5
In-situ energy	5	0	0	5	0	0	0	0	0	0
Renewable energy	5	0	0	0	0	10	10	5	0	0
Growth potential	5	6	4	2	3	3	3	1	2	10
Environmental safety	2	0	0	0	10	10	10	10	0	10
<b>Total points</b>		190	120	65	135	210	275	50	35	<b>310</b>

Table 9.1: Comparison of energy systems

Finally based on this systematic selection procedure we rate our energy options and associated propulsion

schemes in the following manner:

1) Fuel cells are clearly the best choice. They have minimum system weight with currently proven technology on Earth. They have good growth potential. They are reliable, and environmentally clean. They may provide means of conducting multiple missions in the future by using regenerative schemes.

2) Battery and solar cells are the next best option. However, they reduce the payload capability by 10 kg. With a reduced mission energy, higher payload can be achieved. This scheme gives us multiple mission capability, with simple, proven, current technology.

3) Batteries alone are the third option. Without solar cells it does not have multiple mission capability. However, it has the second highest payload capability after fuel cells. Batteries are simple, easy and safe energy management devices.

4) Hydrazine internal combustion engine technology is proven on Earth. However, with current technology, payload will be much smaller than for battery or fuel cell systems.

5)  $LOX + LH_2$  tip jet schemes are theoretically feasible. However their practical implementation may not be feasible. The engines are massive.

6) Hydrazine tip jets would suffer from the same drawback as the  $LOX + LH_2$  system, and would provide even less payload.

7) Wind and nuclear propulsion schemes are not feasible.

Selection of a particular fuel cell, battery and solar cell type are now described. We choose **Proton Exchange Membrane fuel cells**. Their low temperature operation, hence faster startups and quick reponse to changes in power demand are best suited for use in low temperature Martian environment. Corrosion problems minimal. They have Very high power densities which maximizes payload capability. They exhibit no risk of carbonate formation in case of fuel cell leak, unlike AFC. Polymeric membrane easy to contain, unlike the aqueous KOH electrolyte system of AFC. They have low weight, cost and volume. Immobilized electrolyte membrane simplifies sealing in the production process. Apart from these there are some specific advantages of using PEM cells in Mars, which cannot be realized on terrestrial applications. Use of pure reactants avoid contamination problems. With pure reactants higher power densities can be achieved. With pure reactants current densities as high as  $2A/cm^2$  can be achieved [41]. An increase in the pressure of the oxygen increases cell performance. On Earth, this performance improvement must be balanced against the energy required to pressurize the reactant gases. In our case, the reactants are already stored under supercritical pressure, in liquid form. For one time use, expensive high performance cell membranes like the Dow membrane [41] can be used. Also high platinum loaded electrodes can be used.

We choose **lithium ion rechargeable cells**. From Figure 2.1, lithium ion cells have the highest energy and power density. The values plotted in Figure 2.1 are the actual values for a battery produced by SAFT. Hence it is a currently obtained and proven technology. Lithium rechargeable systems have the highest growth potential and are identified for fulfilling long term vehicle traction needs.

We have shown that solar cells used on the Mars Pathfinder lander are enough to harness the mission energy in a little over 3 days. **GaAs/Ge solar cells** are hence sufficient for our purpose. For further protection from radiation damage, **InP** solar cells may be used.

### 9.3 Answers to the key questions

Based on the systematic survey of power systems, here are the answers to the key questions:

1) We can generate the energy required for the mission fully on Mars. This is using solar energy. Based on the energy generation rate of the Pathfinder lander cells [43], the mission energy can be collected within 4 days.

2) This will not reduce the weight that needs to be transported from Earth. If we neglect the effects of dust and other atmospheric factors and assume that the available solar intensity is  $590 \text{ W/m}^2$  [35], then considering a thermodynamic efficiency ceiling of 30% [34] for solar cells, power per unit area would be  $177 \text{ W/m}^2$ , and  $33.89 \text{ m}^2$  of solar cell area will be required. As a comparison the disc area based on preliminary studies is  $29.2 \text{ m}^2$ . Even state of the art space cells have, as was discussed before, power per unit mass values only as high as  $130 \text{ W/kg}$ , which requires  $46 \text{ kg}$  of solar cells. From actual Pathfinder data the required areas and mass of solar cells would be  $1200 \text{ kg}$  and  $133 \text{ m}^2$ . Hence producing power from solar cells while the helicopter is in flight is not feasible. We can make use of solar power by storing it in a battery which flies with the helicopter. This battery needs to be carried from Earth, and hence there is no take off weight reduction from Earth.

If in the near future the combustion of metals in the presence of  $\text{CO}_2$  as an oxidizer becomes a proven technology, substantial take off weight reduction would be obtained. Only the metallic fuels aluminum or magnesium will be required to be carried to Mars.

3) Renewable energy sources will provide multiple mission capability. With current technology this source can only be solar energy. The solar cells would be attached to the lander and the helicopter will have to come back and get its battery recharged if it were to fly multiple missions.

Another scheme will be to use regenerative fuel cells. Solar cells will absorb energy. Once one cycle of operation of the fuel cells is complete, an electrolyzer will go through the reverse procedure of turning water into oxygen and hydrogen. The energy absorbed by the solar cells will be used for this purpose. A water tank to store the water, an electrolyzer, associated controls and ancillary equipment will be required. This technology has not been demonstrated yet.

4) With current technology it is not possible to have an in-situ propellant production scheme that will supply propellants autonomously. Reference [44] proposes a concept of producing oxygen and carbon dioxide from the Martian atmosphere. They will then be used as propellants for rocket propulsion of a ballistic hopper. However, the proposal is speculative in nature, and the concept is massive: the entire propulsion system weighs  $1100 \text{ kg}$ .

5) The answer to this question is obtained from the answer to the second question. It is not possible to generate energy in-situ as the helicopter flies.

6) Fuel cells would provide a clean, environment friendly propulsion scheme.

## 10 POWER PLANT DESIGN

The powerplant is a fuel cell system. It supplies power to an electric motor which rotates the rotor. The fuel cell system consists of the fuel cell stack, fuel, fuel tanks, thermal and water management units and ancillary control equipment. The fuel cell system is designed to provide 10% more energy than required by the extended mission.

The operation and basic cell description is presented first. Then, fuel cell stack design is described. The fuel storage system and the fuel cell system operation are outlined. Critical system issues are identified. Finally, ways to further improvements are cited.

Currently feasible technology is use throughout. The technical advice from Fuel Cells 2000 [45] was sought during the exercise.

## 10.1 Fuel cell description

A schematic representation of a fuel cell with the reactant/product gases and the ion conduction flow directions through the cell is shown in Figure 10.1.

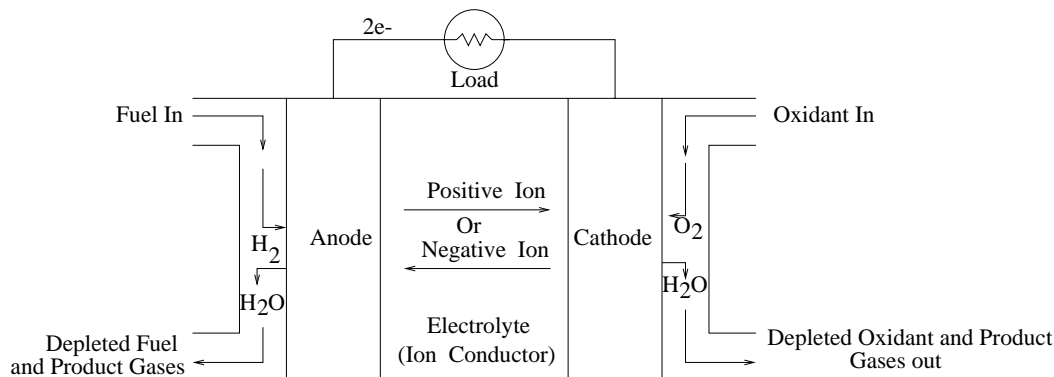


Figure 10.1: Schematic of an individual fuel cell

The fuel cell stack consists of **Proton Exchange Membrane** (PEM) fuel cells and uses pure hydrogen and pure oxygen as fuel. Each fuel cell has two platinum impregnated porous electrodes – the anode and the cathode. Sandwiched between the two electrodes is a hydrated, proton conductive perfluorinated sulphonic acid polymer membrane. The electrodes are cast as thin films and bonded to the membrane. Hydrogen gas flows in on the anode side of the fuel cell; the catalyst, platinum, separates the gas into positively charged hydrogen ions (protons) and free electrons. Electrons cannot pass through the membrane and are forced to flow through an external circuit. The protons, which remain solvated with a certain number of water molecules, diffuse through the membrane to the cathode to react with oxygen and the returning electrons. Water is subsequently produced at the cathode.

## 10.2 Fuel cell stack design

Polarization curves of PEM fuel cells achieved with current technology are produced in Fig. 10.2. Current density, which is the current flowing through each cell divided by the active area of the cell, increases with a decrease in cell potential. The curves of Energy Partners Inc. [46] are for a hydrogen-air single cell and a 10 cell stack both at 300 kPa (43.5 psi, 3 atm) and 60° C. With pure oxygen, higher current densities are expected. The curve given by AeroVironment is for a pure hydrogen, pure oxygen fuel cell to be used in Helios [40]. Our fuel cell performance would be close to the AeroVironment plot. However, we consider the multi-cell performance results of Energy Partners Inc., for our design calculations. They provide actual experimental results for multi-cell stacks and choosing this allows us to operate within a comfortable and easily achievable technology level. Fig. 10.3 shows the cell power densities obtained from the same curves. Cell power density is obtained by multiplying cell current density and cell potential.

The mission energy requirement for the baseline and extended missions are 3025.47 Wh and 3267.44 Wh respectively. The stack is designed for an average power output of 4.63 kW. This is the average power requirement over both the baseline and extended missions. The fuel requirements are calculated to provide 10% more mission energies than required by the baseline and extended missions. This safety margin is provided for any deviation in mission trajectory due to gusts.

The voltage output from the stack is taken as 188V to account for the electric motors, avionics, controls

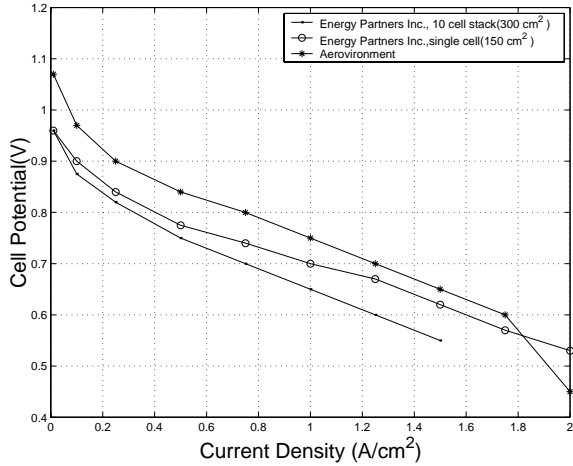


Figure 10.2: Performance of PEM fuel cells

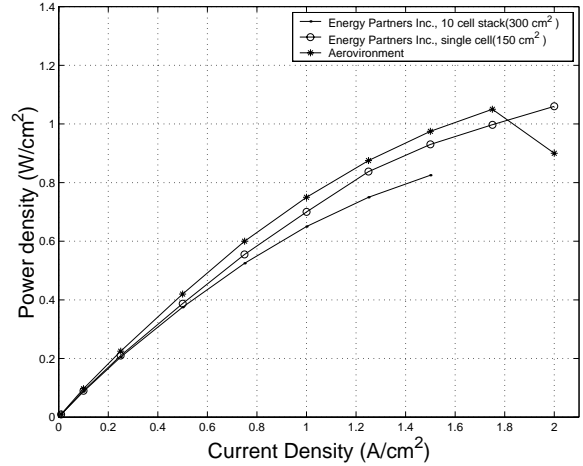


Figure 10.3: Power density of PEM fuel cells

and payload. The thickness of each cell is  $4400\mu\text{m}$  which is taken from [46]. Each cell has a density of  $2500\text{ kg/m}^3$  with porosity of 60%, which means that 40% of the volume of each cell is hollow. The efficiency of the electric motor is 90%. Hydrogen utilization is 100%. Oxygen utilization is assumed 100%, based on the technical advice of Fuel Cells 2000 [45]. Masses of fuel required, fuel stack and tanks have been estimated for different combinations of cell voltages and current densities. The results for the baseline mission are shown in Fig. 10.4. Operating at higher current density (hence higher power density) minimizes stack mass while operating at higher cell voltage minimizes fuel mass.

Corresponding to each system mass, energy densities and the power densities of the fuel cell system, for the baseline mission are plotted in Fig. 10.5. Total mission energy divided by the system mass gives the energy density. Average power output divided by the system mass gives the average power density. From this curve the operating point of a cell has been chosen as 0.65 V and  $1\text{ A/cm}^2$ . This is an easily achievable operating point with current technology [41]. This is not the condition for minimum system mass, but close to it. During hover, the power requirement is higher, and thus the current density drawn from each cell is higher. The operating point is chosen such that the current density drawn during hover has a comfortable margin from the highest achievable value as given in the performance curve, Fig. 10.2. The energy density and power density achieved at the operating point are 316 Watt-hours/kg and 483 Watts/kg, Fig. 10.5. The maximum power output capacity is 6.43 kW.

For the extended mission stack design remains the same, only excess fuel need to be supplied. Also the tank masses slightly increase in order to accommodate this increased fuel. The energy density and power density of the system in case of the extended mission becomes 350 Wh/kg and 452 W/kg.

### 10.3 Fuel storage

The fuel storage system is designed to store the fuel requirement for the extended mission. The fuel cell uses pure hydrogen and pure oxygen as reactants. The required masses of hydrogen and oxygen for the entire mission are calculated as 0.23 kg and 1.83 kg respectively. The volumes of  $LH_2$  and  $LO_2$  are  $3300\text{ cm}^3$  and  $1600\text{ cm}^3$  respectively.

The hydrogen and oxygen are stored in their respective storage tanks at cryogenic temperatures and supercritical pressures. The storage temperature of liquid oxygen ( $LO_2$ ) is  $-176^\circ\text{C}$  and  $-251^\circ\text{C}$  for liquid hydrogen

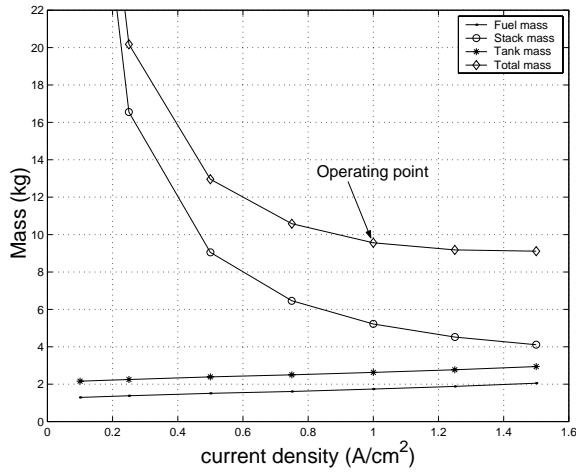


Figure 10.4: Mass of fuel cell system

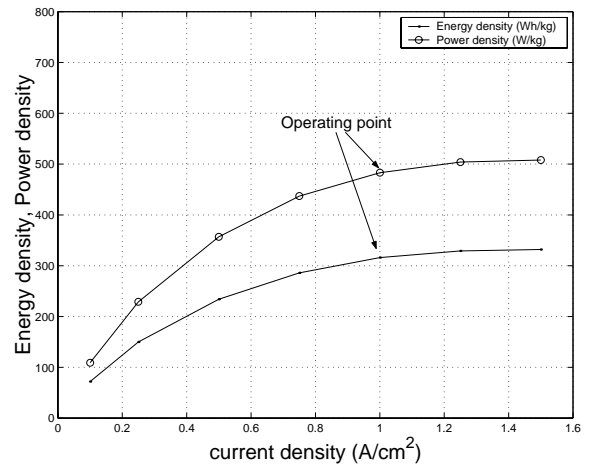


Figure 10.5: Energy density and power density

( $LH_2$ ). The  $LH_2$  tank is at a pressure of 210 psi (1.44 mPa, 14.4 earth atm.) and the  $LO_2$  tank is at a pressure of 820 psi (5.65 mPa, 56.5 earth atm). These values are based on space shuttle values. Like the space shuttle tanks, these are double walled thermally insulated tanks with a vacuum annulus between the inner pressure vessel and the outer shell of the tank. The inner pressure vessels are kept supercold by minimizing conductive, convective and radiant heat transfer. Low conducting supports hold the inner vessel in place within the outer vessel. Radiation may be reduced by using a shield between the inner and outer vessels. Convection is minimized by maintaining a vacuum between the inner and outer vessel, by a vacuum pump. Each tank will have heaters to add pressure to the reactants during depletion to control pressure.

Applying the square-cube law to the fuel weight and tank weight of space shuttle data, the tank weights are estimated as 3.06 kg and 2.82 kg for hydrogen and oxygen tanks respectively. The hydrogen tank is made of aluminium 2219. The oxygen tank is made of aluminium 2219 for the outer vessel and Inconel 718 for the inner vessel. However, the tank weights can be reduced substantially by using high strength filament wound Kevlar 49, with thin metal liners [47]. Assuming a knockdown factor of 50% for the tank weights, based on densities of aluminium alloys and Kevlar 49 (aluminium alloys -  $2800 \text{ kg/m}^3$ , Kevlar 49 -  $1380 \text{ kg/m}^3$ ), a total tank weight of 2.95 kg is assumed.

## 10.4 System operation

The fuel from the tanks flows into the stacks through relief valves. The pressure of hydrogen and oxygen is reduced to 43.5 psi (308 kPa, 3 Earth atm) by the valves. A fuel oxidant method of cooling is adopted. Fuel for cooling is collected in an intermediate coolant chamber through a valve. It is drawn from the chamber based on a controller logic. The water produced is collected in an intermediate water chamber from where the excess is thrown out. In case water is needed for humidization it can be taken from this water chamber. The electricity generated can be carried to the main bus of the vehicle for distribution. The layout of the fuel cell system is shown in Fig. 10.6.

To illustrate the operation of the fuel cell system we consider the power requirement during the baseline mission as shown in Fig. 10.7. The corresponding current density drawn from each cell during the mission is plotted in Fig. 10.8. The maximum current density requirement is during hover,  $1.29 \text{ A/cm}^2$ . Maximum power density of the system is also achieved during hover,  $561 \text{ W/kg}$ . Each cell operates at power density of 0.78

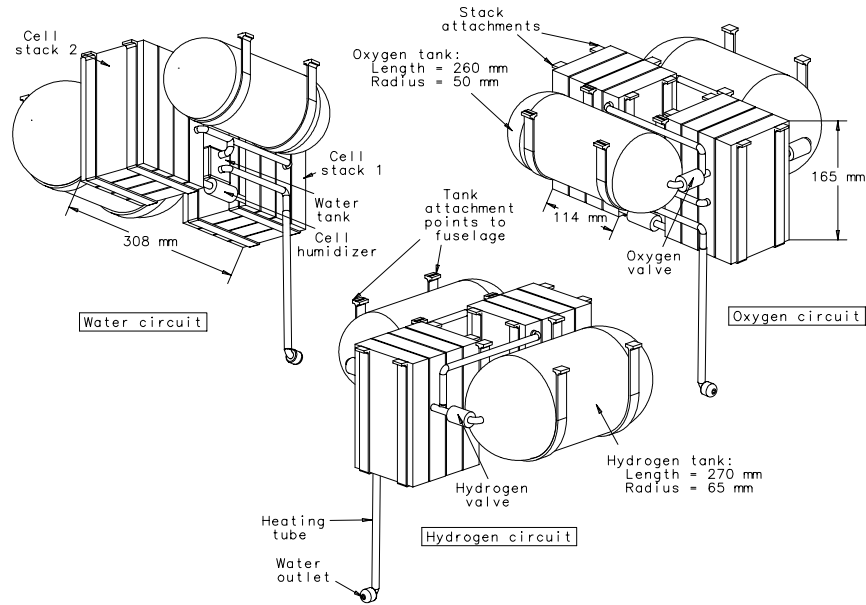


Figure 10.6: Fuel cell system

$W/cm^2$  during hover. An operating point higher than the one selected pushes the hover current density value close to the limit. Fig. 10.9 show the fuel consumption rate during flight. Fuel consumption as a function of mission time is shown in Fig. 10.10. The fuel consumption rate is proportional to the current density. It is the same as the rate at which water is produced.

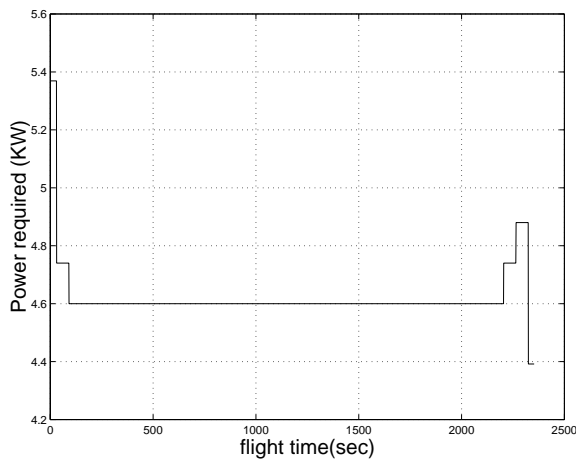


Figure 10.7: Mission power profile

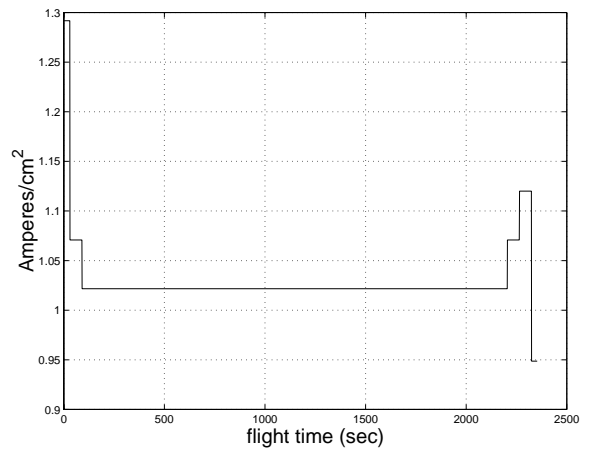


Figure 10.8: Current density drawn from each cell

Fig. 10.11 show the cell voltage during the baseline mission. The cell voltage is always between  $0.59V$  and  $0.65V$ . High cell efficiency is obtained between  $0.6V$  to  $0.7V$  [48]. Fig. 10.12 show the stack voltage output during the mission. The stack voltage never goes below  $160V$ , which is the driving voltage of the motor. This means a voltage converter may not be needed, and a regulator will suffice, and this will save weight.

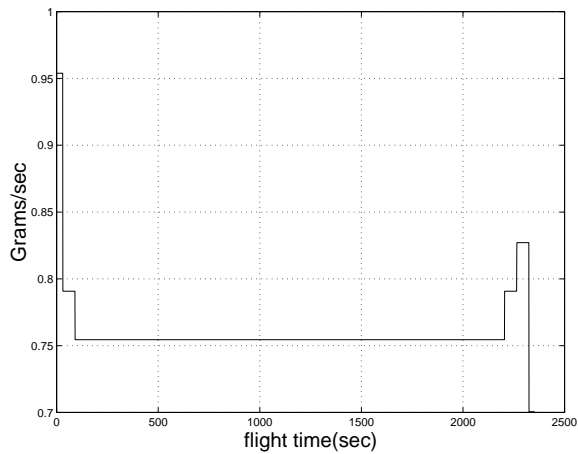


Figure 10.9: Fuel consumption rate

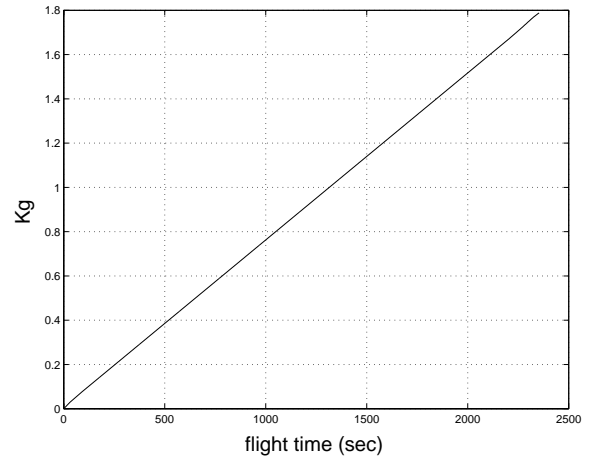


Figure 10.10: Mass of fuel consumed during flight

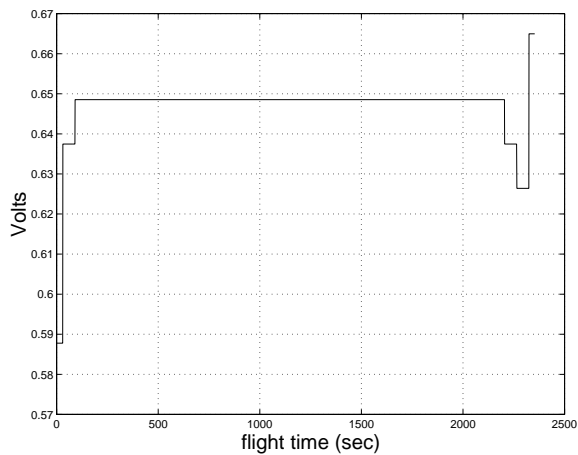


Figure 10.11: Cell voltage during mission

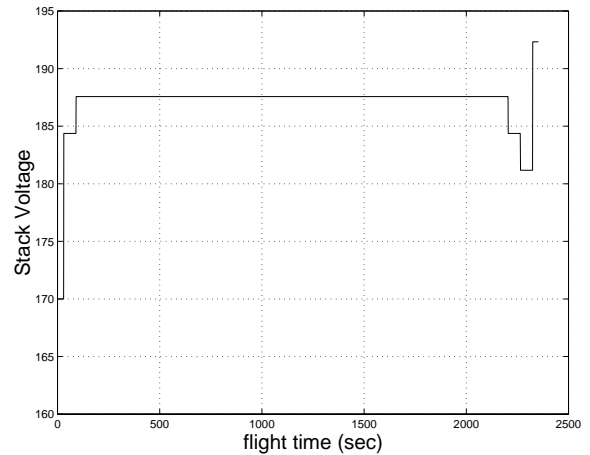


Figure 10.12: Stack voltage during mission

## 10.5 System issues

The following issues are critical to the performance of the fuel cell system.

1) An increase in **operating pressure** increases power density and reduces stack weight [41]. On the other hand high pressure tends to pull the stack apart and to reduce electrical contact with the cells [40].

2) A PEM cell has an **operating temperature** of  $80^{\circ}\text{C}$  to  $120^{\circ}\text{C}$ . The energy needed to start the operation of the fuel cells is low, and so this energy can be harnessed from the lander. Once the reaction starts, the heat generated would be sufficient to sustain the reaction. The higher the temperature, the better the performance. However, temperatures higher than  $120^{\circ}\text{C}$  can lead to problems of membrane dehydration and subsequent loss of ionic conductivity [41].

3) **Water humidification** on the cathode side may be employed, if necessary [45]. Water is produced as liquid in a PEM fuel cell. Water balance must be maintained in the cell. Ballard Power Systems of Canada has demonstrated stack designs and automated systems that manage water balance successfully [41].

4) **Cooling** by fuel and oxidant instead of conventional heat exchangers may be preferred [45].

5) With pure reactants and high efficiency, the gas flow is very low. Hence a **pump** is required to remove

the excess water.

6) The **byproduct** water is collected in a water tank and thrown out whenever it is filled.

### 10.5.1 Growth potential

PEM fuel cells are being intensely developed and researched by several companies for automotive and stationary applications, e.g., Hydrogenics Inc. and Energy Partners Inc. [46] [48]. Apart from the guaranteed performance benefits for pure reactants further improvements of performance can be achieved in future. Design of thinner membranes with lower resistivities will increase power densities [41]. With such changes system weight can be brought down to 6.45 kg. Refining electrode design will help to reduce costs.

## 10.6 Stack technical specifications

The stack technical specifications are shown in Table 10.1. The fuel cell stack is the power plant of MARV. Hence essentially these are the power plant specifications.

Number of cells	290
Active area	27 cm <sup>2</sup>
Average power output	4.63 kW
Maximum power capability	6.43 kW
Nominal cell voltage	0.65V
Nominal current density	1 A/cm <sup>2</sup>
Cell temperature	80°C (176°F)
Cell pressure	43.5 psi (308 kPa, 3 Earth atm)
Reactants	LH <sub>2</sub> /LO <sub>2</sub>
Hydrogen flow rate	1.0 x stoich
Oxygen flow rate	1.0 x stoich
Cooling system	Fuel and oxidant cooling
Module dimensions	2.7 x 10 x 132 cm
Number of modules	8
Weights	Baseline mission(Extended mission)
Stack weight	5.22 kg (5.22 kg)
Hydrogen weight	0.21 kg (0.23 kg)
Oxygen weight	1.69 kg (1.83 kg)
tank weight	2.80 kg (2.95 kg)
Total weight	9.94 kg (10.25 kg)
LH <sub>2</sub> volume	3100 cm <sup>3</sup> (3300 cm <sup>3</sup> )
LO <sub>2</sub> volume	1500 cm <sup>3</sup> (1600 cm <sup>3</sup> )
Energy density	316 Wh/kg (350 Wh/kg)
Maximum power density	560 W/kg (452 W/kg)

Table 10.1: Stack technical specifications

# 11 SELECTION OF ELECTRIC MOTOR

## 11.1 DC motor

The output of the powerplant is used to run a DC electric motor. The speed vs. torque, current vs. torque and controlling of speed by input voltage are shown in Fig. 11.1. The advantages of DC motors over rotating field motors are easily seen. For example, current increases linearly with load torque, thus higher efficiency may be expected over the working range; and speed can be easily controlled by varying the supply voltage  $V$ . The disadvantages are that they have a limited lifetime; there may be unreliable contact, especially at low voltages; there may be electric interference, and there may be additional noise.

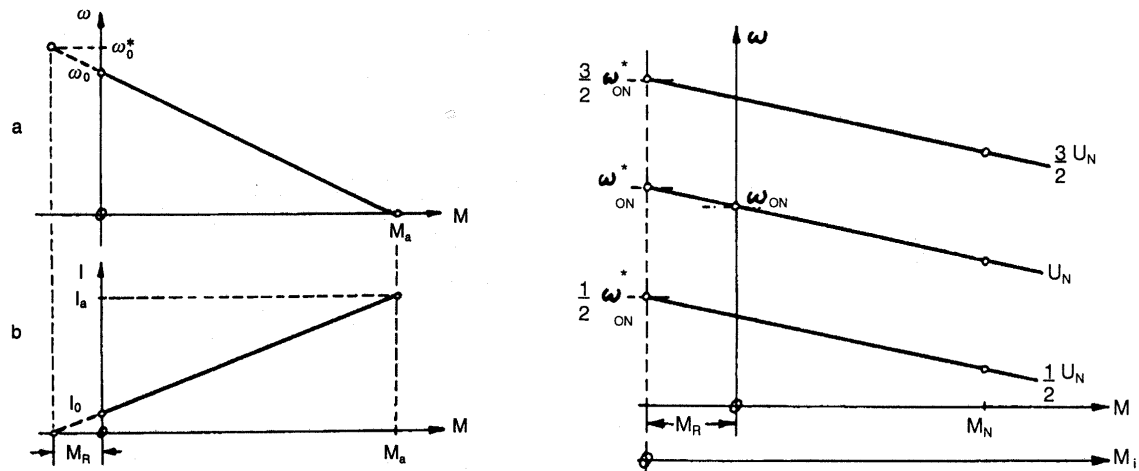


Figure 11.1: DC motor

These disadvantages, compared to induction motors, led to the development of brushless DC motors, which combine the advantages of DC motors together with the robustness of induction motors.

## 11.2 Brushless DC motors

Solutions to the problem of driving a motor from a direct voltage supply without brushes are:

- combination of induction motor and constant frequency inverter
- combination of synchronous motor and constant frequency inverter
- a built-in electronic commutator in place of the conventional mechanical commutator

In the power range of up to 10 W, the first solution is excluded on account of the low efficiency of the induction motor. With constant inverter output frequency, the motor speed is almost constant, but the starting torque is small compared with the classical DC motor. In the higher power range, the combination of inverter with induction motor is generally satisfactory.

Combining the synchronous motor and inverter results in higher efficiencies under certain working conditions, but the start and run-up present special problems. Also, operation is rough because of the synchronous motor's tendency towards oscillation.

The best solution is therefore the substitution of the mechanical commutator with an electronic commutator while preserving the advantages of DC motors. This 'electronic commutator' must switch in the coils that develop

the torque by electronic means at those times when the rotor is in the right position relative to those coils.

### 11.3 Speed setting and control

The angular velocity  $\omega$  of the brushless DC motor can be adjusted by changing the supply voltage  $V$ .

If only a constant direct voltage supply is available, reduction of speed can be achieved by means of a series resistor which achieves voltage reduction at the motor, by a voltage divider, a transistor or a DC chopper with its attendant low heat losses.

The same effect can also be achieved using the full supply voltage, but with some power being absorbed by appropriate control of the transistors in the stator circuits. When the transistors are not fully saturated, there is a resultant power loss, due to the voltage drop. This must be allowed for in the design. The increased power loss can be avoided if the switching frequency is high compared with the motor speed. Variations in switch-on/switch-off time can be used to control the average voltage that is applied to the winding. Current interruptions must be prevented by means of fast acting freewheel diodes.

Regulating the speed presupposes a means of measuring the speed, together with a regulator that operates in the manner described above on the motor winding voltages. The motor speed can be measured by means of an AC tachometer generator whose induced voltage magnitude or frequency is a measure of the speed. An exact setting of the motor speed is achieved when the tachometer's frequency and phase angle are the same as those of the reference signal generator. Integrated circuit components are available to fulfill these somewhat demanding requirements.

### 11.4 Selection of brushless DC motor

Since we need a motor with an output power of 5 kW, we should keep the weight of the motor as small as possible. Aveox Company has developed small, high performance brushless DC motors. A number of their products are high-torque, low-weight airborne motors.

We selected a brushless DC motor which was designed and built for a small unmanned electric helicopter. A small high-power density amplifier is fitted on the back of the motor and an integrated centrifugal cooling fan is designed to augment power dissipation on the stator and controller. At only 1.9 kg, the complete motor/controller/cooling fan produced 4.23 Nm of torque at 11500 RPM with a 160 VDC, 34.2 A input. Overall system efficiency is 90%.

## 12 TRANSMISSION DESIGN

Due to the strict weight constraint, the weight of the transmission was used as the primary design parameter. In addition, load paths, integration of the gearbox and the configuration of the airframe were also considered. Four kinds of transmission configurations were evaluated during the design process.

### 12.1 Problem formulation

The rotor RPM is 650 and the powerplant is a brushless DC electric motor with a maximum RPM of 11500. This leads to an 18:1 reduction ratio. The transmission should also provide an output in two opposite directions of rotation for the coaxial configuration. First, we considered the possibility of the complete elimination of the

transmission system. Direct control for electric motors has been widely used, but for our case, where the power is 5kW, such control is not easy and a transmission is needed.

## 12.2 Trade-off study

Four transmission configurations were considered. The first is shown to the left in Fig. 12.1. It has a two stage reduction: the first stage is a planetary gear train and the second stage uses spiral bevel gear meshing. In this configuration, the power and the load are not along the same line and this requires a wider fuselage. This would lead to an increase in weight and drag.



Figure 12.1: Transmission configurations 1 and 2

The second configuration is shown to the right in Fig. 12.1. It also has a two stage reduction gear. The first stage uses one small pinion driving two big gears and the second stage uses two small pinions driving one bull gear. The final stage has spiral bevel gears to provide opposite direction rotation to the two rotor shafts. This configuration has the power and load along the same line and would lead to a more compact fuselage. However, the bevel gears at the final stage can't be easily installed in the gearbox.



Figure 12.2: Transmission configurations 3 and 4

The third configuration is shown to the left in Fig. 12.2. This uses two-stage planetary gears for the speed reduction. At the final stage, it uses four spiral bevel gears to get the opposite rotation direction of the two shafts. The power and the load are along the same line, and thus the lateral size of this configuration can be minimized. A problem is the installation of bearings for the four bevel gears.

The fourth configuration is very similar to the second and is shown to the right in Fig. 12.2. The difference is that instead of using bevel gears to get two directions of rotation, an internal gear is used. However, the lateral size of this design is relatively large compared to the third configuration.

Configuration 1 was eliminated because of size and weight considerations. Configuration 2 was eliminated because configuration 4 has an advantage over it. Configurations 3 and 4 were studied in more detail to arrive at the final design configuration. Based on the detailed design of configurations 3 and 4, we find that the weight and size of configuration 3 is lower than configuration 4. The weight of configuration 3 is 75% of configuration 4. The lateral size of configuration 3 is 72% of configuration 4. In the design process, the rotor control design was carried out concurrently with the transmission design. For the yaw control, we need a linkage which goes through the inner shaft to connect the yaw control level and the yaw control servo. Since the center line of the shaft and electric motor for configuration 3 is occupied by shafts, we cannot install this yaw control linkage. Also, the installation of the bearings for configuration 3 is not as simple as it is for configuration 4. Therefore, we choose configuration 4 as our final transmission design, although it is heavier and larger than configuration 3.

### 12.3 Detailed design of configuration 4

For configuration 4, there were two design constraints. Since this design uses parallel spur gear transmission, the diameter of the three gear meshes shown in Fig. 12.3 are constrained to each other.

We selected a first stage reduction ratio of 3 and a second stage reduction ratio of 6. We needed to make the sum of the radius of the first mesh D1 equal to that of the second gear mesh D2, and the sum of the diameter of these two meshes equal to the difference in diameter of the internal gear mesh D3. This was not an easy requirement to satisfy. The results for the first, second and third meshes are shown in Tables 12.1, 12.2 and 12.3 respectively.

n \ P	10	16	24	32	48	64
10	1,0.12,4	0.63,0.30,2.5	0.42,0.67,1.67	0.31,1.2,1.25	0.21,2.69,0.83	0.16,4.79,0.63
20	2,0.03,8	1.25,0.07,5	0.83,0.17,3.33	0.63,0.30,2.5	0.42,0.67,1.67	0.31,1.20,1.25
30	3,0.02,12	1.9,0.04,7.5	1.25,0.08,5	0.93,0.14,3.75	0.62,0.30,2.5	0.46,0.54,1.87
40	4,0.01,16	2.5,0.02,10	1.67,0.05,6.67	1.25,0.08,5	<b>0.83,0.17,3.33</b>	0.62,0.30,2.5
50	5,0.01,20	3.1,0.02,12.5	2.08,0.03,8.33	1.56,0.05,6.25	<b>1.04,0.11,4.16</b>	0.78,0.20,3.12
60	6,0.01,24	3.75,0.01,15	2.5,0.01,10	1.87,0.02,7.5	1.25,0.04,5	0.93,0.07,3.75

Table 12.1: Sizes of first stage gear

In these tables,  $n$  stands for the number of teeth and  $P$  stands for the diametral pitch. The first number in each column is the pitch diameter of the pinion, the second is the width, and the third is the sum of the diameters of the two meshing gears. All sizes are in inches.

In the third table, the first two numbers have the same meaning as those from the previous tables, but for the third number, since it is for the internal gear meshing, represents the difference in diameter between the internal gear and external pinion.

From the three tables, we cannot find the cross point where the two above constraints can be met. The items which are shown in bold are the gear sizes which are near the cross point. In order to find the design which satisfies the constraints, we can choose more tooth number candidtes around these points.

After more investigations, we selected diametral pitch of 48 for all the gears. For the first gear meshing, the

n \ P	10	16	24	32	48	64
10	1,0.31,7.0	0.62,0.80,4.4	0.41,1.77,2.91	0.31,3.15,2.18	0.20,7.1,1.45	0.15,12.6,1.09
20	2,0.08,14	1.25,0.20,8.75	0.83,0.45,5.83	0.63,0.79,4.37	<b>0.41,1.77,2.91</b>	0.31,3.15,2.18
30	3,0.04,21	1.87,0.09,13.12	1.25,0.20,8.75	0.93,0.35,6.56	<b>0.62,0.79,4.37</b>	0.46,1.40,3.28
40	4,0.02,28	2.5,0.05,17.5	1.66,0.12,11.7	1.25,0.20,8.75	0.83,0.45,5.83	0.62,0.80,4.37
50	5,0.02,35	3.12,0.04,21.8	2.08,0.08,14.5	1.56,0.13,10.9	1.04,0.29,7.29	0.78,0.51,5.46
60	6,0.001,42	3.75,0.03,26.25	2.5,0.05,17.5	1.8,0.09,13.1	1.25,0.20,8.75	0.93,0.35,6.5

Table 12.2: Sizes of second stage gear

n \ P	10	16	24	32	48	64
10	1,0.31,5	0.62,0.80,3.1	0.41,1.77,2.08	0.31,3.15,1.56	0.20,7.1,1.04	0.15,12.6,0.78
20	2,0.08,10	1.25,0.20,6.25	0.83,0.45,4.16	0.63,0.79,3.12	0.41,1.77,2.08	0.31,3.15,1.56
30	3,0.04,15	1.87,0.09,9.37	1.25,0.20,6.25	0.93,0.35,4.68	<b>0.62,0.79,3.12</b>	0.46,1.40,2.34
40	4,0.02,20	2.5,0.05,12.5	1.66,0.12,8.3	1.25,0.20,6.25	<b>0.83,0.45,4.16</b>	0.62,0.80,3.12
50	5,0.02,25	3.12,0.04,15.6	2.08,0.08,10.4	1.56,0.13,7.8	1.04,0.29,5.20	0.78,0.51,3.9
60	6,0.001,30	3.75,0.03,18.75	2.5,0.05,12.5	1.8,0.09,9.3	1.25,0.20,6.25	0.93,0.35,4.6

Table 12.3: Sizes of internal meshing gear

pinion has 44 teeth and the gear has 132 teeth. For the second stage, the pinion of the external meshing has 25 teeth while the gear has 150 teeth. The pinion for the internal meshing has 35 teeth and the gear has 210 teeth. To make the design feasible, some gears widths have to be increased. The width of the first pinion is 0.20 inch (5.1 mm). The first gear has a width of 0.12 inch. The width of the second pinion of the external meshing is 0.63 inch. The width of the second gear of the external meshing is 0.60 inch (13.0 mm). The pinion of the internal meshing is 0.32 inch (8.1 mm) wide. The internal gear has a width of 0.39 inch (9.9 mm). The internal gear has a base disk of 0.16 inch width. The maximum lateral size for this design is 6.42 inch (163.1 mm). The weight of all the gears is 2.93 lbs (1.329 kg).

In Fig. 12.4, the meaning of the term 'hollow ratio' is the ratio of the hollow inner diameter to the diameter of the shaft. It can be seen that the bigger the diameter of the shaft, the lighter the shaft will be. The weight of the shaft decreases with an increase in the ratio of the inner radius to the outer radius. Since the yaw control linkage passes through the center of the inner shaft, we need to have enough space in the shaft. This also helps in weight reduction, because we can make the shaft lighter when increasing its size. Also, for the installation of the bearings between the inner shaft and outer shaft, we should have some clearance between them. In our case, a 0.20 inch (5.1 mm) clearance is needed. Based on these considerations, we can select the size of the shafts from Fig. 12.4. The inner shaft has an outer radius of 0.79 inch (20.1 mm) and hollow ratio of 0.95, which gives an inner radius of 0.75 inch (19.1 mm). The outer radius for the outer shaft is 1.02 inch (25.9 mm) and the hollow ratio is 0.96, which gives an inner radius of 0.98 inch. From the configuration design of the whole vehicle, the inner shaft has a length of 26 inches and the outer shaft has a length of 15.7 inches.

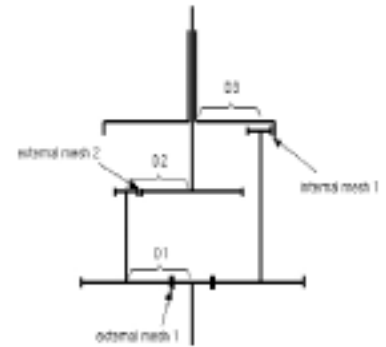


Figure 12.3: Design constraint of configuration 4

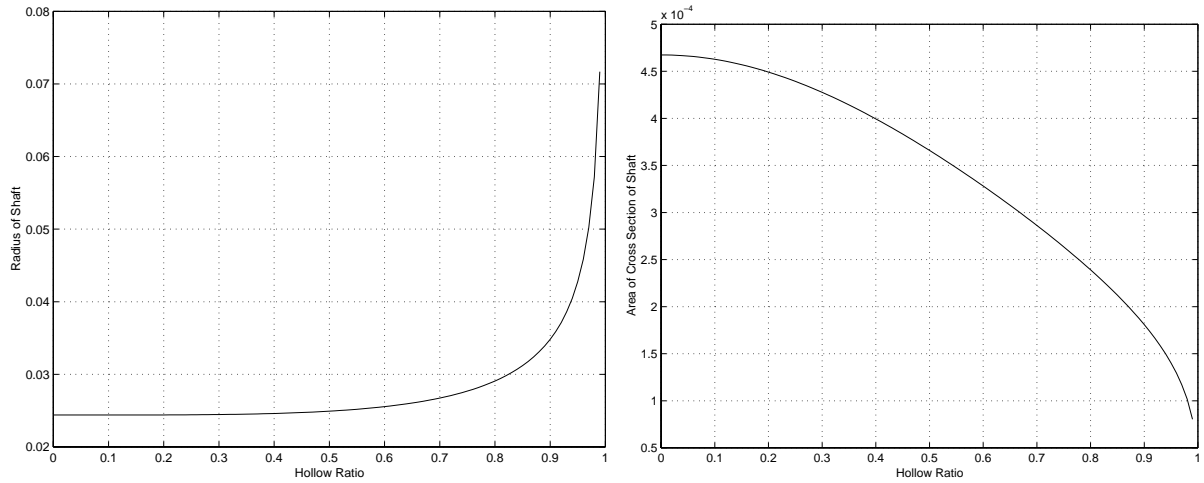


Figure 12.4: Hollow ratio effect on the diameter and cross section area of the shaft

There are three critical design conditions: two during the landing phase, and one during flight. We assume that when the vehicle is landing, there may be a maximum load factor of 10. Under this load condition, the hub and rotor will transmit a large external load to the shaft. The shaft is checked for compression buckling and yield. During flight, the shaft is subject to the torque of the rotor, and thus in this case it may have torsional bucklings.

First, we checked the compression yield. For the landing condition, the compression stress of the inner shaft is 783.3 psi and 631.2 psi for the outer shaft, while the yield stress of tension for our shaft is 50,000 psi. This gives safety factors of 63.6 and 79.3 for the inner shaft and outer shaft, respectively.

Next, we checked the compression buckling during re-entry deceleration. We idealized both the inner and outer shafts as having unconstrained ends. The critical compressive stress for the inner shaft is 867,640 psi and 699,130 psi for the outer shaft. Both of these shafts have a factor of safety of 1107 for compression buckling.

Finally, we checked the torsional buckling. For this we assumed the shafts had hinged ends. The critical shear buckling stress for the inner shaft and outer shaft are 88,433 psi and 99,776 psi respectively. Both of these figures are much larger than the shear yield strength of 30,000 psi of our shafts, and therefore it was concluded that our shafts could meet the torsional buckling requirement.

Due the high factors of safety, the shafts will also be highly resistant to fatigue failure.



Figure 12.5: Integration of transmission

## 12.4 Integration of structure

The integration of the transmission is shown in Fig. 12.5.

The transmission system is housed in a gearbox to prevent the dust on Mars from getting inside. Also, the gearbox, which is made of composites, provides the structural support for the bearings. The figure in the folded graph shows the internal structure of the gearbox. The gearbox case is composed of four parts: the top cone, the middle cylinder, the middle cone and the bottom cylinder. These four parts can be glued together. A disk is

mounted on the middle cylinder part, which holds the bearings for the first stage transmission output as well as the bottom of the yaw slide. There is an upside down cone inside the top cone case. This design is for holding the bottom bearing of the outer shaft. The gearbox case is bolted to the fuselage attachment structure, which is made of steel. The top of the fuselage attachment holds another bearing for the outershaft. It has four fuselage attachment points to connect the pipeline. The lift should be carried through these four attachment points to the pipeline and to the fuselage. The electric motor and the clutch are fixed on the gearbox. The outer shaft is supported by the gearbox through two bearings. The inner shaft is supported by two bearings, one between the outer shaft and inner shaft, and another on the gearbox. The gearbox is fixed on the fuselage by eight pipelines.

## 12.5 Lubrication of gears

Bray grease 604, which contains Bray oil 814, has superior low temperature performance and has been used at low temperature in the Mars Pathfinder Rover actuators. Thus, it is used in our design for the lubrication of the transmission system.

# 13 ROTOR CONTROL SYSTEM

It was decided that since the MARV is an unmanned helicopter, it was not necessary to ensure stringent handling qualities as would be done for a conventional helicopter, and instead the control system should be designed for maximum control. The control system should be capable of giving the collective and cyclic inputs in addition to differential input for yaw control. For the control of the rotors, a number of ideas were analysed. They were: (1) conventional swashplate, (2) servo-flap operated by mechanical linkages, (3) servo-flap driven by smart actuators, (4) all-movable tip driven by smart actuators, (5) shaft tilt and (6) control by CG shift. These designs will be explained in the next few sections.

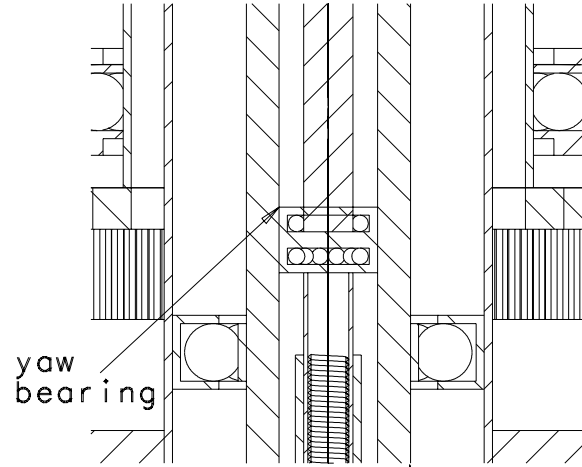
Kaman has used **servo-flaps** for rotor control for many years in their K-Max and Seasprite helicopters. The major advantage of this design is that only a small actuation force is needed for control, because the force needed is just for driving the servo surface instead of the whole blade. Average collective values for the servo-flap range from -6 degrees to 10 degrees (i.e., trailing edge up) depending on the gross weight of the vehicle, and cyclic values can also range from  $\pm 5$  degrees to  $\pm 10$  degrees.

The **active rotor blade trailing edge flap** is driven via a piezo-induced bending-torsion composite beam. The advantage of this design compared with a system using mechanical linkages is that this does not need a swashplate system and can lead to weight savings. Based on current technology, trailing edge flaps driven by piezostacks can achieve  $\pm 8$  degrees deflection.

Another concept is that of the **all-moving tip** driven by smart materials. The blade tip is actively pitched via a piezo-driven bending-torsion coupled actuator beam that runs down the length of the blade. A quasi-static blade tip deflection of  $\pm 1.8$ deg was measured with 125 Vrms at 15 Hz for a Mach-scaled rotor (2000 RPM). It is estimated that in hover the dynamic blade-tip pitch amplitude will be  $\pm 1.75$  deg below 2/rev and increase up to 5/rev, taking advantage of the actuator torsion mode at 5.7/rev. The 1/rev actuation force can reach as high as 10 percent of the total thrust of the rotor.

**Shaft tilt** can also be used as a scheme for longitudinal and lateral control. An example of this is shown to the left in Fig. 13.2. The powerplant and the transmission part are integrated together and are held by a frame. This frame is supported at the bottom by a universal joint. The top of the frame is driven by four electric servos to position the shaft in any orientation in space. The servos are fixed on the fuselage.

SECTION A-A (YAW ACTUATION DETAIL)

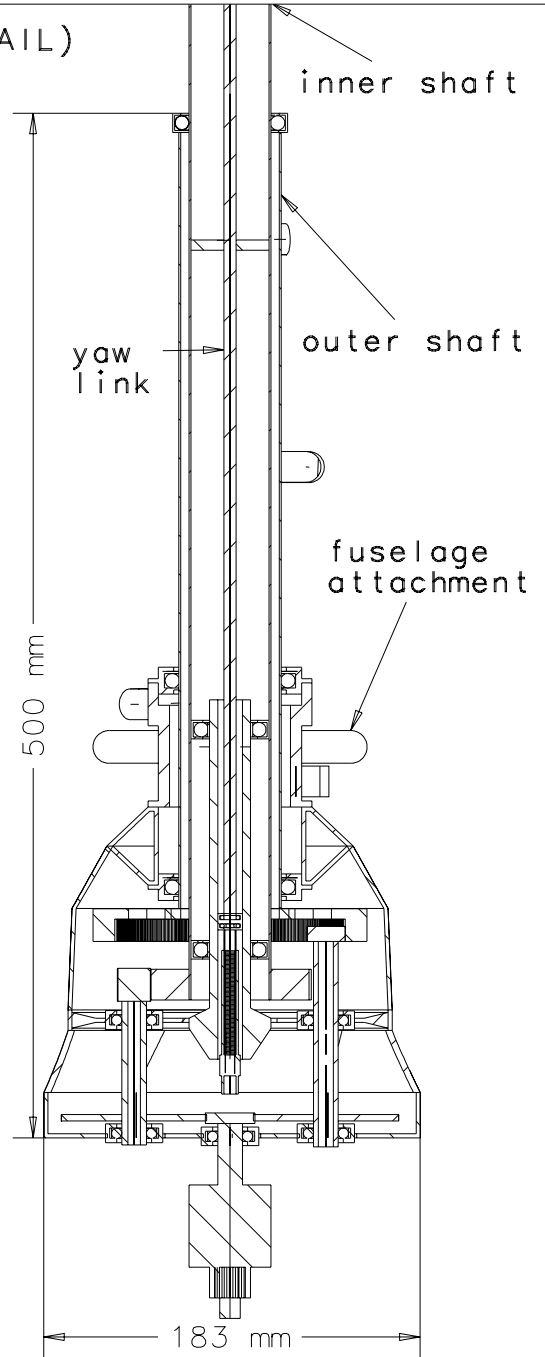


yaw bearing

actuating screw

yaw slide

yaw actuator location



inner shaft

outer shaft

yaw link

fuselage attachment

500 mm

183 mm

outer shaft gear (inner teeth)

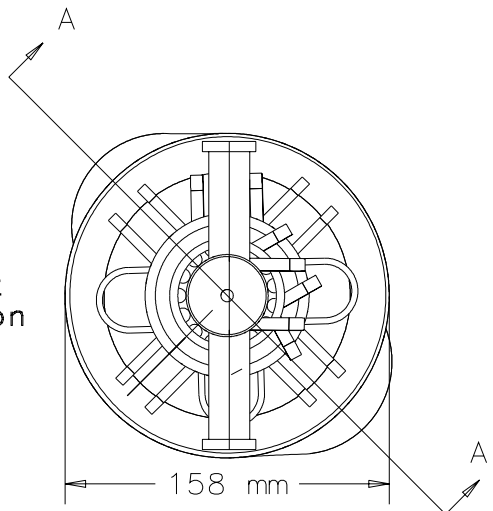
inner shaft gear

inner shaft transmission gear

outer shaft transmission gear

transmission input

SECTION A-A (GEAR BOX DETAIL)



158 mm

TOP VIEW OF TRANSMISSION

SECTION A-A

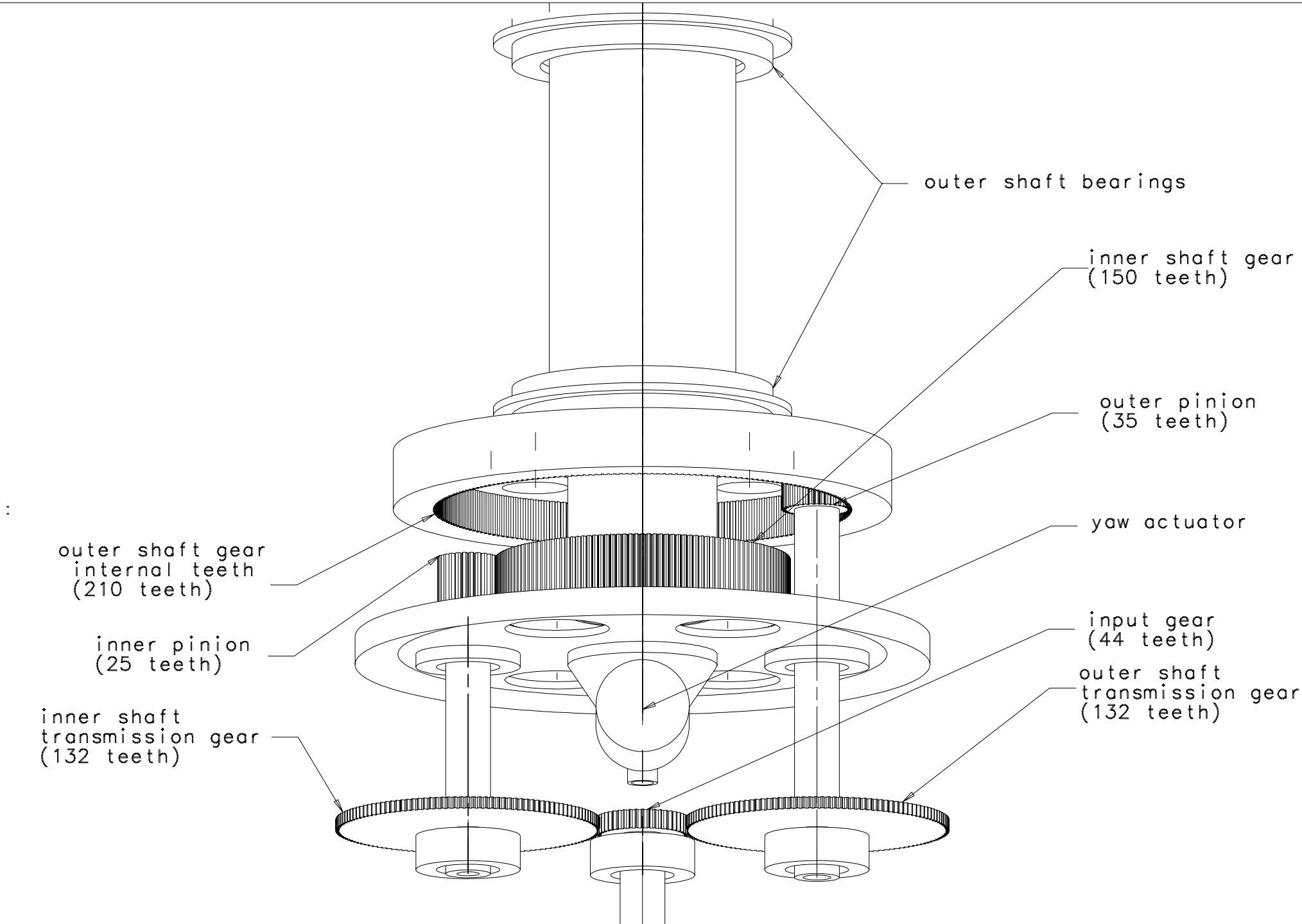




Figure 13.2: Control by shaft tilt and CG shift

Another possible method of controlling the helicopter is through **center of gravity movement**. This is illustrated to the right in Fig. 13.2. The two masses are moved by electric servos and thus change the position of the center of gravity, thereby obtaining lateral and longitudinal control of the vehicle.

Finally, there is the **conventional swashplate** control for a coaxial helicopter. The two swashplates of a coaxial helicopter are connected to each other by linkages which make them move simultaneously in space. The disadvantage of this method is that because it has more parts, it is heavier than the others.

### 13.1 Trade-off study

To make our choice, each of these concepts were considered and compared. First, we considered the servo-flap concept. The biggest problem with this design is based on the low atmospheric density on Mars. The Reynolds number is very low which makes the boundary layer very thick. This means that the trailing edge flap may not be able to create any controlling force since it may be submerged in the boundary layer. If we place the flap with some clearance behind the trailing edge, the pitch moment needed to hold the flap will increase. This will increase the weight of the bearings and make the design interior of the blade complex. Thus we did not proceed with this design.

The moving tip driven by smart materials was an attractive concept. However, we have to fold the blade to fit the vehicle in the lander, and it would be difficult to fold the bending-torsional coupling beam. Also, the load at the tip of the blade is small and this may lead to insufficient control authority.

Shaft tilt is very attractive in the sense that it does not need any swashplate and the associated linkages. However, it can only provide the longitudinal and lateral control. For the collective control, we need to change the RPM of the powerplant. Also it can not achieve yaw control.

The scheme for control of the vehicle with CG shift also can't provide the collective and yaw control we need in our design, and so this method is also rejected.

### 13.2 Control system design

The accomplishment of the collective and cyclic control for the coaxial configuration is very much like that of the single main rotor helicopter. The two swashplates are connected by linkages which make them have the same orientation in space. So for both collective and cyclic control, the two rotors will behave as one.

We have designed an innovative scheme for yaw control, which is shown in Fig. 13.3. The yaw control is coupled with the collective control. The top lever AA' is connected with the linkage of the yaw control at point

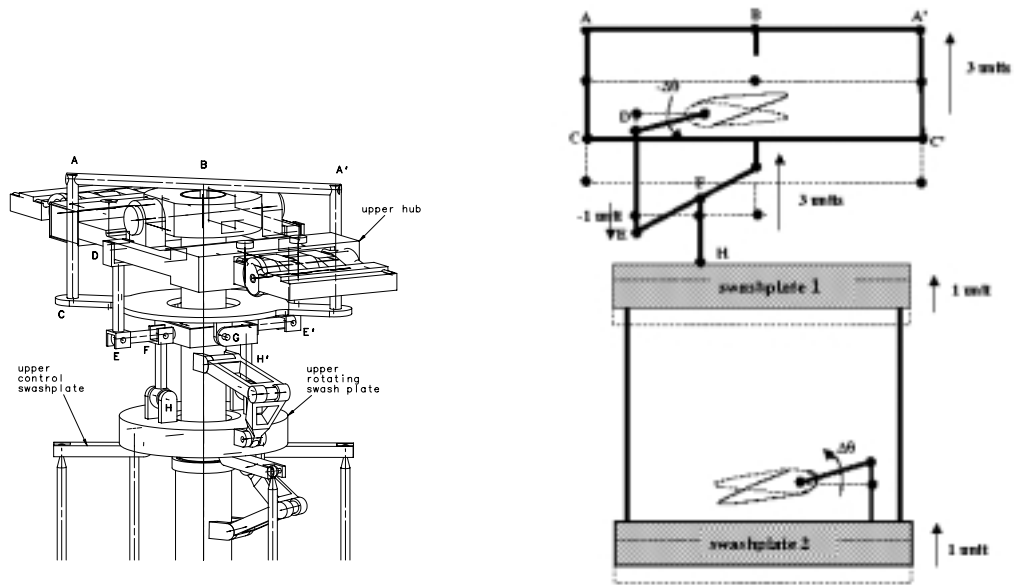


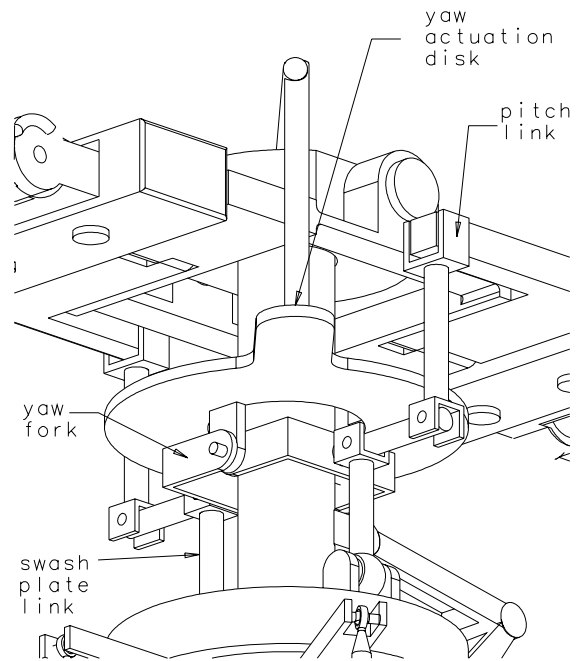
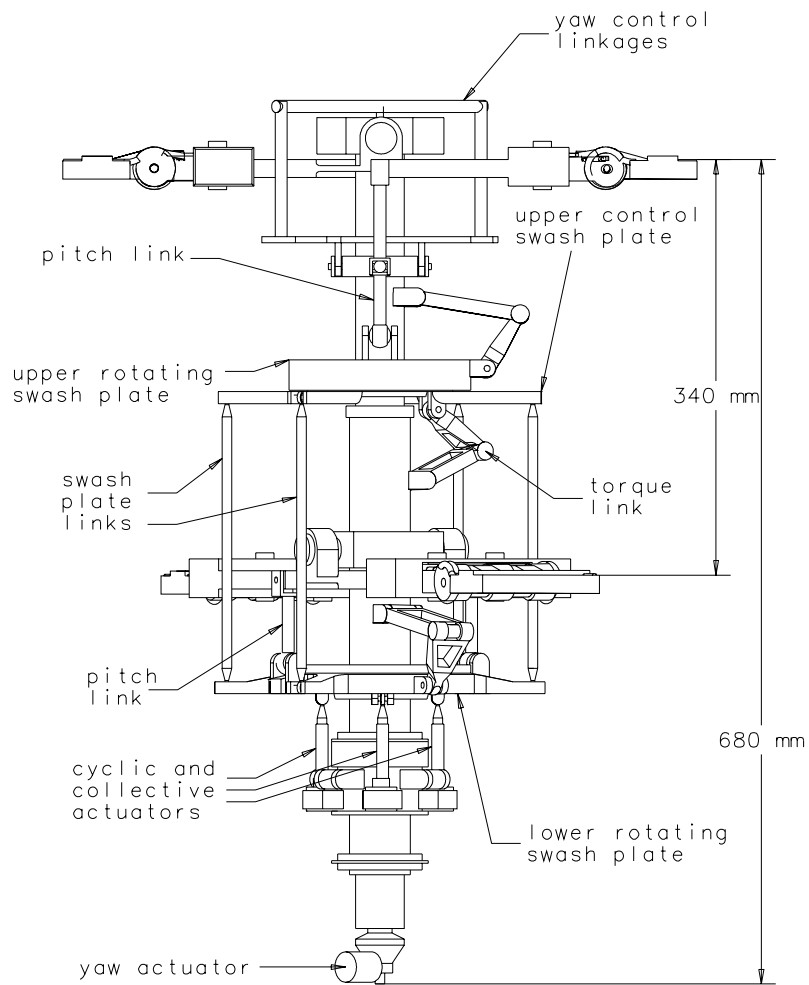
Figure 13.3: Yaw control system

B. Lever AA' is connected with the disk CC' between the lever AA' and the swashplate by linkage AC and AC'. Notice the two forks EG and E'G. One end of these two forks is connected to the disk at point G. The other end is connected with the pitchhorn by pitchlink DE at point E. The center of the fork is connected to the swashplate by linkage FH at point F.

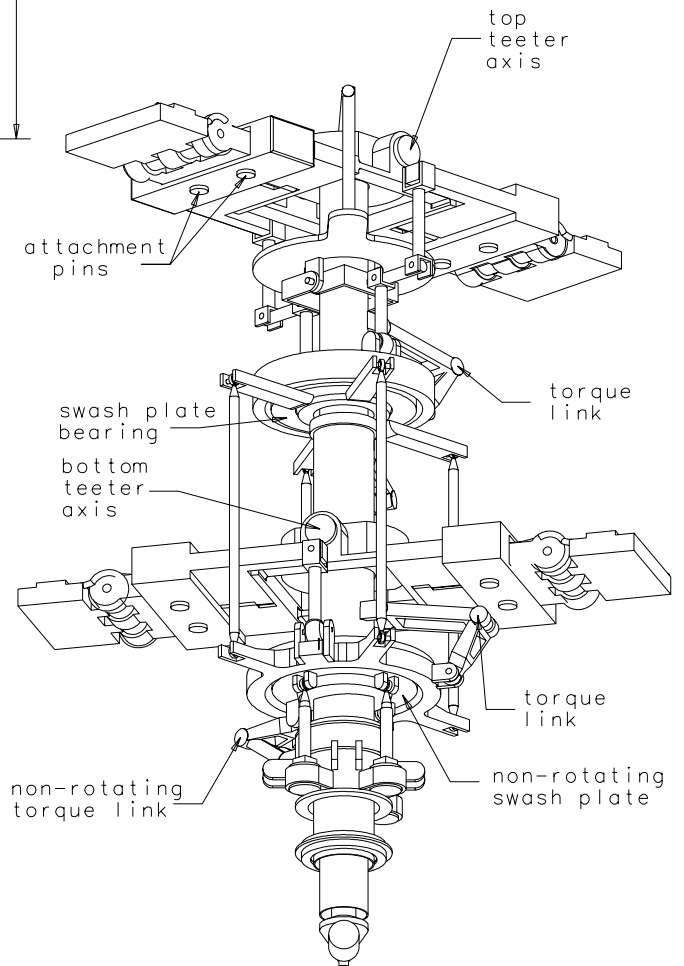
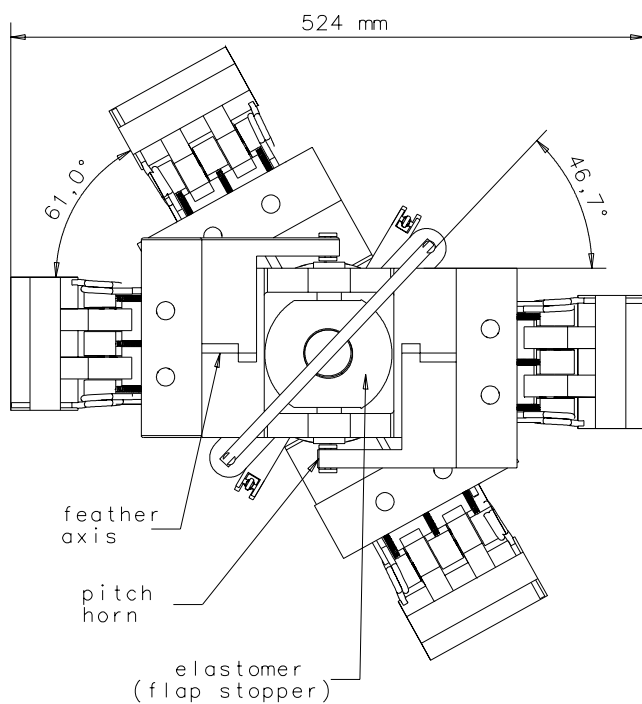
When the collective control is applied, the rod which goes through the inner shaft and is connected with the lever AA' at point B is moved with the same displacement as the collective input by an electric servo motor which is installed in the gearbox. When the lever AA' and the swashplate have the same vertical movement, the two forks stay in the same position. The top and bottom rotors will have the same amount of pitch change.

When the yaw control is applied, the rod which drives the lever AA' has three times the input of the collective control input. For example, when the collective servo gives the bottom swashplate a one unit upward movement, the lever AA' will have a three unit upward movement. When the bottom swashplate has a one unit upward movement, the pitch angle of the bottom rotor will increase a certain degree, say,  $\phi$ . At the same time, the top swashplate will also move upward one unit because the top and bottom swashplates are connected. When the swashplate moves up one unit, the linkage of FH will also move up one unit. This means the center of the fork F will move up one unit. When the lever AA' moves up by three units, the disk will also move up three units by the linkages of AC and A'C'. The end of the fork which is connected with the disk will also move up three units. The other end of the fork E will move downward one unit compared with the original position. The movement relations are shown more clearly to the right in Fig. 13.3.

Thus the top rotor will have the same pitch angle change as the bottom rotor but in the opposite direction. Therefore one rotor will increase the thrust while the other will decrease the thrust. Since the changes are equal, the total thrust will stay the same. Since the torque on one rotor is higher than the other, the vehicle will change direction.



YAW CONTROL DETAIL



## 14 LANDING GEAR DESIGN

In this section we discuss the detailed design of the landing gear. The design is based on our knowledge of the Martian surface from Viking and Pathfinder missions. The landing gear is designed to satisfy FAR 27 requirements. These requirements, as well as those unique to this design, are:

- “The helicopter should be able to be landed with no excessive vertical acceleration, no tendency to bounce, nose over, and without exceptionally favorable conditions” (FAR 27.75) [49].
- Previous Martian surface missions (Viking I, Viking II and Pathfinder) have revealed a very rocky surface (Fig. 14.1). The landing gear must be designed for varying surface conditions, such as protuberances, depressions, small craters, slopes, and soil-bearing strength.
- The landing gear must be retractable to fit inside the lander.
- Finally, the landing system must be lightweight, simple and reliable.

Fig. 14.1 is an image acquired at the Viking Lander 2 site. The rounded rock in the center foreground is about 20 cm wide. The angular rock to the right and further back than the rounded rock is about 1.5 m across [50].

Based on these requirements, a deployable, four legged landing gear is selected. It is simple and lightweight (Fig. 14.2). Each leg ends with an articulated foot pad containing crushable aluminum honeycomb. Due to expected rough surface conditions, wheels cannot be used. The wheels would be required to climb over rocks as large as 1m in diameter (Fig. 14.1). This would introduce a prohibitive weight penalty. Since our deployment scheme does not require movement of the vehicle out of the lander, simple foot pads are the optimal solution.

The foot pads (110 mm diameter) are articulated to allow the vehicle to adapt to slopes and rocks. Their saucerlike shape is designed to decrease stress on impact and avoid instability on touchdown due to soil erosion.

Ground resonance is not a problem in that our rotors are stiff inplane with a lag frequency of 3.7/rev.

To achieve the necessary stability, the landing gear is able to absorb a diversity of impact loads. The tendency to bounce is avoided by using crushable honeycomb material in the foot pads, so the gears would compress on impact. Honeycomb shock absorbers are simple. For lesser number of landings, complex hydraulic shock absorbers can be avoided. Our baseline mission incorporates two landings. In case the mission is modified to allow more takeoffs and landings (for example by using a rechargeable battery instead of fuel cell system), shock absorption can be achieved using pneumatic shock absorbers. Another possibility is to use high performance shock absorbing material like Sorbothane [51] on the foot pads. They must be heated to around  $-20^{\circ}C$ . Crushable honeycomb has been used successfully in past surface missions [52], hence it has been chosen for the MARV foot pads.

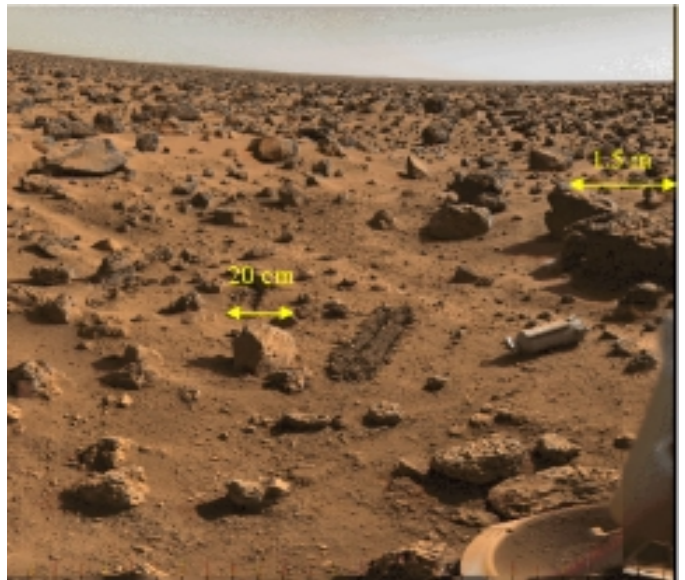


Figure 14.1: Viking image of the Martian surface

## 14.1 Landing leg deployment mechanism design

The extended legs represent a large volume fraction of the vehicle (about 42% for each leg) in order to adapt to as many landing situations as possible. The retraction ratio must be as large as possible to fit the helicopter inside the lander. The folding linkage design achieves a retraction ratio of almost 80%.

The folding linkages consist of three articulated leg sections retracting along the fuselage, as shown in Figs. 14.2 and 14.3. Each leg consists of two parts: one primary strut, articulated around a hinge for retraction, and 2 secondary struts attached to two contiguous sides of the fuselage. The folding hinge on the primary strut is equipped with a torsion spring. In the retracted position the spring is compressed: the folded primary strut is held vertical by a flexible link to the fuselage (Fig. 14.3). When the link is released, the spring extends the two parts of the primary strut in a colinear position. In this position the two parts lock together with a pawl latch as shown in Fig. 14.3.

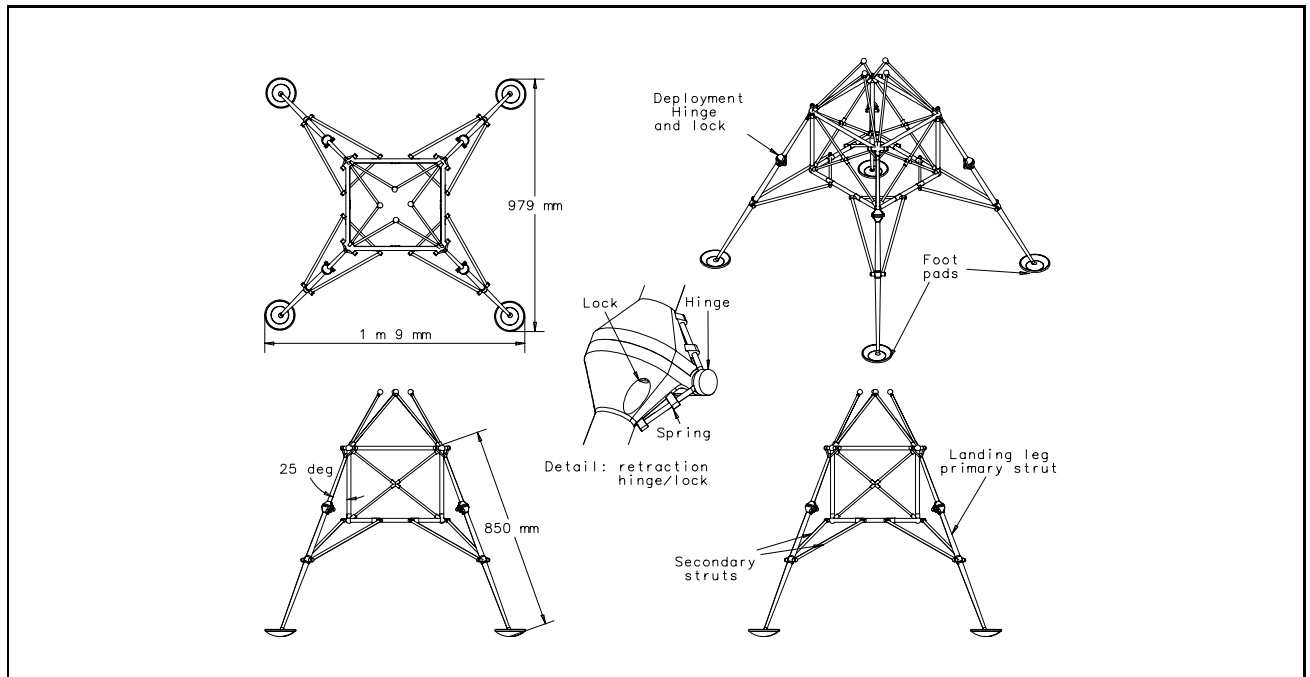


Figure 14.2: Fully deployed landing gear system

## 14.2 Landing gear sizing

In order to choose the best structure for impact absorption and stability upon landing, as well as the most suitable folding linkages, an algorithm was developed to determine the worst combination of impact conditions. The design space was determined and the design was optimized for lowest weight and highest retraction ratio. Three cases can arise during touchdown:

- All legs contact the ground simultaneously: best case both for stability and loading.
- Two legs contact the ground first, and the other two legs are just clear of the ground: worst case for stability (shortest distance from ground contact to center of gravity).
- Only one leg contacts the ground first and supports the totality of the load: worst case for loading.

In all cases the rotor lift is assumed to act through the center of gravity throughout the landing impact. This

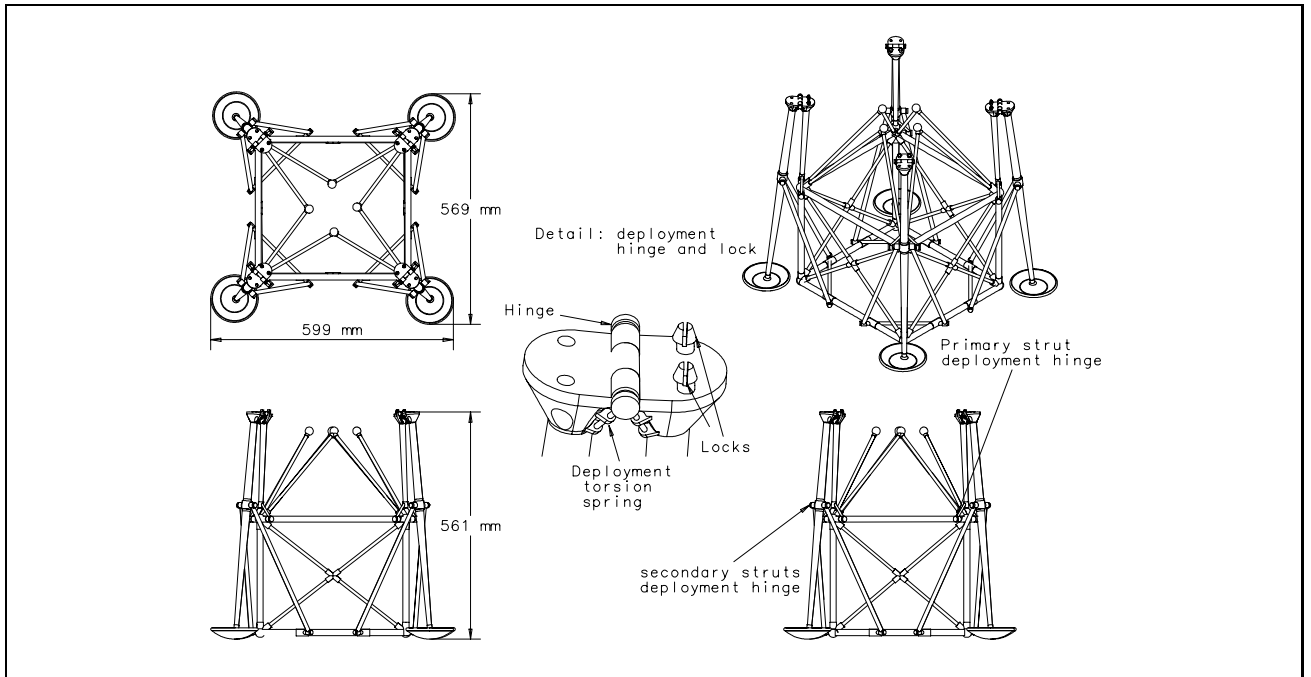


Figure 14.3: Fully retracted landing gear system

lift equals two-thirds of the design maximum weight, as per FAR. A maximum reaction factor of 3 has been assumed for landing leg sizing, with a factor of safety of 1.5. The size of the landing legs is determined by the FAR 29.725 requirement stating that the vehicle should withstand a drop test of 8 in, with a 1.5 safety factor. This corresponds to a drop velocity on Mars of 1.5 m/sec (4.9 ft/sec). Each leg is designed to sustain this drop test without permanent deformation. The primary strut section area increases from the foot pad ( $80\text{mm}^2$ ) to the secondary strut attachment ( $315\text{mm}^2$ ), where the bending stress is highest. The section area then decreases from this point to the attachment to the fuselage corner. The secondary struts work only in tension and have a constant circular cross section ( $80\text{mm}^2$ ).

Fig. 14.5 shows the region of possible design. The parameters are the landing gear length and angle as defined in Fig. 14.2. The conditions for unacceptable landing are as shown in Fig. 14.4:

**Case 1:** Contact of the lower blades with the ground, while landing at a  $15^\circ$  inclination. For this condition the blade maximum flapping is assumed, as is the presence of a rock of maximum diameter.

**Case 2:** Vehicle turnover while landing at a  $15^\circ$  inclination, in the worst landing condition (two legs contact the ground first, the two other legs just clear of the ground).

**Case 3:** Contact between the lower rotor blades and ground or vehicle turnover (**case 4**) when one leg first contacts a rock of maximum diameter.

**Case 5:** Contact between ground and lowest part of fuselage (considering the additional area for payload installation, and the presence of a maximum diameter rock).

Note: Case 6 in Fig. 14.5 corresponds to a non-feasible region (landing gear height in extended position less than fuselage height).

The point selected for MARV corresponds to the optimal weight and retraction ratio: landing leg length of 850 mm, angle from the vertical axis =  $25^\circ$ , for a weight of 3.6 kg and a retraction ratio of 79%.

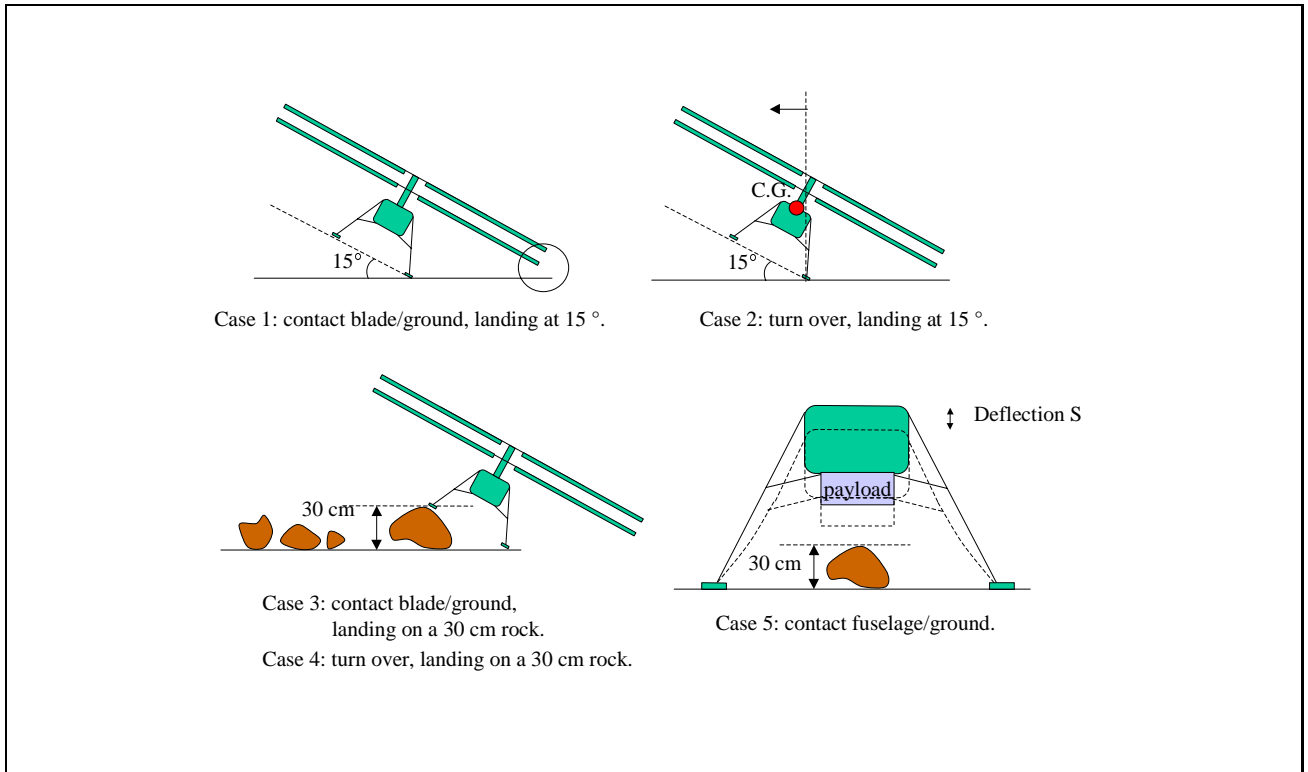


Figure 14.4: Different landing cases considered for leg sizing

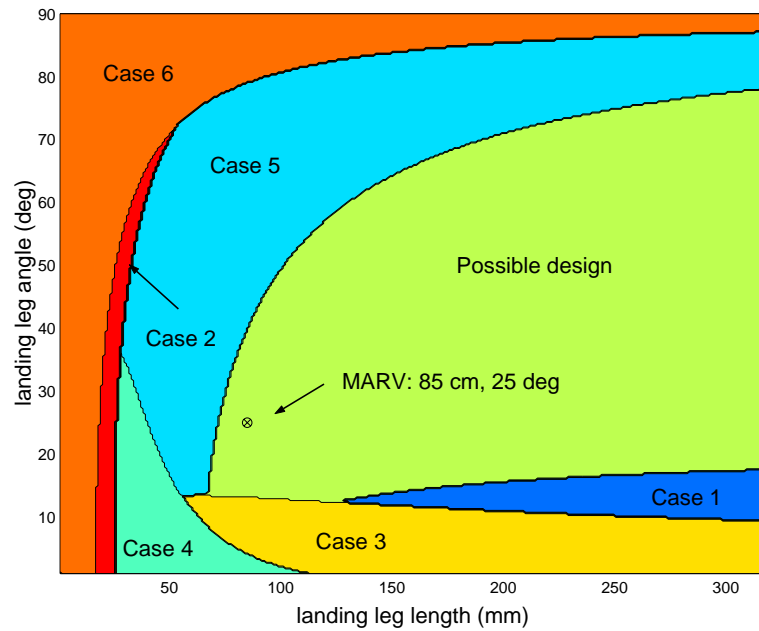


Figure 14.5: Design space for a four legged system

### 14.2.1 Trade study

A three legged landing system was first considered. The change to four legs was dictated by the weight versus strength tradeoff that also produced the rectangular shaped body, with its four obvious attachment points. The revised gear pattern also greatly simplified the deployment mechanism by reducing the leg length: the required

leg length increases in case of three legs because of decreased minimum distance between the center of gravity and the landing leg, so the total landing gear weight is lower in case of four legs. For five legs and more, the weight again increases and the retraction ratio is too low. Therefore four legs is the optimal choice for MARV.

## 15 FUSELAGE DESIGN

The fuselage must be able to provide support for the main mechanical parts (gearbox/motor assembly and rotor) and the landing gear; provide support and protection for the fuel systems as well as the avionics and payload; and provide effective load paths to resist landing and an deceleration of  $100m/s^2$  during atmospheric entry as required by the RFP.

The fuselage structure is kept simple and light. The fuselage is the strongest part of the structure, since it has to directly support the loads in flight, as well as during the landing. The central structure is designed as a rigid hexahedral. It consists of two rectangular horizontal frames connected by four vertical struts and supported on each side by two cross struts for torsional stiffness (Fig. 15.1). The junction with the landing gear has been designed to resist the landing impact while still allowing a high retraction ratio.

To reduce the weight as much as possible a thin skin of Mylar was used to cover the fuselage. This skin protects the subsystems from dust, wind and rotor downwash.

Since this helicopter will only fly in the thin Martian atmosphere, we ignore the aerodynamic streamlining demanded by Earth's atmosphere.

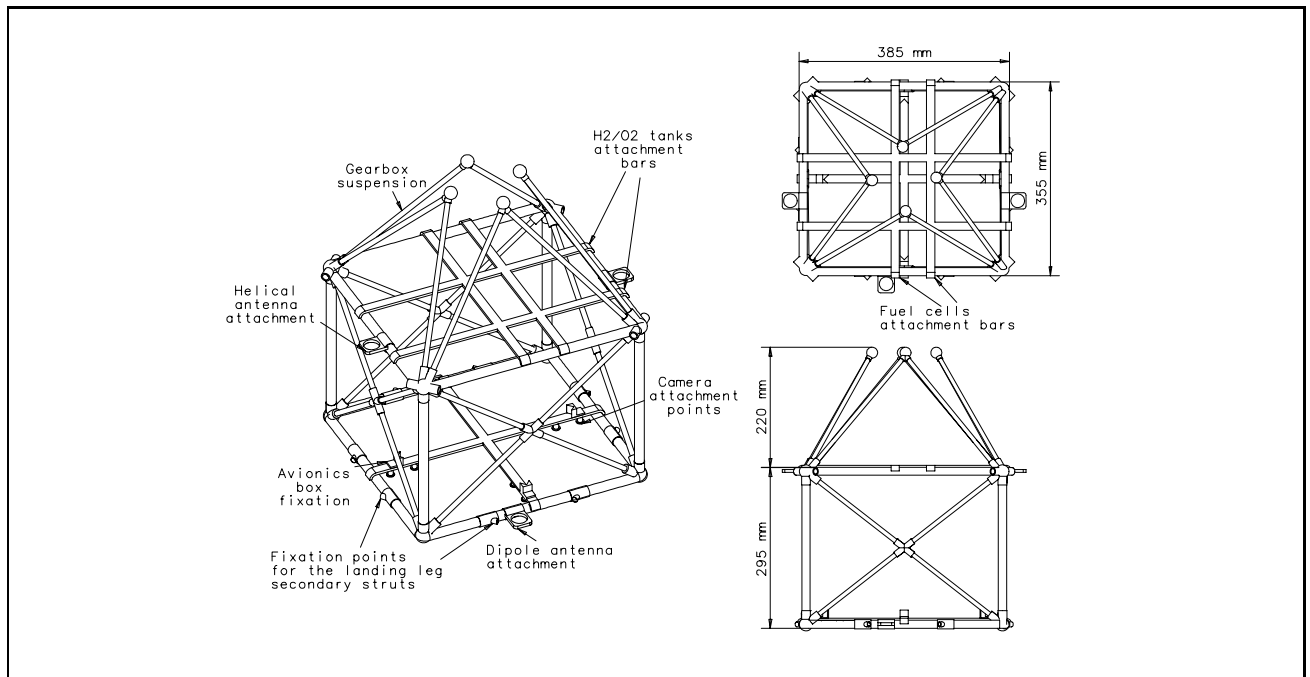


Figure 15.1: Fuselage structure

### 15.1 Internal configuration

Inside the fuselage, the equipment is arranged in two stages: one upper stage for the power system and one lower stage for the avionics and payload.

The structure is basically wrapped around the tanks: if the tanks are enlarged, the vehicle design has to grow to accommodate them. One problem is posed by the use of only two tanks. Since oxidizer is heavier than fuel, four tanks would allow the placement of one tank on each side of the cabin for balance. With only two tanks, proper center of gravity must be maintained. The fuel tank was moved further outboard than the oxidizer, while the fuel cells were moved towards the fuel tank. The fuel, oxidizer, and water circuits are so arranged that the center of gravity is exactly placed on the shaft axis.

The avionics box, protected by an aerogel coverage, is fixed to the bottom of the fuselage by two transversal bars attached to the lower frame.

Since the payload can be of many types, no fixed payload bay is designed, but a space is kept under the avionic box (150 mm x 350 mm x 360 mm) and four attachment points are provided on the lower frame. This would, for example, allow fixation of an articulated arm and a container for a sample return mission. Additional space is also available in the upper stage, under the fuel and oxidizer tanks, to accommodate scientific payload, inside a box similar to the avionics box.

## 15.2 Gearbox suspension

The gearbox supports the rotor mast. A rigid fixation of the gearbox to the frame would transmit rotor vibrations directly to the structure.

The remedy consists of placing between the gearbox and the structure a flexible suspension which damps out the main part of vibrations. Thus this system acts like a filter for vibrations. The gearbox is finally attached to the structure at two levels (Fig. 15.2):

- at the rotor mast level by 4 rigid bars, transmitting the rotor lift to the structure (each bar is doubled to insure torsional strength).
- at the gearbox level by a flexible suspension, placed between the bottom of the gearbox-motor assembly. This suspension takes care of the loads in longitudinal and lateral directions as well as pitching and rolling moments and the reaction couple from the motor.

Suspended like a pendulum, the gearbox oscillates around the meeting point of the 8 fixation bars.

The principal part of the flexible suspension is a cylindrical element formed by a succession of thin disks of rubber and duralumin, as shown in Fig. 14.4. One face of each element (there are four elements in total) is bonded to the gearbox, while the other is bonded to the structure. The vibration absorption occurs in the radial direction of the element, deformed in shear. The reaction couple transmission is achieved by compression of the elements. Two such elements receive in shear the loads in the longitudinal direction. The two other elements receive in shear the loads in the lateral axis. The reaction couple from the motor is taken in compression by all four elements. A transversal bar associates the two element groups. This part works only in traction/compression. The elastomeric material used in this system is maintained at a temperature of  $-30^{\circ}C$  using the waste heat from the fuel cells which are located just above the fixation beam to the fuselage. Although Silicone has the best overall temperature range of any elastomer (down to  $-150^{\circ}F \approx -100^{\circ}C$ ), it cannot be used because of poor tensile strength and tear. We recommend using Neoprene rubber which has good properties down to  $-65^{\circ}F (\approx -54^{\circ}C)$ . This vibration absorption device is designed to cancel the inplane vibrations induced by the high lag frequency.

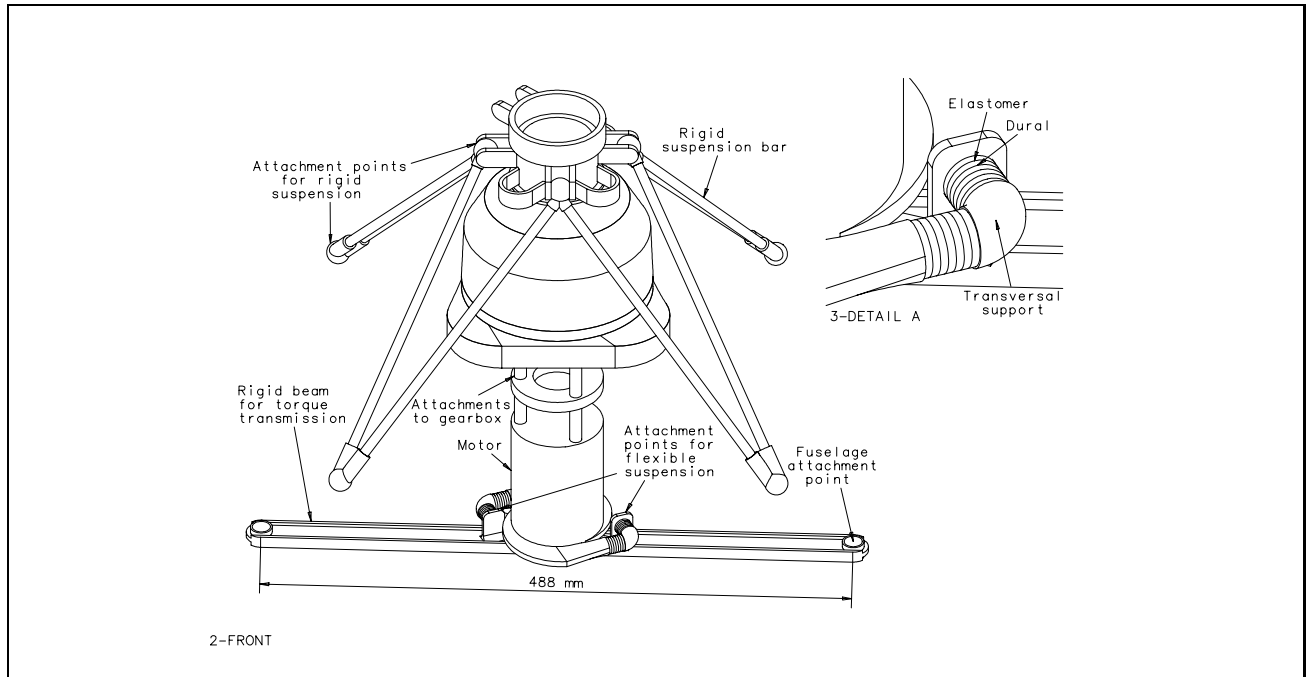


Figure 15.2: Gearbox suspension

## 16 MATERIALS AND MANUFACTURING

The structures of MARV must be built of solid materials which can survive the harsh Martian environment. As stated in the RFP, the year-round variation of Martian temperature is from  $-132.6^{\circ}\text{C}$  to  $17.4^{\circ}\text{C}$ , and the average temperature is  $-62.6^{\circ}\text{C}$ . In the early Martian fall season, the diurnal temperature variations are about  $0^{\circ}\text{C}$  (at noon) to about  $-100^{\circ}\text{C}$  (at night). This represents a large variation in temperature.

The atmosphere of Mars consists of 95.32% carbon dioxide, 0.13% oxygen, 0.03% water and small concentrations of other elements. One advantage of this dry and practically oxygen-free atmosphere is that materials on Mars are not corroded.

Hence, a key problem in the selection of materials is low temperature behavior.

### 16.1 Properties of aerospace materials at low temperatures

For the design of aerospace vehicles, one important criterion is weight, and therefore materials with high strength/weight and stiffness/weight ratios are widely used. These include metallic alloys, such as aluminium and titanium alloys, and different kinds of composite materials. These materials have been successfully applied to fixed-wing aircraft, rotorcraft and Earth-orbit spacecraft. However, for most of these applications, there are no severe temperature challenges. Therefore, for low temperature applications, the change in mechanical properties of conventional aerospace materials should be considered.

O'Brien and Cleary [53] tested an aluminum-lithium (Al-Li) 8090 alloy over the temperature range  $-50^{\circ}\text{C}$  to  $110^{\circ}\text{C}$ . Three mechanical properties – tensile strength, fracture toughness and fatigue crack growth behavior – were tested. They found that in this range, temperature had little influence on these properties. For example, one result from their test is shown in Fig. 16.1. LT, TL and ST represent different test orientations.

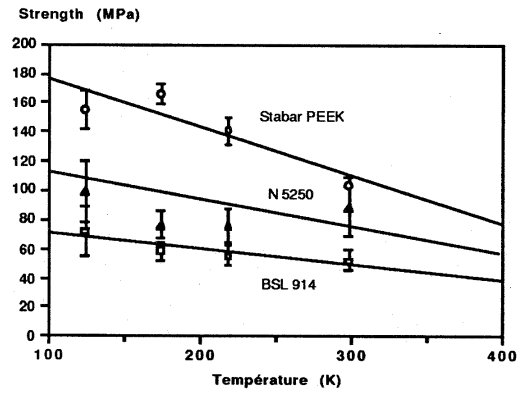
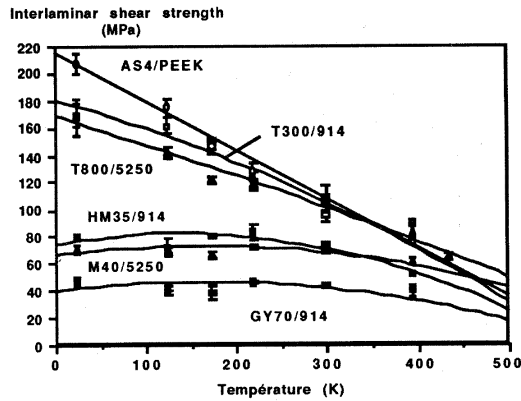


Figure 16.2: Interlaminar shear strength and matrix strength versus temperature

Stevenson [43] tested the rover wheel with a core of black anodized aluminum alloy (7075-T6) for the Mars Pathfinder Rover. The legs of the Mars Surveyor 98 Lander also were made of aluminum [54]. Aluminum alloy has therefore been proven on Mars. Miller [55] listed the tensile strength of glass fiber at different temperatures. Some fibers became stronger when the temperature decreased. For example, the tensile strength of E-glass is  $5310\text{MPa}$  at  $-190^{\circ}\text{C}$ , while it is  $3445\text{MPa}$  at  $23^{\circ}\text{C}$ . Roussy and Parcelier [56] examined the effect of various parameters at different temperatures (from  $-253^{\circ}\text{C}$  to  $127^{\circ}\text{C}$ ) on the mechanical properties of thermoset (cyanate, epoxy, bismaleimide, polyimide) and thermoplastic (PEEK) composite materials. Some of the experimental results are shown in Fig. 16.2. It is seen that the ultimate strength of various composite materials increases when the temperature is lowered from 400K to 20K. However, the amount of the increase depends on the type of fiber used.

The effect of low temperature on the matrix is an increase in stiffness and an improved toughness. This is shown by the measurements of tensile strength in Fig. 16.2. At low temperatures, some specific failure modes of composite materials should be analyzed. One example is the possibility of a laminate cracking due to a large temperature differential between the curing temperature and the low operational temperature.

In general, materials used on Earth can also be used on Mars.

The mechanical properties of some example materials are listed in Tables 16.1 and 16.2. It should be noted that for composite materials different processes for lay-up of the plies bring different properties.

## 16.2 Materials for primary structures

Our choice of materials for primary structures has depended on high strength/weight and stiffness/weight ratios.

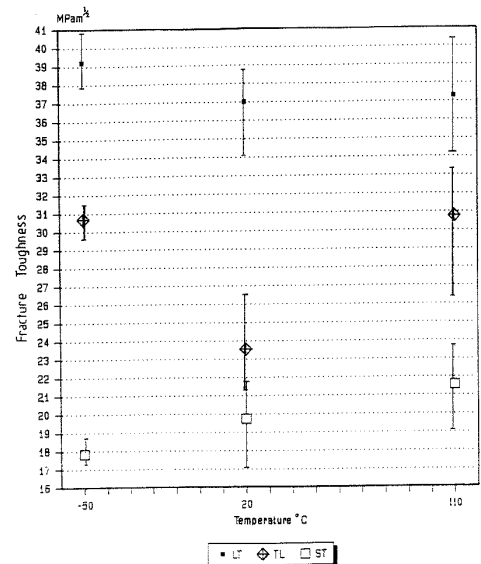


Figure 16.1: Average and range of fracture toughness values for three test orientations

Material	Density, $\rho$ ( $kg/m^3$ )	Ultimate Strength (Tension) $\sigma_U (MPa)$	Yield Strength (Tension) $\sigma_Y (MPa)$	Modulus of Elasticity $E (GPa)$	$\sigma_U/\rho$	$\sigma_Y/\rho$	$E/\rho$
Al(7075-T6)	2800	570	500	72	0.204	0.179	25.7
Al-Li(8090)	2530	475	350	80	0.188	0.138	31.6
Ti6Al4V	4730	900	830	115	0.190	0.175	24.3

Table 16.1: Typical properties for some metallic alloys

Material	Density, $\rho$ ( $kg/m^3$ )	Tension Strength $\sigma_T$ $0^\circ/90^\circ$	Tension Modulus $E_T$ $0^\circ/90^\circ$	Compression Strength $\sigma_C$ - $0^\circ$	Compression Modulus $E_C$ - $0^\circ$	$\sigma_T/\rho$ $0^\circ$	$E/\rho$ $0^\circ$
AS Graphite-Epoxy	1540	1448/62	128/9	1172	110	0.940	82.5
Boron-Epoxy	1990	1585/63	207/19	2482	221	0.796	79.6
E Glass-Epoxy	1800	1130/97	39/5	620	32	0.628	21.7
Kevlar49-Epoxy	1380	1379/28	76/6	276	76	0.999	55.1

Table 16.2: Typical properties for some composites

**Rotor blades:** nose box – graphite/epoxy (AS graphite/epoxy); I-beam rib – graphite/epoxy and honeycomb (Nomex); skin – Mylar film; flexible beam – E-glass/epoxy

**Transmission / Rotor Control System:** shaft – Ti6Al4V; gear – steel; link rod – graphite/epoxy tube; swashplate – Al-Li 8089; swashplate ball – 7075-T6 overlaid nickel

**Fuselage:** – graphite/epoxy

**Landing Leg:** – graphite/epoxy

## 16.3 Manufacturing

Manufacturing is an important step in making the design become a reality. In order to produce the most cost effective product, most parts of our rotorcraft were designed with conventional structures. However, to meet the requirements of the Martian environment, some parts such as blades, had to be specially designed. Nevertheless, simplicity of manufacture was emphasized in the design.

Use of information technologies, including CAD, CAE, CADAM, and electronic document tracking and optimizers in building jigs, molds and other parts will reduce the cost of the rotorcraft.

**3D Electronic Mockup:** Use of a three-dimensional (3D) Computer Aided Design (CAD) system is recommended for the drawings. This will involve an electronic mockup. The electronic mockup provides a means to check-fit assemblies before they are built [57]. It is a powerful tool to resolve potentially costly design conflicts.

**Jigs:** Three jigs are needed to build up our rotorcraft: a blade jig, a jig for the transmission and electrical motors, and a final assembly jig. The latter holds the fuselage in proper alignment to enable the other subsystems to be attached. Each subsystem of the MARV should be inspected carefully before final assembly.

**Manufacture of blades:** The rotor blades have optimized planform, taper and twist, and have hinges for folding. The structural details are shown the blade structural design section. All blades are of composite

construction. The blade consist of a nose box (D-spar), ribs (I-beam) and a trailing edge block. The part aft of the nose box is covered by Mylar film.

For folding, each blade is divided into two sections which are hinged together. The fabrication of each section includes three major cure cycles. The nose box, the ribs and the trailing edge block are laid-up and cured separately. Then these three parts are bonded together to get the blade shape. Three kinds of mold are used: the nose box molds, the rib molds, and the trailing edge block molds.

Molds can be also designed using a 3D CAD system. Using 3D CAD technology, the design can be easily transferred from drawings to computer controlled machines to build the high quality molds. Thus the accurate reproduction of the shapes of different parts of the blade can be ensured.

Since the mold is heated and pressurized, the choice of mold material becomes key in mold fabrication. The material should have dimensional stability and compatibility, low cost, good surface finish, and durability. Our molds are machined from tool steel and coated by nickel. The coefficient of thermal expansion (CTE) of tool steel is  $11.1 * 10^{-6}/^{\circ}C$  [58]. Among the metal materials, it most closely matches that of composites, such as glass fiber-reinforced materials, which have CTEs of  $6.3 - 8.4 * 10^{-6}/^{\circ}C$ . Steel is also highly durable and has good thermal conductivity.

Before curing, release agents are used to coat the molds so that the composite parts can be demolded easily. A computer-controlled ply lay-up machine is used to accurately place the graphite/epoxy cloth, cut cloth to the proper length and width, lay it at the correct angle, and compact each ply directly on the mold surface of different parts as it is being laid. After the plies are stacked, the outside of the parts is covered by vacuum bags. Then different parts are cured separately using an autoclave. The primary component of the autoclave is the pressure vessel, which contains embedded heaters and cooling coils. The autoclave applies pressure to the outer surface of the composite parts through pressurization of the interior gases.

The curing process of the nose box includes two steps. First, four sections of the nose box (01, 12, 23 and 34, as shown in Fig. 6.2) and two I-beam sections (11' and 22') are cured. However, in this step, the plies are only laid-up to half of the thickness for all parts. After curing, two nose box sections are bonded to one I-beam section to get an assembly. Then the lay-up machine is used again to place the plies on the surface of the assembly to the required thickness. Cured again, the nose box attached with one I-beam rib is built for each blade section. The other ribs and the trailing edge block are cured once.

All parts are put in the blade jig. Using this jig, each part can be positioned exactly. The nose box, ribs and trailing edge block are bonded together. The Mylar film is then stretched to cover the top and bottom surfaces of the blades and is glued to the ribs. Finally, two blade sections are connected by a hinge to form the complete blade.

After final assembly, each blade is inspected to confirm the accuracy of planform and airfoil shape, and the quality of bonding. Before installation on the hub, each blade is statically and dynamically balanced.

## 17 AVIONICS SELECTION

During the mission, avionics are responsible for (i) monitoring and sequencing the internal systems, (ii) maintaining communication with the lander, and (iii) navigation. RFP section 1.2.6 states that avionics may be assumed to be no more than 10% of the vehicle mass. This assumption would reduce the avionics system to a 'black box' of 5 kg mass for a 50 kg helicopter. A lower-weight avionics suite is presented here, which totals approximately 4 kg. This 20% weight savings translates into additional scientific payload capacity.

The following sections describe the components of the suggested avionics package. Realistic weight estimates

have been made based on systems available today. Although specific brands are suggested, different brands may be suitable as well.

## 17.1 Outboard avionics

The responsibility of the outboard avionics is to measure the atmospheric conditions around the helicopter, and to input these into the flight computer. Pressure transducers will serve as the pitot-static system of the helicopter, and will aid the flight computer in determining altitude, rate of climb, and flight speed. Temperature sensors will be used to monitor the changing atmospheric conditions. Finally, cameras record the views of Mars seen by the helicopter.

**Pressure transducers** can be used to measure the static pressure, from which altitude and rate of climb can be determined, and from total and static pressures, flight speed is determined. Course and speed corrections will be made autonomously, based on this data. Two transducers will be mounted facing forward, to measure total pressure. One transducer will be mounted on each of the port and starboard sides, to measure static pressure. With two transducers to measure static and total pressures, there is sufficient redundancy.

The pressure transducer emits electrical pulses corresponding to the pressure. These pulses are output to the flight computer, which processes the data and performs the altitude, climb rate, and flight speed calculations. Industrial supply catalogs/literature (e.g. Omega [59]) present a wide array of pressure transducers available, which are capable of measuring the expected range of pressures on Mars. It is estimated that a pressure transducer with a weight of 0.057 kg can be achieved, in a small package of roughly 30 mm x 20 mm diameter.

The ambient temperature will be monitored by three **temperature probes**. Conditions will be carefully noted so that the delicate operating conditions are not exceeded. If temperature conditions become dangerous, the mission should be delayed or aborted if in-flight. Such safety routines can be pre-programmed into the flight computer.

Probe size/weight was estimated from the Cole/Parmer catalog. The probes themselves will be wired into the temperature sensor portion of the flight/data computer, which will monitor the temperature. It is estimated that a temperature probe with a weight of 0.012 kg can be achieved, in a small package of roughly 100 mm x 2 mm diameter.

**Cameras** can be used with sophisticated shape recognition programs to allow the MARV to recognize landmarks, as a navigation aid. Stereoscopic vision capabilities may enable the helicopter to avoid obstacles, as well as judge distance to a target. Additionally, cameras aid scientists in viewing the actual environment in which the helicopter is operating, avoiding the need to rely simply on pressure and temperature readings. Cameras will likely be involved in the scientific mission, but the package of cameras recommended here is done so solely for the purposes of avionics.

There is a wide variety of cameras available for use on the MARV, including microscopic cameras, weighing less than 20 grams. The Mars Pathfinder mission successfully utilized a panoramic camera which spans a 360-degree viewing area [60]. The Sojourner rover utilized two forward-looking cameras to provide stereoscopic vision



Figure 17.1: Transducers



Figure 17.2: Sony Xc-999

[60]. However, for the purposes of collision avoidance and landmark recognition, we recommend an array of three single, wide field-of-vision cameras with acceptable resolutions. One camera will point forward, and one will point to each side. This will provide a useful level of camera coverage.

The cameras proposed here provide a compromise between size, weight, and resolution. The Sony-XC999 color camera weighs 0.2 kg and is roughly of 120 mm x 22 mm diameter [61].

## 17.2 Inboard avionics

Inboard avionics allow the helicopter to (i) maintain trim and course, (ii) store and transmit data, and (iii) maintain a proper internal environment.

Trim will be maintained by properly measuring the pitch, roll, and yaw attitudes/rates of the helicopter. In addition, rotor RPM must also be monitored. For these two purposes, a set of gyros and a tachometer will be needed.

Three **gyroscopes** will be used to independently measure the rates of pitch, roll, and yaw. There are a number of sophisticated, lightweight gyros available for model helicopters and unmanned air vehicles (UAVs). The Micro Piezo Gyro [62] shown in Fig. 17.3 operates using a piezoelectric crystal rather than a mechanical flywheel. This offers a fast response time and a high accuracy, in a small package. We expect a similar set of gyros can be mounted on our helicopter. The weight of this gyro is 0.014 kg, and its size is roughly 28 mm cube. Three gyros will be used, one for each axis of rotation. It is necessary only that the gyro which determines yaw be placed about the vertical axis. Since no exposure to the atmosphere is required, we will mount the three gyros inside the central avionics box.



Figure 17.3: Mini gyro

Two possible **rotor tachometer** types are optical and magnetic. We recommend the magnetic tachometer, because it is generally a more rugged device and is roughly the same weight as the optical type. Measurements of rotation speed are made through the interaction of the magnetic sensor and several magnetic strips on the rotor shaft. As each strip spins by the sensor, an electrical pulse is generated. Typically 3-5 strips are placed on a small shaft; thus 3-5 pulses emitted from the sensor will equal one revolution. The flight computer uses this data to accurately determine rotor speed. We estimate that a tachometer of 0.09 kg weight and 50 mm x 15 mm diameter can be placed on our helicopter [63].



Figure 17.4: Tachometer

A computerized compass will help the flight computer determine heading relative to the Martian north pole. Distance and bearing from the lander will be determined through the use of a Doppler radar system on the lander. The radar signal will originate from the lander, reflect off the helicopter and return to the lander. The process will determine the distance and bearing between the lander and the helicopter. The position vector, thus determined, can be transmitted to the helicopter. Using this information, the helicopter can decide its course.

The computerized compass will weigh around 0.014 kg, and be sized approximately 5x8x1 cm [61]. Under this Doppler radar setup, there is no required component for the helicopter itself. The only requirement is the ability to receive this passive telemetry data.

Communication/telemetry equipment will be necessary to transfer mission status and scientific data back to the lander (RFP: section 1.2.7). Data will be collected, synchronized, and sent. Three major avionics components – a data multiplexer, a transceiver, and antennas – will perform these tasks. This section will describe these

three components. The feasibility of radio communication on Mars will be examined. Finally, our suggested communications package will be described.

The multitude of sensors and signals will make it impossible to transmit each individually. This problem is overcome by using a digital data multiplexer. This device merges each of these signals into one continuous stream, which is then beamed to the lander. The multiplexer must be chosen on the basis of the number of signals to be processed, and the required accuracy. We estimate that the multiplexer can be designed to be approximately 0.2 kg and approximately 100x100x25 mm in size [64].

Radio communication issues and how they manifest in this mission are now described. The feasibility of communication will be examined, concluding with our suggestion on the transmitter and antenna for our helicopter.

A primary issue behind successful radio communications is the quality of the received signal. If a signal sent from the helicopter is too weak when it reaches the lander, there will be an unacceptable level of data loss. The same is true for a signal sent from the lander to the helicopter.

A further primary issue is that of Line-of-Sight (LOS) contact between the helicopter and the lander. We must rely on LOS operation because Mars is an isolated environment. Neither satellites in orbit, nor repeater stations on the ground are available for communications assistance. Additionally, Mars has no significant ionosphere off of which signals can be bounced. If direct LOS is not maintained, communication signals will not reach their target.

**Quality of Received Signal:** The strength of a received signal depends on several key parameters. First, the signal is given a certain strength when transmitted, through the transmitter and the antennas. These are termed gains, and are beneficial to communication. Second, there are factors which decrease the signal strength as it passes through cables and through the atmosphere. These are termed losses, and are detrimental to communication. It is through proper balance of these that a quality link is designed. Gains and losses can be summed into one simple equation:

$$P_r = P_t - L_p + G_t + G_r - L_t - L_r \text{ [65]}$$

where:

$P_r$  = Signal Power Received  $P_t$  = Transmitter Gain

$L_p$  = Free Space Path Loss  $G_t$  = Transmit Antenna Gain

$G_r$  = Receive Antenna Gain  $L_t$  = Transmit Line Loss

$L_r$  = Receive Line Loss

The most significant parameters here are the path loss and antenna gains. A large path loss, coupled with low antenna gains, results in a very weak signal at the receiver. This very weak signal, as previously mentioned, will be rife with data errors. For our design, we have assumed a value of -80 dB as an acceptable received signal which will have a low bit error rate (BER).

We have also assumed a 5 W transmitted power source, which translates into a transmitter gain of 7 dB. This is limited by the size and weight of the transmitter. We expect a 5 W transmitter can be placed in a small enough package for our helicopter.

Our cable distances can be designed to be very short. In our case we will assume 2 meters total, which will result in a total line loss of 0.5 dB[60].

With these assumptions made, there are 3 parameters remaining which need to be designed. Path loss will depend on distance, frequency, and antenna type. Antenna gain will depend mainly on antenna type.

We must now make our choices. Our first decision is that of frequency. Previous NASA scientific missions

have operated in a wide frequency spectrum, ranging from 1.7 GHz to above 20 GHz. However, we can see that for an omnidirectional antenna, path loss is related to frequency:

$$L_p = 32.4 + 20\log(f) + 20\log(d)dB \text{ [65]}$$

Therefore to minimize path loss, we wish to keep a low frequency. We have chosen 2.4 GHz as our communication frequency. This is a sufficiently low frequency such that path loss is minimized, and it is in a range in which NASA has much experience. NASA's Tracking and Data Relay (TDR) Satellites communicate in this range of frequency [66], and it is also used for many commercial Local Area Networks (LANs).

Our second decision is that of antenna type. We may choose an omnidirectional antenna – specifically, a vertical dipole antenna – or we may choose a directional antenna – most commonly a helical style. They are similar in that they are rugged and small; the difference is that of direction and antenna gain. Omnidirectional antennas do not need to be pointed in any direction to have their signal received. The signal is radiated equally in a spherical pattern. Thus the path loss is high. Directional antennas, in contrast, must be pointed at their target to have their signal received. Such an antenna would require a tracking system and actuators for correct pointing. However, its signal radiating pattern is not spherical, and thus results in low path losses.

Another difference is that the antenna gains related to these two styles are significantly different. Omnidirectional antennas are low-gain antennas, with gains between 0 and 5 dB. Directional antennas, in contrast, can achieve high gains, ranging from 6-30 dB [66].



Figure 17.5: Helical antenna

Based on the requirement that a directional antenna have a tracking system and actuators, initially we favored an omnidirectional transmitter antenna. However, due to the large path loss associated with such an antenna, this type is unfeasible. We can see that with a frequency of 2.4 GHz and a distance of 25 km, our path loss comes to:

$$L_p = 32.4 + 20\log(2400MHz) + 20\log(25km) = 128dB$$

If we assume our omnidirectional antennas each have a gain of 5 dB, we can determine what signal strength we will have at the receiver:

$$P_r = 5 - 128 + 5 + 5 - 0.5 = -113.5dB < -80dB$$

We see that this result is a weaker signal than what is required for an acceptable BER. We require at least a -80 dB signal, yet with omnidirectional antennas we receive a -113.5 dB signal. Thus we cannot choose an omnidirectional antenna for this application. We therefore suggest the use of a helical type directional antenna. It provides a high signal gain, and exhibits lower path losses. Directional antennas can be constructed approximately  $2\lambda$  long and  $\lambda/3$  in diameter [66]. It is estimated that each will weigh 0.3 kg.

As discussed previously, we must maintain line-of-sight (LOS) between the helicopter and the lander. The difficulty with this requirement is that the horizon on Mars drops off quickly. At a range of 25 km, the MARV will not be visible to the base of the lander.

A good rule of thumb for sizing antennas on Earth for LOS is that due to the Earth's curvature, an object drops off at the rate of 4 inches per mile. On Mars, this rate will increase to around 7 inches per mile. With our maximum range of 25 km, this results in a 2.76 m high antenna required on the lander. We therefore recommend that all antennas be elevated to a height of 3 meters. This includes the antennas, which will send signals to the helicopter, as well as the Doppler radar system which must locate the helicopter and determine its location.

A secondary issue is that of antenna and transmitter size and weight, which must be minimized in order to meet our weight requirements. The final concern is that of available power, which should be kept within reasonable limits.

In summary, the communications design is as follows: a simple omnidirectional transmitting antenna setup will be unacceptable for telemetry transmission due to poor signal quality. Helical, directional transmitting antennas will be used, both on the helicopter and on the lander. It will be acceptable to utilize low-gain dipole antennas for receiving signals. Thus, the helicopter will be equipped with a small dipole antenna to receive commands and position information. Vertical dipole antennas are required to be at least  $\lambda/4$  high. At 2.4 GHz, this results in a height of 31 cm. With a diameter of 10 mm and a thickness of 2 mm, an aluminum dipole will weigh approximately 0.0024 kg.

Antennas on the lander will be on a 3 m high stand, which will enable LOS communications. Two directional antennas will be placed on the helicopter; one will face forward and the other aft. Together, a full 360 degrees of motion can be achieved, and thus one antenna can point towards the lander at all times. Each antenna must be mounted on a small frame attached to two actuators (one which can turn the antenna about the vertical axis, one to point the antenna towards or away from the ground). It is estimated that actuators that weigh 0.2 kg can be installed to manage this.

The electronic components of the avionics package are sensitive to temperature variations, and optimum performance requires a specified ‘operating range’ of temperatures. To ensure this, the avionics components are packaged inside insulated boxes, and a small heating system maintains the temperature required for performance. Thermal insulation must be extremely efficient as well as light weight. A precedent has been achieved in the case of the Mars Sojourner rover, which used ‘aerogel’, a solid-silica insulator [60]. We recommend using this, because it is extremely efficient, and can be molded around a thin, light, aluminum box frame.

Heaters will be placed inside the boxes which contain the avionics components. Thermal switches will monitor the internal temperature, and turn the heaters on and off based upon the required temperature. This installation is also similar to that used on the Mars Sojourner rover [60].

The ‘aerogel’ insulation weighs roughly  $20 \text{ kg}/\text{m}^3$  [67]. Thermal switches can be made to weigh 0.010 kg each [68]. The thin electronic heaters will line the inside of the avionics boxes. These heaters are 0.010 kg each, sized 76x76 mm square [68].

### 17.3 Flight computer

The onboard flight computer will be responsible for controlling the helicopter and maintaining it on its preset mission. The mission profile and point-specific commands will be preset into the flight computer. Based on the measurements of airspeed, altitude, and trim attitude, the flight computer will issue commands to adjust course and trim. Specifications for the computer were taken from the Mars Sojourner Rover computer [69]. Computing and size requirements are similar, and thus size and weight is expected to be similar.

### 17.4 Component placement/deployment

The placement of avionics components will be in three major locations, as shown in Fig. 17.6. First, certain avionics must have an outlet to the atmosphere, and a view clear of any internal obstructions. These will be placed with a face on the exterior of the fuselage. Second, certain avionics will be required on the lander. Finally, the main package of electronics should be placed in the center of the helicopter, as we wish the helicopter’s center of gravity to be located below the vertical shaft axis.

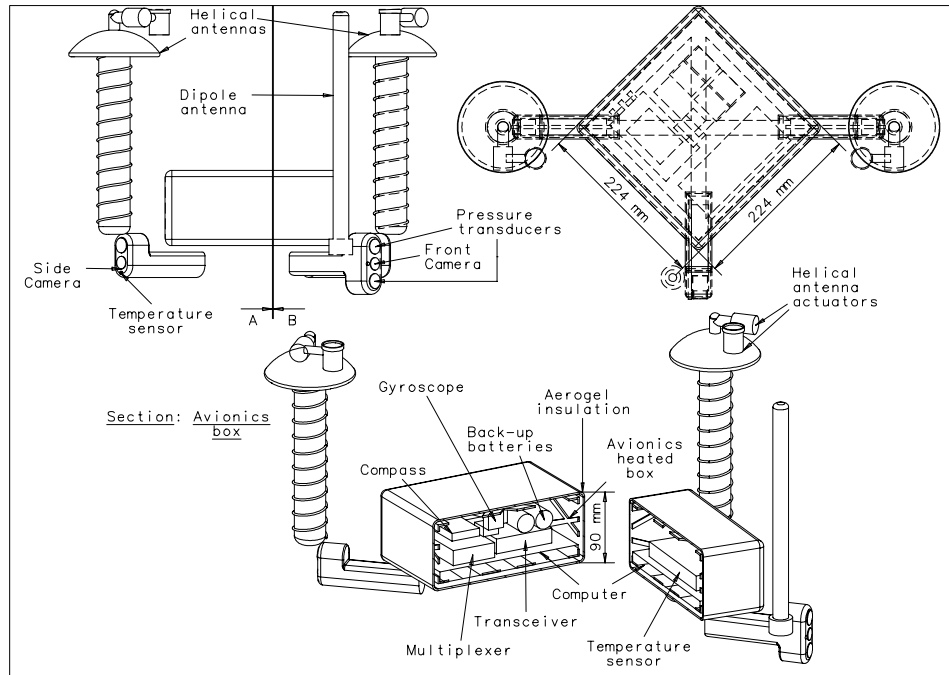


Figure 17.6: Placement of avionics

These outboard sensors will be mounted in three outboard avionics boxes. Each of these boxes will be a thin aluminum shell, wrapped in 'aerogel' insulation. Lining the inside of each box will be two thermal switches and two heating units. Each box will contain a pressure transducer, a temperature probe, and a camera. Due to the requirements of the pitot-static system, one box must be forward and one box must be on the left or right side of the fuselage (to measure total and static pressure in forward flight).

The central avionics box will contain the flight and data computer, the data multiplexer, the radio transceiver, the temperature sensor, the three gyros, and the compass. Four heaters will line the walls of this large box, along with 4 thermal switches. As with the other boxes, this will also be lined with 'aerogel' insulation.

## 17.5 Redundancy/reliability

Measures to ensure adequate redundancy will be summarized here:

Radio communication redundancy is achieved by using two antenna systems. The primary system is the pair of transmitting directional antennas. There is a secondary dipole antenna which may be utilized to send information and receive commands. Thus, the failure of a directional antenna will not result in a total mission failure.

The pitot-static system has been designed to have two ports which measure total pressure, and two which measure static pressure. The system is made of flush-mounted pressure transducers, which cannot get clogged.

The central avionics box is equipped with 4 heating units, and 4 thermal switches. The outboard avionics boxes have 2 heaters and 2 thermal switches each. Therefore, failure of one heater or one switch will not endanger the internal avionics environments.

$LiSOCl_2$  batteries are used to power 4 hours of telemetry transmission specified in the RFP.  $LiSOCl_2$  batteries were used on the Pathfinder Rover. Assuming that the heaters function for 30 minutes of the total duration of 4 hours, the total energy requirement for continuous full sensor and data relay is 72 Wh. This is calculated from Table 17.1. Currently feasible energy density values of  $LiSOCl_2$  batteries are up to 250 Wh/kg

(discussed in powerplant selection chapter). Assuming a reasonably low energy density of 210 Wh/kg, a battery weight of 0.34 kg is obtained. The battery weight is included as part of the powerplant group, not in avionics.

## 17.6 Summary

The complete avionics system, detailing weight and power drawn is shown in Table 17.1:

Subsystem	Item	No.	Weight (kg) ea.	Operating Power (W)
Command	Flight Comp.	1	0.995	5
Communication/Telemetry	Transceiver	1	0.15	5
	Multiplexer	1	0.2	0.25
	Helical Antenna	2	0.3	-
	Dipole Antenna	1	0.002	-
	Coax Cable	1	0.014	-
Vision	Camera	3	0.2	
Navigation	Compass	1	0.14	0.250
Sensors	Pressure Transducer	4	0.057	0.210
	Thermocouple Probe	3	0.012	-
	Temperature Sensor	1	0.2	0.630
	Thermal Switch	10	0.01	0.070
	Gyroscope	3	0.014	0.245
	Tachometer	1	0.09	0.100
Heating	Heating Elements	10	0.01	50
Insulation	Aerogel	-	0.01	-
Structure	Central Box	1	0.325	-
	Forward Box	1	0.087	-
	Side Box	2	0.074	-
Misc.	Wiring	-	0.01	-
TOTAL			4.077	61.76

Table 17.1: Avionics weight table

# 18 WEIGHT AND BALANCE

## 18.1 Weight breakdown

The preliminary studies to estimate the weight breakdown have been carried out using the well-known Boeing-Vertol formulae. These formulae utilize size, gross weight, and other general specifications, and fit this data to historical trends. Output from these formulae contain more specific weight information on subsystems of the helicopter. Although these formulae are accurate and valid for large Earth helicopters, it should be noted that our helicopter of 50 kg is well outside the traditional trendline used for the Boeing-Vertol formulae. Thus these formulae have been used with discretion. Actual known weights, for example for our powerplant and blades, have been substituted when available.

Fig. 18.1 shows our preliminary estimate of payload versus gross weight, using the Boeing-Vertol formulae. This curve shows no truly optimum point for gross weight, from a payload perspective. It also shows that to keep a finite payload, gross weight cannot be made to be lower than 27 kg.

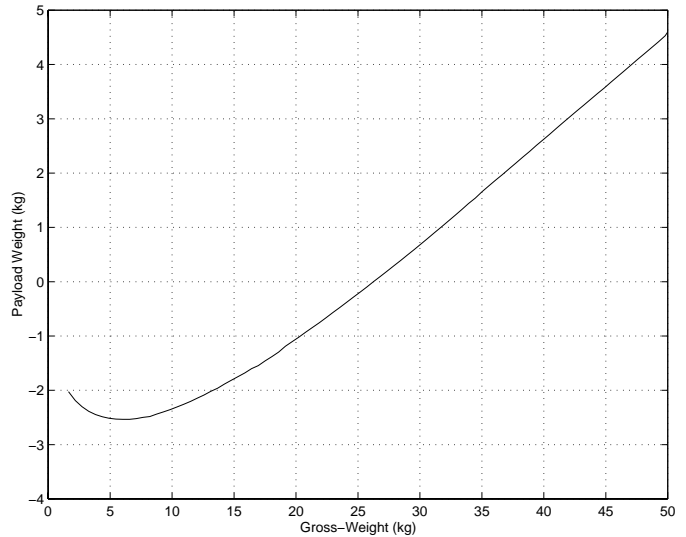


Figure 18.1: Preliminary estimate based on Boeing-Vertol formulae

Our goal, as stated earlier, has been to design the helicopter to have a maximum scientific payload capacity. It must be noted that the nature of this payload use has an effect on our gross weight. A fully loaded helicopter on the lander will remain fully loaded throughout the flight. However, a helicopter which performs a sample-return mission will be lighter during the first half of its mission, and fully loaded only during the second, ‘return’ half of its mission. We have chosen to consider the helicopter fully loaded throughout its mission, which is the conservative approach.

Based on the choice of a full load, we have chosen a gross weight of 50 kg as nominal for our helicopter. The results from the Boeing-Vertol formulae show that at this weight, we achieve 4.5 kg of payload capacity.

As we progressed through our studies, our weight estimations became more and more refined. Specific weight information replaced the preliminary estimations, changing our overall payload capacity. Each component’s size and material became known, and thus each weight was now known as well. Size and material was optimized wherever possible, to result in a minimal weight for each component. As we utilized these more accurate weight estimates, the payload capacity increased. Table 18.1 shows the final weights of the actual components chosen for our helicopter. Fig. 18.2 shows a comparison of the Boeing-Vertol formulae and the actual optimized weights. We can see that the payload capability has been increased from 4.5 kg to 10.8 kg.

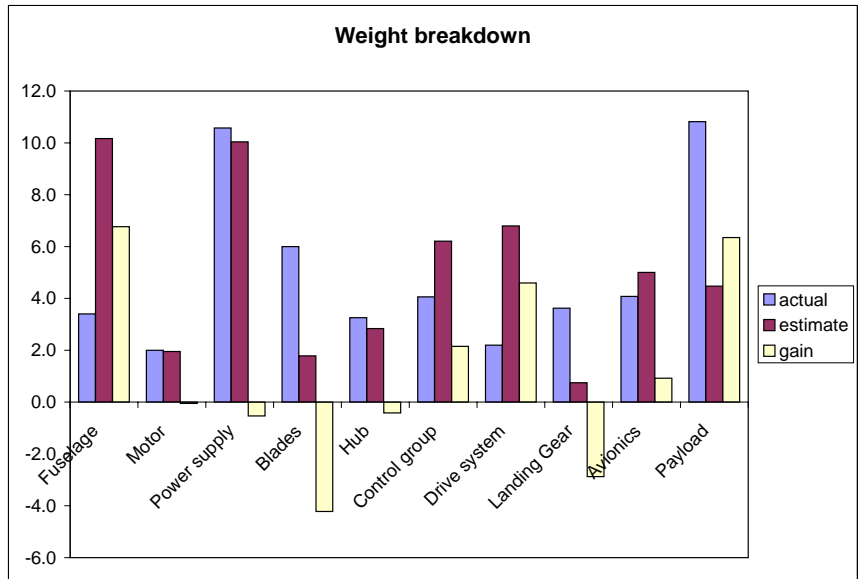


Figure 18.2: Comparison between actual weights and predictions

It is interesting to note how our final weight estimation deviates from the traditional Boeing-Vertol formulae. We have summarized a list of major reasons for these deviations here:

**Fuselage:** The fuselage is lighter than predicted because our helicopter is unmanned. Thus there is no space required for a pilot. Composite materials have also been used throughout, whereas traditional helicopters

generally utilize cheaper yet heavier metals.

**Blades:** Although very light materials were used in the blade construction, blade weight is still more than predicted by the Boeing-Vertol formula. This is because a very large blade area is required to produce lift in the thin Martian atmosphere. There is also a folding mechanism on our blades, which adds weight. Thus our blades comprise a larger proportion of our total weight, compared to traditional helicopters.

**Drive system:** A very simple mechanism has been designed for our drive system. Very few gears and heavy shafts are required. Also, lightweight composites have been used for the housing, limiting weight even more. Thus our drive system weight is lower than predicted.

**Landing gear:** Landing gear exhibits a weight higher than predicted by the Boeing-Vertol formula. This is due to the unique and necessary folding mechanism we have designed.

## 18.2 Balance

Fig. 18.3 shows the CG locations of each part of the helicopter. The CG reference point is located at the center of the bottom surface of the motor which is right on the shaft axis. Note that in our configuration, the center of gravity is nearly directly under the hub (0.06% rotor radius longitudinal offset and 0.3% lateral offset). This location will remain relatively constant throughout the flight, with the only variation coming from the loss of water by the fuel stacks. However, this has a negligible effect on the overall CG location. We suggest also that scientific payload be placed centered on the shaft axis so the CG remains on this axis. A detailed description of the weight and CG location of each part of the helicopter is given in Appendix 1.

Parameter	Mass (kg)	% GTOW	Longitudinal CG (mm)	Lateral CG (mm)	Vertical CG
Fuselage	3.4	6.8	0	0	145
Motor	2.0	4.0	0	0	50
Power Supply	10.6	21.1	4	26	80
Blades	6.0	12.0	0	0	709
Hub	3.3	6.5	0	0	677
Control group	4.1	8.1	-1	-1	622
Drive system	2.2	4.4	-1	0	255
Landing gear	3.6	7.2	0	0	-312
Avionics	4.1	8.2	0	0	240
Payload	10.8	21.6	-	-	-
Gross weight	50	100	1	7	250

Table 18.1: Weight and CG location breakdown

## 19 PERFORMANCE ANALYSIS

The performance analysis of the MARV was an integral part of the overall design process. The demands of hovering flight had a large impact on the forward flight regime, where the traditional concern of drag divergence Mach number and unconventional concern of extremely low retreating blade Reynolds number played an important role in the design process.

The analysis of the coaxial configuration proceeded along the same lines as that for a conventional rotor. The single-rotor, equivalent-solidity concept was used, and an extended momentum theory analysis showed the

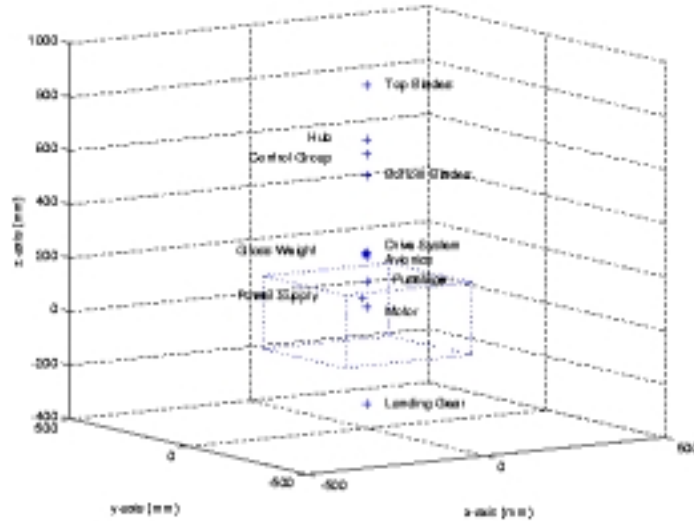


Figure 18.3: Component CG locations on the MARV

variation of required power with advance ratio. This also allowed the required fuel cell weight for the entire mission to be calculated, to check that a useful payload could still be carried. Based on these calculations, the forward flight advance ratio was chosen and for this value, a detailed trim analysis was undertaken to determine the corresponding control settings and flapping angles. This information was then used to construct the variation in angle of attack around the azimuth in forward flight, to ensure that the airfoil could operate efficiently over the entire required range.

## 19.1 Drag breakdown

The high thrust coefficient, and thus high inflow ratio, of the MARV make the induced power comprise the vast majority of the total required power. The small fuselage relative to the rotor, combined with the extremely low dynamic pressure in forward flight make the overall drag of the vehicle very small, with the profile drag of the rotor being much higher than the total drag of the fuselage.

The drag values are expressed in terms of equivalent flat plate areas, which are simply the dimensional drag values divided by the freestream dynamic pressure. These are shown in Table 19.1.

Component	Equivalent Flat Plate Area (m <sup>2</sup> )	Percentage
Rotor	62.7	99.7
Fuselage body	0.2	0.3
Total Flat Plate Area	62.9	100

Table 19.1: Drag breakdown

The profile drag of the rotor was calculated based on a standard formula for profile drag in forward flight, which is dependent on advance ratio, drag coefficient, and rotor solidity. A thrust-weighted solidity and an average drag coefficient in forward flight for the newly designed airfoil were used. The drag of the fuselage was calculated based on a strip analysis, whereby the section was split into a number of cylindrical sections. The

drag of each section was then found, using a fuselage drag coefficient of 1.17.

## 19.2 Analysis methodology

As explained in the aerodynamic design section, the basic design process involved assuming airfoil behavior in order to develop an optimum planform, and concurrently designing an airfoil which could meet these requirements. Aided by an understanding of the probable airfoil operating envelope limits, this was necessary since no existing airfoil could be used.

The forward flight analysis began with an extension of momentum theory to forward flight [72]. The hover value of inflow from the blade element results was fed to a code which then calculated the inflow as advance ratio increased by using a Newton-Raphson iteration on the forward flight inflow equation. Using these values of inflow, a calculated value of thrust-weighted solidity, and estimates of other relevant coefficients, figures for the induced, profile, and parasite power of the vehicle were then computed at each advance ratio. To gauge the effect of exceeding the airfoil drag divergence Mach number at higher advance ratios, and the increase in profile power that would be associated with this, an approximation derived by Johnson has been used. This showed that at higher advance ratios, this increase in profile power starts to offset the rapid decrease in induced power. This is an interesting result because for helicopters on Earth, this increase would not be expected until much after the minimum power point. However, since the critical Mach number here is so low, this drag penalty shows up much earlier, since usually the critical Mach number at normal lift coefficients in forward flight is relatively high. An additional implication of this effect for a vehicle operating in a very low Reynolds number environment, however, is that any intrusion into sonic flow may result in more than just a drag increase - it is more likely that the weak boundary layer will completely separate and all lifting capability will be lost. Limiting the advance ratio to a point corresponding to the airfoil critical Mach number serves as a necessarily conservative approach to minimizing the possibility of separating the boundary layer. Therefore it was decided to fly at an advance ratio lower than that corresponding to minimum power, but which still gave a useful drop in required power.

It was next necessary to determine the margin that may be needed for gusts and maneuvers. Since the effect of maneuvers is very difficult to quantify, and since it was known that because of the low Lock number the control response would be relatively slow, the gust condition was considered to be more important. Assuming the maximum gusts as stated in the RFP were on the order of 5 m/s, this translated into an extra effective advance ratio margin of 0.03 and an increase in lift coefficient of 0.2.

After determining an advance ratio, a trim analysis was conducted which calculated the control settings and flap angles in forward flight. This trim analysis used flexible flapping blade dynamics in steady level flight coupled with vehicle trim equations. It used non-linear trim equations, up to second order nonlinear structural and aerodynamic forces, and uniform inflow. Based on these results, the variation in angle of attack around the rotor az-

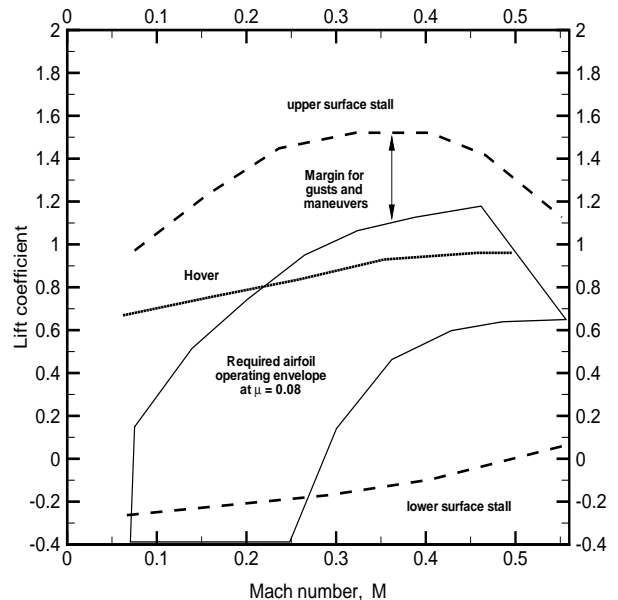


Figure 19.1: Rotor operating envelope in forward flight

imuth in forward flight was constructed, and it was ensured that the airfoil could perform over the required range of lift coefficient, Reynolds number, and Mach number. This was done by inputting the corresponding parameters at each of 14 radial stations along the blade into the Xfoil airfoil design program, and ensuring that the flow did not separate or become sonic. This is shown in Fig. 19.1, where it can be seen that the operating envelope of the airfoil has sufficient margins around the rotor operating envelope to allow for gusts and maneuvers.

### 19.3 Performance results

As expected, the total power required decreased substantially in forward flight, with a minimum power required being reached at an advance ratio of 0.37 (Fig 19.2). Ideally this would have been the design point, but since the hover condition was such a driving parameter, such a high advance ratio would have put the airfoil significantly past its drag divergence Mach number. An even greater concern than the associated drag rise that would occur is the fact that the flow would most likely completely separate and destroy all the lift. Thus, the critical Mach number boundary shown in the figure is essentially the limit on forward flight speed. This, along with the calculated margin for gusts, set the advance ratio of 0.08, corresponding to 11.5 m/s (41.4 km/hr, or 22 knots).

The power required to hover was found to be almost 4.9 kW (6.7 hp), while the power in forward flight dropped to 4.6 kW (6.2 hp). Using these figures, as well as the rest of power required curve as shown in Figure 19.2, it was next possible to determine the total energy which would be required during the mission, given the desired mission profile. This then allowed determination of the required fuel weight, as detailed in mission layout section.

Fig. 19.3 shows the distribution of power in hover and at the forward flight advance ratio of 0.08. It can be seen that the induced power clearly dominates the power requirement, which is to be expected since the thrust coefficient and therefore inflow velocity is so high. Due to the induced power percentage being so high, the profile power is a relatively small percentage of the total, even though the average drag coefficient of the airfoil at such low Reynolds numbers is significantly higher than that of normal airfoils. Lastly, parasite power required to overcome the drag of the fuselage is a miniscule contributor to the total, since the fuselage area is so small relative to the rotor.

Fig. 19.4 shows the payload/range curve. From this it can be seen that to reach the desired range of 25 km, a payload of 10.8 kg can be carried. Also, it is seen that if the

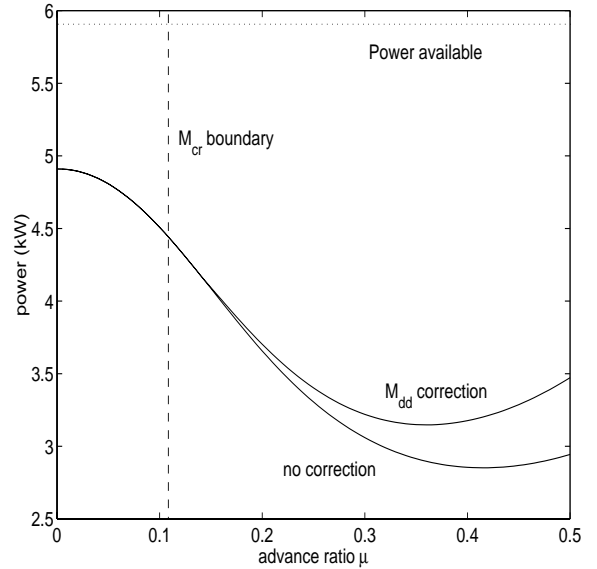


Figure 19.2: Power required in forward flight

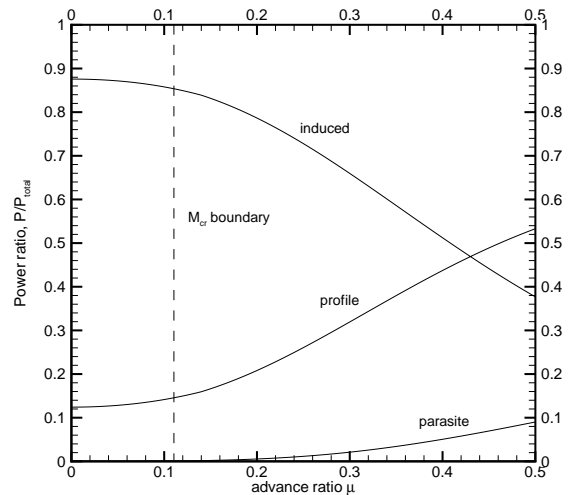


Figure 19.3: Power breakdown

payload drops to 2 kg, the range can be quadrupled. This is essentially a trade of payload for fuel cells.

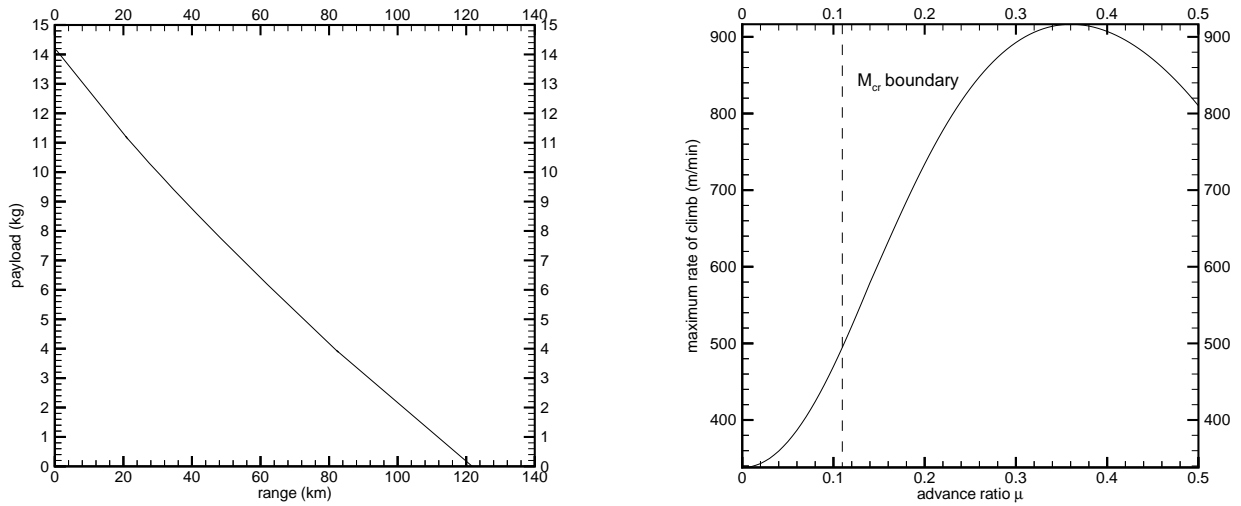


Figure 19.4: Payload vs range

Based on a maximum available power of 5.89 kW, Fig. 19.4 shows the rate of climb capability of the MARV due to excess power available. Again, the critical Mach number boundary places a realistic limit on forward flight velocity and rate of climb. It was assumed that since the RFP specifies a maximum cruise altitude of 100m, the density would not change significantly from the value at the Martian surface. It can be seen at all points between hover and the forward flight advance ratio of 0.08, the maximum possible climb velocity is well above that needed at any point during the mission profile.

## 20 PROJECT PLAN

MARV uses current technology. None of the design aspects rely on future/advanced technology 'extrapolations'. The novelty is in integration. In this section we examine the critical technologies associated with the MARV mission. We provide a technology roadmap and risk reduction testing schemes of the various design components. Finally we present a preliminary estimate of funding and personnel for a MARV development program spanning less than five years.

### 20.1 Critical technologies and risk assessment

In terms of individual components, the technologies critical to the development of MARV are: (i) low Reynolds number and high Mach number airfoils; (ii) high pressure, pure reactant PEM fuel cell system; (iii) low temperature water balance and humidification scheme for fuel cell system; (iv) thermal management system for fuel cells; (v) long duration cryogenic LH<sub>2</sub>/LOX storage system; (vi) vehicle to lander communication system; (vii) low temperature behavior of structural components; and (viii) behavior of lubricants for limited duration (30 mins) low temperature applications ( $-132^{\circ}C$ ).

The issues important at a system level are: (i) response of the rotor system in a low Lock number environment;

(ii) performance of the fuel cell system during start up and response to changes in power demand; (iii) gust response of the rotor system to provide sufficient clearance between two rotors; (iv) low temperature management of the byproduct water; (v) detailed design of control strategies for fuel and oxidant management; and (vi) investigation into implications of possible leakage in the fuel cell stacks.

Because of the nature of the mission, any error in design or system planning and implementation, allow scope for corrective action. Redundancy can be built into the navigation/guidance and control systems algorithms. However, the basic hardware components must work. Any misjudgement in rotor system, transmission, control mechanism, power plant or fuselage strength would result in a catastrophic and immediate termination of the mission. Such risks may be avoided only through extensive simulation and experimental studies.

As a preliminary design MARV is a low risk vehicle. Redundancy is designed into avionics and communication systems in MARV. The structure has been designed for failure under buckling loads during a reentry acceleration of  $100m/s^2$ . Aerodynamic performance is assured since the whole design is based on a 20% knockdown on the density.

## 20.2 Critical technology areas

No new technology is demanded for the development of MARV. It only demands risk reduction testing of the current technology components for this new application.

### 20.2.1 Technology roadmap

Here we identify the critical research areas that will further enhance MARV capabilities.

A better understanding of **low Reynolds number compressible aerodynamics** will reduce design safety margins. Tip losses for low aspect ratio blades operating at such conditions must be studied. Structural design can be optimized with better capability of **loads and vibration** prediction in presence of strong gusts and maneuvers. Development of **high strength, low stiffness materials** will provide more freedom in hub design for placing rotor blade frequencies properly. Study of **flap behavior at low Reynolds numbers** is recommended, as this may allow a plain flap or servo-flap to be used for rotor control instead of a heavy and complex conventional swashplate control mechanism. However their behavior and effectiveness in a very low Reynolds number environment is not understood. **Regenerative fuel cell technology** may provide multiple mission capability with all the advantages of fuel cell propulsion. Product water is electrolyzed back to hydrogen and oxygen with solar power. The challenge is to develop low cost high performance compressors to compress the gasses into liquids. Long duration **cryogenic storage** capabilities of LH<sub>2</sub>/LOX must be enhanced. **Guidance, Navigation and Control (GNC)** capability without support from the lander is not possible with today's technology. A light weight, low power, intensive and reliable flight control and mission computer must be built for complete vehicle autonomy. Line-of-Sight **communications** antennas as used in this design are heavy and voluminous. Lander to vehicle communications may be improved for lighter and more reliable telemetry.

### 20.2.2 Risk reduction testing

Mission risk reduction testing must be performed through extensive premission testing.

**Blade aerodynamics** and **dynamics** testing would rely on accurate simulations of the Martian environment. A better understanding of the composition and characteristics of the Martian atmosphere will provide better models. Low temperature testing for **materials** must be performed to ascertain, with confidence, the exact nature of their behavior at temperatures as low as  $-132^{\circ}C$ . The **fuel cells** need extensive testing for performance

validation while operating with high pressure pure reactants. Without validation, advanced capability cannot be utilized with confidence. Also, extensive testing needs to be performed to design exact water balance, heating and control schemes for the fuel cell system. The heat released by the fuel cell system can be properly designed to replace the heating system. **Cryogenic storage** schemes and automatic pressure control must be tested. Hence no advanced capability has been used in the present design. The **landing gear** must be tested to withstand adequate crash tests. All **avionics** need to be tested. The **data multiplexer** would need to be designed specifically, depending on the number of signals from sensors. The **antennas** and their tracking systems would have to be validated, for all angles and distances expected in the mission profile. **Aerogel** performance must be validated.

## 20.3 Preliminary resource estimate

Generally, rotorcraft cost analysis is based on historical data and empirical models [73] [74]. However, these models are not completely suitable for the analysis of MARV because of the special flight environment and very high R&D costs associated with Martian flight. In this section, the MARV cost analysis, including the cost of R&D, manufacturing and of the Mars Mission are described. All costs are in 1999 dollars.

### 20.3.1 Cost of R&D

The funding and personnel estimates for MARV development are based on our technology roadmap as shown in Fig. 20.1. In order to improve the reliability and reduce the mission risk, all subsystems should be tested before final assembly. Also, before packaging onto the Mars Lander, a final environment test for MARV should be carried out.

From this table, manpower for design can be calculated as 29.5 man-year. If the average annual cost per person is assumed to be \$200,000, the total personnel cost will be \$5.9M.

The cost of tests depends on the availability of test facilities. In this section, we assume that an existing altitude chamber can be used to conduct the rotor hover test and environmental tests. Existing low density wind tunnels may need modification. A flight simulator and test stand for the transmission have to be built. We assume that the price of an altitude chamber and wind tunnel test is \$10,000/hr, the price for a simulator test is \$600/hr, the price for a transmission stand test is \$500/hr, and the price for static and dynamic testing of the fuselage and landing legs is \$500/hr. The total cost of these tests is \$6.68M, based on the testing hours listed in technology roadmap.

To this must be added as much as \$2M for modifying existing wind tunnel for the rotor tests, and designing and manufacturing of the flight simulator and other test stands.

In summary, the cost of R&D is \$14.58M.

### 20.3.2 Cost of manufacturing

The cost of manufacturing is estimated via the model from the 1999 RFP of the AHS Design Competition [75]. It should be mentioned that this cost model is based on historical cost data and uses weight, total production quantity and production rate as primary cost drivers. To suit the requirements of our case, some parameters have been modified. For example, a factor of 3 is used to estimate the cost of manufacturing MARV's complex blades. Also, much expense is added in the avionics system. The cost of the electro-motor is actually obtained from the manufacturer [3]. Here, the total production quantity is one. The detail prices are listed in Table 20.1.

Subsystem	Cost (\$M)
Rotor System	0.093
Fuselage	0.043
Landing Leg	0.009
Transmission	0.04
Electro Motor	0.013
Control System	0.006
Flight Computer	0.02
Avionics	0.047
Final Assembly	0.065
Total Cost	0.336

Table 20.1: Manufacturing cost breakdown

### 20.3.3 Mars mission cost

According to the cost equation stated in the RFP, the Mars mission cost is approximated using a fixed launch vehicle cost of \$70M and a mission development/flight cost of \$180,000 per kg of launch mass. The gross weight of MARV is 50kg including 10.8kg payload. Therefore the total launch mass is  $50 \cdot (1+21.5+13+20) = 2775$  kg.

Thus the total mission cost becomes  $\$70,000,000 + 2775 \cdot \$180,000 = \$570M$ .

Notably, if the payload is reduced by 1kg, the mission cost will be reduced by \$10M.

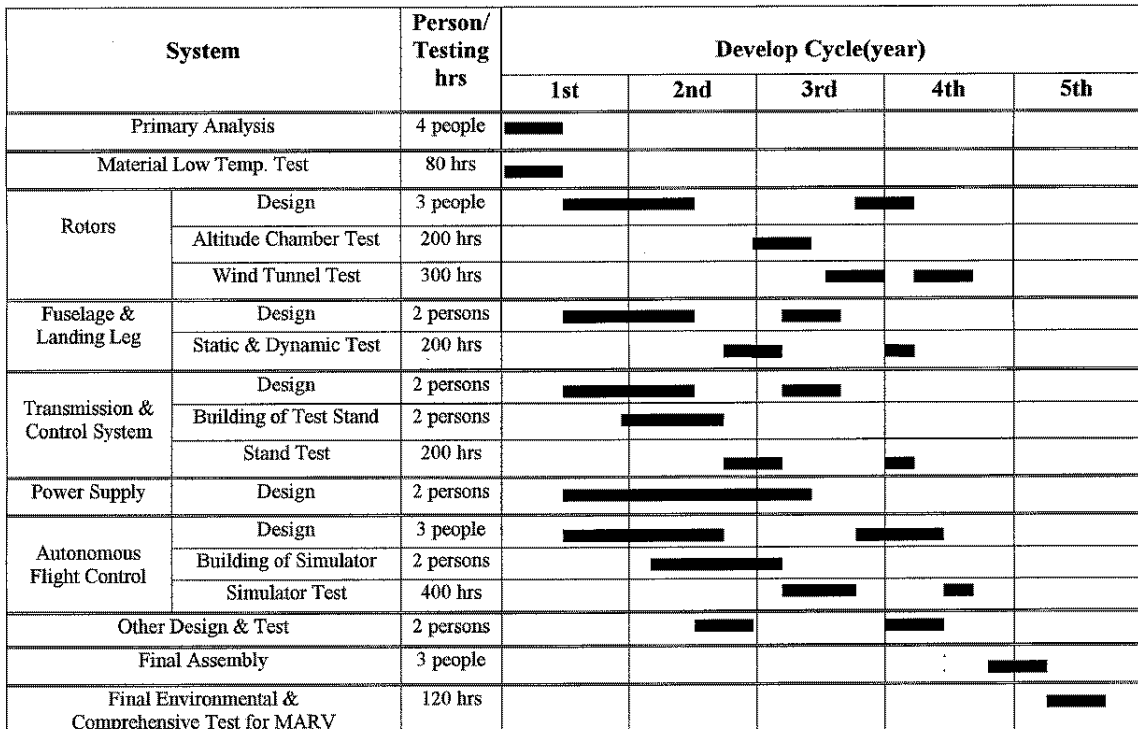


Figure 20.1: Preliminary resource estimate

## 20.4 Redundancy and reliability

Reliability has been a key issue from the very first stages of the MARV design. Hence all aspects of the design – the rotors, transmission, powerplant, control system, fuselage, and landing gears – have been designed at a level of detail that ensures maximum system reliability. Operational reliability is ensured by entirely basing the design on the RFP stipulated 20% knockdown factor on density and pressure. Mission reliability is ensured by providing redundancy in mission avionics. Communications antenna design has been performed to ensure necessary line of sight communications between lander and the vehicle. The fuel system is designed to provide 10% more energy than required by the extended mission. Extensive vibration reduction schemes are implemented: flexbeam type teetering hub design; detailed design of vibration isolator separating the gear box vibration from fuselage; and design of coaxial rotor phasing to optimize 2/rev vibration level. Thus maximum reliability in imaging (and scientific probe placement, if necessary) is guaranteed.

## 21 SUMMARY AND CONCLUSIONS

The detailed design of MARV has been presented. MARV is a 50 kg gross take off mass, coaxial helicopter specially designed for a Mars application. MARV offers 10.8 kg of payload capability over a range and endurance of 25 km and 39 minutes. The range and endurance is further extended by 0.12 km and 3 minutes by a restart. The entire 10.8 kg are reserved for scientific payload and does not include any part of the operational vehicle. A separate payload bay area is provided which can be tailored to package any scientific payload less than or equal to 10.8 kg that may be desired by the scientific community.

MARV relies on currently proven technology. A coaxial system is a reliable and proven technology on Earth. The power plant is a fuel cell. Validated test results for operations with impure fuels have been used for its design. With pure fuels a much higher performance level is guaranteed. The control system relies on the conventional swashplate mechanism of coaxial rotors. The novelty lies in tailoring the design to fit a two-bladed teetering rotor system. The structural design of the blades, landing gear and fuselage relies on state of the art composites.

Extensive engineering trade off studies were performed to develop the configuration as well as the specific design aspects of MARV. An exhaustive survey of all possible vehicle configurations was performed. Four different kinds of possible transmission systems were analyzed. Six kinds of control systems were studied. Detailed airfoil and power plant options were explored before the final design was done. Investigations were performed on fuselage structure, landing gear and the rotor hub types to select and design the most suitable configuration.

MARV is a feasible design. It is a safe, reliable and ideal candidate for being a natural extension of the use of robotic vehicles for Mars exploration.

# BIBLIOGRAPHY

- [1] Akkerman, J.W. "Hydrazine Monopropellant Reciprocating Engine Development," NASA Conference Publication 2081, 13th Aerospace Mechanisms Conference, Proceedings of a Symposium held at Johnson Space Center, April 26-27, 1979, Houston, TX.
- [2] <http://www.saft.alcatel.com>
- [3] <http://www.aveox.com>
- [4] Stevenson, S. "Mars Pathfinder Rover-Lewis Research Center Technology Experiments Program," NASA-TM-107449, Prepared for the 32nd Intersociety Energy Conversion Engineering Conference, July 27-August 1, 1997, Honolulu, HI.
- [5] Smith, J.O., Black, K.M., Kamangar, F.A., and Fitzer, J. "The University of Texas at Arlington autonomous aerial vehicle - an overview," *Journal of Applied Intelligence*, vol. 2, 1992.
- [6] <http://209.207.236.112/irp/program/collect/vtuav.htm>
- [7] Stepniewski, W.Z. and Tarczynski, T, "Open Aircrew VTOL Concepts", NASA Contractor Report 177603.
- [8] <http://www.planetinternet.be/pixel/>
- [9] <http://www.dragonflypictures.com/>
- [10] Woodley, B., Jones, H., Frew, E., LeMaster, E., Rock, S. "A Contestant in the 1997 International Aerial Robotics Competition." AUVSI '97 Proceedings, July 1997. Aerospace Robotics Laboratory, Stanford University, at <http://sun-valley.stanford.edu/users/heli/>
- [11] <http://www.naval-technology.com/projects/seamos/seamos1.html>
- [12] <http://www.army-technology.com/projects/cypher/cypher1.html>
- [13] Kroo, I., Prinz, F. Progress Report, Mesicopter Project: Research and Development Work in the Area of Ultra-Low Reynolds Number Aerodynamics, 1999. <http://aero.stanford.edu/mesicopter/>
- [14] <http://www.keyence.co.jp/international/hobby/saucer.html>
- [15] <http://www.afot.com/>
- [16] <http://larcpubs.larc.nasa.gov/randt/1993/RandT/SectionD/D7.html>
- [17] Stancil, Charles M. "Electric Toroid Rotor Technology Development", at <http://www.niac.usra.edu/files/studes/abstract/56Stancil.html>
- [18] Young, L., Chen, R., Aiken, E., Briggs, G. "Design Opportunities and Challenges in the Development of Vertical Lift Planetary Aerial Vehicles," , Presented at the 2000 AHS Vertical Lift Aircraft Design Specialist's Meeting, San Francisco, CA, Jan 19-21, 2000.
- [19] Drela, M., "Transonic Low-Reynolds Number Airfoils", *Journal of Aircraft*, Vol 29 (6), 1992.
- [20] Coleman, C.P. "A Survey of Theoretical and Experimental Coaxial Rotor Aerodynamic Research," NASA Technical Paper 3675, March 1997.

- [21] Bourtsev, B., Selemenov, V., Vagis, V. "Coaxial Helicopter Rotor Design & Aeromechanics," in *Proceedings of the 25th European Rotorcraft Forum*, 1999, Rome, Italy.
- [22] Greer, D., Hamory, P., Krake, K., Drela, M. "Design and Predictions for a High-Altitude (Low-Reynolds-Number) Aerodynamic Flight Experiment," NASA TM-1999-206579, 1999.
- [23] Evangelista, R., McGhee, R., Walker, B. "Correlation of Theory to Wind-Tunnel Data at Reynolds Numbers Below 500,000." *Lecture Notes in Engineering: Low Reynolds Number Aerodynamics*. Vol 54, Springer-Verlag, New York, 1989.
- [24] Mueller, T.J., "Low Reynolds Number Vehicles," AGARDograph No. 288, Neuilly sur Seine, France, 1985.
- [25] Daedalus Project: Materials and Manufacturing, at <http://web.mit.edu/course/16/16.00/www2/daed-materials.html>
- [26] Human powered aircraft links, at <http://www.handcyclequest.com/hpvlinks/air.html>
- [27] Human powered helicopter, at [http://helios.etsmtl.ca/index\\_ang.htm](http://helios.etsmtl.ca/index_ang.htm)
- [28] Yeo, H.S. "A Comprehensive Vibration Analysis of a Coupled Rotor/Fuselage System", PhD thesis, Department of Aerospace Engineering, University of Maryland, College Park, 1999.
- [29] Lee, T., and Chopra, I. "Design and Spin Testing of an Active Trailing-Edge Flap Actuated with Piezo-Stacks", in 40th AIAA/ASME/AHS/ASCE Structures, Structural Dynamics and Materials Conference, St. Louis, Missouri, April 16-18 1999.
- [30] Milgram, J. "A Comprehensive Aeroelastic Analysis of Helicopter Main Rotors with Tailing-edge flaps". Phd Thesis, Department of Aerospace Engineering, University of Maryland, College Park, 1997.
- [31] Hill, P., and Peterson, C. *Mechanics and Thermodynamics of Propulsion*, Second Edition, Addison-Wesley Publishing Company, June 1992.
- [32] Yuasa, S., Isoda, H. "A Concept of CO<sub>2</sub> Breathing Propulsion Engine for Planet Use"
- [33] Vincent, C., Scrosati, B. *An Introduction to Electrochemical Power Sources*, Second Edition, John Wiley & Sons, Inc, 1997.
- [34] Partain, L. *Solar Cells and Their Applications*, John Wiley & Sons, Inc, 1995.
- [35] Fahrenbruch, A., Bube, R. *Fundamentals of Solar Cells*, Academic Press Inc., 1983.
- [36] Kerslake, T., Kohout, L. , "Solar Electric Power System Analysis for Mars Surface Missions," NASA/TM-1999-209288.
- [37] Volpe, R., Balaram, Ohm, T., Ivlev, R. "A Next Generation Mars Rover Prototype," JPL-California Institute of Technology.
- [38] Lichter, M., Viteran, L. "Performance and Feasibility Analysis of a Wind Turbine Power System for Use on Mars", NASA/TM-1999-209390, September 1999, Glenn Research Center.
- [39] Mason, L. "Surface Nuclear Power for Human Mars Missions", NASA/TM-1999-208894, Lewis Research Center, January 1999.

- [40] Dornheim, M. "Special Fuel Cells Key to Month-Long Flight", in *Aviation Week and Space Technology*, Feb.28, 2000.
- [41] J.H. Hirschenhofer, D.B. Stauffer, R.R.Engleman, and M.G. Klett, *Fuel Cell Handbook*, second edition, Nov.1998, DOE/FETC-99/1076.
- [42] Voecks, G., Rohatgi, N., Jan, D., Ferraro, N., Moore, S., Warshay, M., Prokopius, P., Edwards, S. "Operation of the 25 kW NASA Lewis Research Center Solar Regenerative Fuel Cell Testbed Facility".
- [43] Stevenson, S. "Mars Pathfinder Rover-Lewis Research Center Technology Experiments Program," NASA-TM-107449, Prepared for the 32nd Intersociety Energy Conversion Engineering Conference, July 27-August 1, 1997, Honolulu, HI.
- [44] Sercel, J., Blandino, J., Wood, K. "The Ballistic Mars Hopper: An Alternative Mars Mobility Concept," AIAA/SAE/ASME/ASEE 23rd Joint Propulsion Conference, June 29-July 2, 1987, San Diego, CA.
- [45] Wichert, R. "Response to information request", March 24, 2000.
- [46] F. Barbir, "Technical Challenges in PEM fuel cell Development", Energy Partners, Inc. <http://www.energypartners.org/papers/ARGENT2.htm>
- [47] Youngblood, J., Talay, T., Pegg R. "Design of Long-Endurance Unmanned Airplanes Incorporating Solar and Fuel Cell Propulsion", AIAA/SAE/ASME, 20th Joint Propulsion Conference, June 11-13, 1984, Cincinnati, OH.
- [48] F. Barbir, Michel Fuchs, Attila Husar, J. Neutzler, "Design and Operational Characteristics of Automotive PEM Fuel Cell Stacks", Energy Partners, Inc. Paper no. 00P-63.
- [49] Federal Aviation Regulations, Part 27, U.S. Department of Transportation, 1993.
- [50] [http://nssdc.gsfc.nasa.gov/photo\\_gallery/caption/vikinglander2-2.txt](http://nssdc.gsfc.nasa.gov/photo_gallery/caption/vikinglander2-2.txt)
- [51] <http://www.sorbothane.com/>
- [52] <http://www.hq.nasa.gov/office/pao/History/SP-4205/cover.html>
- [53] O'Brien, B., Cleary, E. "Assessment of Aluminum-Lithium Alloys for Spacecraft Applications," *Key Engineering Materials*, vol. 72-74, 1992.
- [54] <http://mpfwww.jpl.nasa.gov/msp98/lander/bus.htm>
- [55] Miller, D. "Glass Fibers", in *Engineering Materials Handbook*, Vol. 1. ASM International, 1987.
- [56] Roussy, L., Parcelier, M. "Influence of Polymeric Matrix and Fiber on Composite Materials at Low Temperatures." in *Proceedings of the AIAA Sixth International Aerospace Planes and Hypersonics Technologies Conference*, AIAA-95-6134, April 3-7, 1995, Chattanooga, TN.
- [57] Colucci, F. "Helibus on the Information Highway-Information Technology makes the S-92 a Truly Global Helicopter" , *Vertiflite*, Fall/Winter 1999.
- [58] Hyer, M.W. *Stress Analysis of Fiber-Reinforced Composite Materials* The McGraw-Hill Companies, Inc., pp. 579-580, 1997.
- [59] <http://www.omega.com>

- [60] Matijevic, J. "'Sojourner' The Mars Pathfinder Microrover Flight Experiment", Jet Propulsion Laboratory, Pasadena, CA.
- [61] <http://isr/com/rwi>
- [62] <http://mars.sdsc.edu/roverpwr/power.html>
- [63] <http://www.grainger.co>
- [64] <http://www.aydin.com/telemetry>
- [65] McLarnon, B. "VHF/UHF/Microwave Radio Propagation: A Primer for Digital Experimenters," at <http://hydra.carleton.ca/articles/ve3jf-dcc97.html>
- [66] Blevins, B.A. "Small Satellite Antennas," at <http://www.psl.nmsu.edu/antennas/SmallAnt.html>
- [67] <http://mars.sdsc.edu/rover/thermal.html>
- [68] <http://www.minco.com>
- [69] <http://mars.sdsc.edu/roverctrlnav/roverctrlnav.html>
- [70] Volpe, R. "Rocky 7: A Next Generation Mars Rover Prototype," Jet Propulsion Laboratory, Pasadena, CA.
- [71] Shirley, D. "Mars Pathfinder Microrover," Jet Propulsion Laboratory, Pasadena, CA.
- [72] Leishman, J.G. *Principles of Helicopter Aerodynamics*. Cambridge University Press, 2000.
- [73] P. Leslie *Short Haul Civil Tiltrotor and Bell Model 412 Cost Drivers* In Rotorcraft Economics Workshop, Moffett Field, CA, NASA Ames Research Center, 1996.
- [74] Tishchenko, M.N., Nagaraj, V.T., and Chopra, I. "Unmanned Transport Helicopter," 55th Annual Forum Proceedings. American Helicopter Society, Montreal, Canada, May 1999.
- [75] Bell and AHS *1999 Request for Proposals for High-Speed VSTOL Personal Transport*, 16th Annual Student Design Competition.